The Pennsylvania State University

The Graduate School

College of Engineering

PROPAGATION OF ELECTROMAGNETIC WAVES THROUGH COMPOSITE MEDIA

A Dissertation in

Electrical Engineering

by

Khalid Z. Rajab

Submitted in Partial Fulfillment
of the Requirements
for the Degree of

Doctor of Philosophy

May 2008

The thesis of Khalid Z. Rajab was reviewed and approved* by the following:

Michael T. Lanagan
Associate Professor of Engineering Science and Mechanics
Associate Director of the Materials Research Institute
Dissertation Co-Adviser
Co-Chair of Committee

Raj Mittra
Professor of Electrical Engineering
Dissertation Co-Adviser
Co-Chair of Committee

Wenwu Cao
Professor of Mathematics

Randy Haupt
Department Head of Computational Electromagnetics
Senior Scientist at the Applied Research Laboratory

Elena Semouchkina
Associate Professor of Engineering Science and Mechanics

Douglas H. Werner
Professor of Electrical Engineering

W. Kenneth Jenkins
Professor of Electrical Engineering
Head of the Department of Electrical Engineering

*Signatures are on file in the Graduate School

Abstract

The propagation of electromagnetic waves through ceramics and composite materials is investigated in this work. The design of complex artificial materials has potential as a valuable tool for application to many new devices, such as high-resolution lenses and electromagnetic imaging devices, as well as for the improvement of currently existing ones. A technique is demonstrated for the characterization of ceramics and other dielectrics, at terahertz frequencies, with the use of terahertz time-domain spectroscopy (THz TDS). Composite materials comprised of complex scatterers, and in particular spherical resonators, are studied using the same system. In order to calculate the scattered fields from a large number of resonant spheres, a new technique is developed, based on the characteristic basis function method (CBFM). This technique improves the computational speed of the calculation, as well as allowing the solution of bigger scattering problems, with a larger number of larger sized spheres. Finally, a technique is developed that allows the characterization of an anisotropic material, at any angle of incidence, to provide all the material tensor coefficients of the material of interest. The material tensors of effective media are related to the structure of the medium's lattice, and the importance of symmetry in the structure is demonstrated. A procedure is demonstrated that allows one to verify that the retrieved parameters are indeed those of the bulk material, by comparing eigenvectors of the extracted T-matrices. The procedure reveals that for many complex materials, such as dielectric resonators arrays, effective medium approximations do not apply, and so calculation techniques such as the CBFM, or the finite-difference time-domain method must be used to correctly determine the behavior of a composite.

Contents

List of Figures

List of Tables

Acknowledgments

I would like to thank my advisers, who have been fantastic intellectual role-models.

Dr. Michael Lanagan has guided me as a researcher from my first days as an undergraduate student at Penn State. He has always motivated me to follow my interests in academia, as well as providing me with numerous opportunities for travel and learning that have made my pursuit of further education a pleasure.

Dr. Raj Mittra has always been a wonderful source of conversation, with his travels all around the world. There has been no problem that I have presented him with, no matter how seemingly complicated, that he has been unable to break down into the simplest of terms.

I would also like to express my sincere gratitude to my doctoral committee, as well as everyone at the Materials Research Laboratory. My committee – Dr. Wenwu Cao, Dr. Randy Haupt, Dr. Elena Semouchkina, and Dr. Doug Werner – have all been teachers of the highest order, and have helped to improve my dissertation immeasurably. There are so many people at MRL that have helped me over the years, that I am bound to miss some. Nevertheless I will try my best, and if I have left you out, then please accept my sincere apologies! Steve Perini has been a source of help at the microwave lab since I first started at MRL, but more importantly he has been a good friend and someone to talk to through my years growing up at Penn State; Donna Lucas, who has somehow managed to keep her patience while dealing with my complicated travel plans; Amanda Baker, who has successfully deciphered my designs and managed to use her significant artistic and engineering merits to turn them into workable devices; Paul Moses, for his interesting discussions on the state of the university, the environment, and the world. At MRL, I would also like to thank Dr. Clive Randall, who has always demonstrated his passion for sport as well as science; Dr. Elena Semouchkina and Dr. George Semouchkin, for their fascinating discussions on science, as well as their travels and exploits around the world.

My thanks also goes to all of my family. My parents, Leila and Ziad, for instilling me with a love of knowledge, travel, food, and life; my sister, who is always ready to have a laugh (and climb Kilimanjaro!); my *new* parents, Françoise and Daniel Yvanoff, who have raised the most wonderful daughter and family, and introduced me to all the amazing food of Bretagne!; my grandparents, Tareq and Jehan, who have been intellectual role-models not just for me, but for the whole of Kuwait, in establishing cultural and educational standards for the country to strive towards; my grandmother Lim Kwee Yang, who was always ready to welcome me to Singapore with an open heart; Mamie Gouarec for making the best crèpes; Nur, Mae and Tareq; Misha'l, Mikie, Freija and Haytham; Nadr and Denise, and Yasmine, Faye, Nadia, and Tareq; Patrick, Celene and Cheryl; Rawa and Rasmia; Fatima, and all the rest of my family, and of course Ali, Manaf, Sohail, Wa'el, Obi, Abdullah, and Rouffy.

Marie – words cannot express what you mean to me. Kula Tano!

Dedicated to my parents,

Leila Fonglin-Rajab and Ziad Sayid Rajab,

and to my grandparents,

Jehan and Tareq Sayid Rajab,

and Foo Tiang Kwang and Lim Kwee Yang.

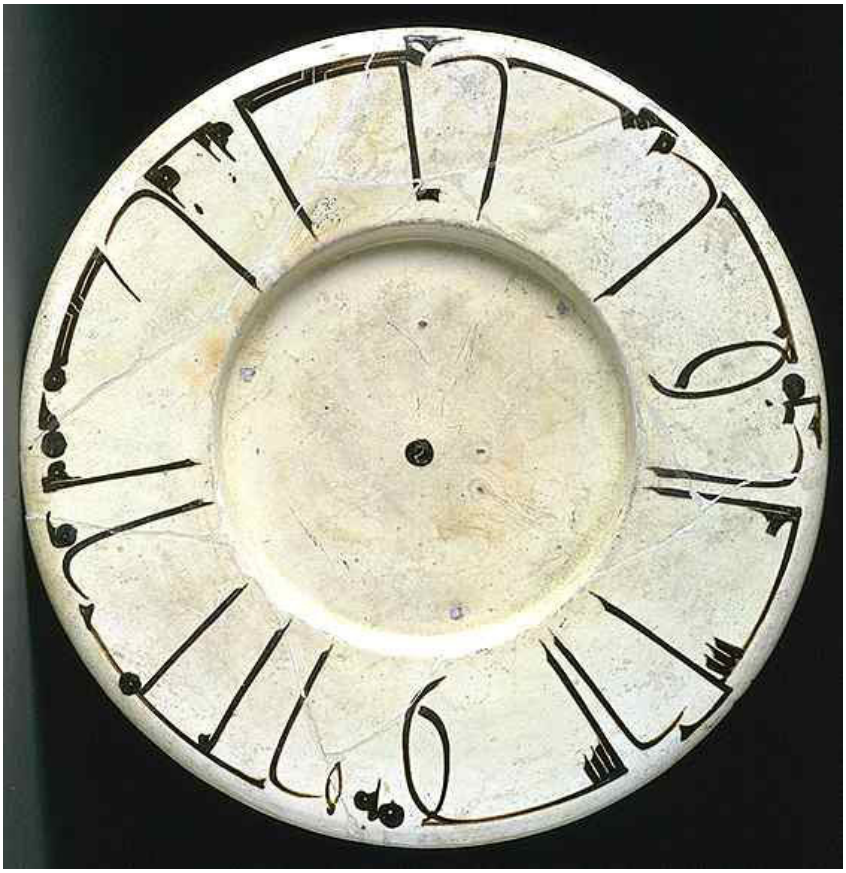

Figure 1: "Science is bitter-tasting at first, but sweeter than honey in the end. Good health to the owner of the dish". An epigraphic dish from eleventh or twelfth century Khurasan or Transoxiana, western Iran, the central motif is based on the Chinese yin and yang pattern. *Courtesy of Musée du Louvre, Paris.*

Chapter 1

Introduction

1.1 Statement of the problem

This thesis presents a methodology for characterizing materials and complex composite electromagnetic structures, and in particular aggregates of resonant spheres. The motivation behind this work is to contribute to an understanding of the behavior and response of complex media, and to determine the viability of these exotic materials for application to new engineering devices and designs. The term *metamaterial* - a composite media with a response that differs from those of its constituent parts - has received increasing attention in recent years. The promise of wonderful new applications, verging on the science fiction, has driven research from engineers, scientists and mathematicians. The idea of a perfect lens, or a cloaking device, to name but two, have captured the imagination of the general public. And academically, the number of publications and citations has grown exponentially. A great draw for research, and of interest, has been the *homogenization* of a complex structure; representing that complex structure as an *effective media* that will simplify its use in the designs of devices, as well as some of the wonders that have been promised. The question bodes though, how well do these effective media truly represent the structure they are replacing? It would surely simplify all design processes if they were a perfect representation, but are these representations truly correct?

A common technique for representing a composite structure as an effective media, is to

replace that structure with an effective permittivity and permeability. The permeability and permeability are the parameters of any material that determine how it will respond to an electromagnetic field. The idea is that, if you can find a permittivity and a permeability that responds exactly as your structure does, then you can replace your structure with a black box, of which you can ignore everything else but those two parameters, and that will allow you to work with it for any application you may need.

The basis for the techniques that are used to determine those parameters have existed for as long as the study of electromagnetics itself. We will discuss the history of this research further, later in this chapter, however we should note that the attempt at determining the permittivity and permeability of a structure is not just limited to complex, exotic materials, but is of utmost importance to the characterization of even the basic of materials. We will begin our discussion, in chapter 2, with the demonstration of a material characterization technique for some of these materials, in a region of the electromagnetic spectrum that is possibly the fastest growing in terms of interest - the terahertz band. This is a region of the spectrum that contains 90% of the energy in the universe, but which we have only very recently been able to attempt to harness. Even relatively common materials may possibly have unknown or surprising behavior at these frequencies, and so it is of interest to explore. After our investigation of ceramics at these frequencies, we will then turn our attention to more complicated structures, i.e., periodic arrays of spheres. These spheres have complicated scattering, but is it possible to represent these spheres as an effective media?

To begin to answer this question, we need a full understanding of how electromagnetic fields behave with these spheres. And for that purpose, in chapter 3 we will present a new, highly efficient technique for calculating the fields that are scattered from the spheres. The technique is called the characteristic basis function method (CBFM), and allows the complete solution of the scattering from a random, or periodic, arrangement of spheres.

We stated earlier that the idea of replacing a structure by an effective permittivity and permeability was very popular. However, can a complex structure like an aggregate of spheres

really behave like a regular isotropic dielectric material? It turns out that the permittivity and permeability are themselves very complicated ideas. A common approach has been to use a constant for each of the two, or in some cases provide a frequency dependence, i.e., *dispersion*. However in reality, materials can be, and quite regularly are, more complicated than just frequency dispersive. They may be *spatially dispersive*, or if they are functions of space, then they are *inhomogeneous* (very common despite what most textbooks would have you believe!) They may also be *nonlinear*, in that they are functions of the strengths of the fields. What we are most interested in, however, is *isotropy*, or rather, the lack thereof. An isotropic material is independent of the polarization of the interacting electromagnetic wave. These structures are extremely simple to analyze. However, many materials are in fact *anisotropic*; that is, they are dependent on the direction of the field. In chapter 4 we will discuss the relationship of symmetry in a structure to its anisotropy, and determine what complex structures cannot be modeled as isotropic media. In order to provide a methodology to do this, we have developed what is, to the best of our knowledge, the first technique, at the microwave and terahertz frequencies, that allows the complete determination of the material parameters of the most general form of an anisotropic material. Additionally, the technique will allow characterization at oblique incident angles (almost all others are limited to normal incidence), while also providing a simple quantitative test for whether the extracted parameters truly reflect those of the *bulk* material. It will be shown that a sample must be of a minimum thickness, otherwise *surface layer effects* dominate, and the material will not behave as a homogeneous bulk material.

In the concluding chapter, the results of the work are summarized, including important findings and newly developed techniques. Finally, suggestions for future work will be made.

1.2 The terahertz gap

Recent years have seen a large amount of interest devoted to the terahertz (THz) region of the electromagnetic spectrum. A lack of sources, especially in the frequency range of

100 GHz to 10 THz, had made investigations into this band difficult. This was despite the promise of applications in the characterization of materials, biomedical imaging, detection of explosives, communications, and a plethora of other fields. The term "terahertz gap" proved a particularly good description of the gap between the microwave and infrared (IR) bands; the division between solid-state electronics and optical photonics. Lately, this gap has begun to narrow as new, higher-power sources have started to cover a greater range of frequencies, leading to excitement at the range of applications that have begun to open up.

1.2.1 Terahertz sources

The earliest investigations at terahertz frequencies were reported in the 1960's, not long after the development of the laser. Gebbie et al., in particular, demonstrated an HCN laser operating at .337 mm (0.89 THz) [1]. Shortly afterwards, the same group used their setup to characterize the monochromatic refractive indexes and absorption coefficients of various benzene compounds [2], as well as air [3]. In recent years, the development of new terahertz sources have involved both solid-state electronic devices and optical schemes. Solid-state technologies, extended from the microwave frequencies, have in particular been useful for applications in wireless communication. The two main photonic sources that have been attracting attention are the quantum cascade laser (QCL), as well as traditional optical THz generation. The QCL was first demonstrated at far-IR frequencies (70 THz) in 1994 [4], while the first terahertz band (as we have defined it here) QCL, operating at 4.4 THz, was demonstrated in 2002 [5, 6]. Undoubtedly, the most widely used source for terahertz materials research and characterization has been time-domain optical THz generation. The earliest works on this technique were performed at AT&T Bell Laboratories [7] and the IBM Watson Research Center [8]. These two labs also developed, respectively, the electro-optic and photoconductive antenna for THz generation/detection. The electro-optic effect was used to generate Cherenkov radiation, while the technique used currently, namely the free-space electro-optic sampling method, was developed by Wu et al. [9]. These works were also the

precursors to the technique termed THz time-domain spectroscopy (TDS). This is the most prevalent technique used currently for material characterization at terahertz frequencies. We will discuss THz TDS, as well as the two main generation/detection techniques in more detail in chapter 2.

For further information on the various aspects of terahertz technology, the interested reader may consult one of a number of reviews. This began with the earliest terahertz research involving submillimeter astronomy [10], as well as more contemporary works including terahertz materials [11], so-called "T-ray" imaging [12, 13], biomedical applications [14], space sciences [15], and security applications [16, 17]. There have also been a number of reviews on the historical achievements of terahertz research in general [18, 19, 20, 21, 22].

1.3 Metamaterials

The term *metamaterial* was coined in 1999 by Rodger Walser [23, 24]. He defined them as:

> *Macroscopic composites having a manmade, three-dimensional, periodic cellular architecture designed to produce an optimized combination, not available in nature, of two or more responses to specific excitation.*

In 2001, Valerie Browning and Stu Wolf of the Defense Advanced Research Projects Agency (DARPA), redefined the term, stating that:

> *Metamaterials are a new class of ordered composites that exhibit exceptional properties not readily observed in nature. These properties arise from qualitatively new response functions that are:*
>
> - *Not observed in the constituent materials and*
> - *Result from the inclusion of artificially fabricated, extrinsic, low dimensional inhomogeneities.*

This definition has remained popular in the metamaterials community, with the key omission of the reference to observation in nature. Many natural materials, whether discovered or not, exhibit unusual properties that would be beneficial to engineers if we were able to artificially design them to our needs. An example of such a natural material is the opal, which at visible wavelengths exhibits some of the metamaterial properties that we will discuss, due to its ordered lattice of silica spheres.

1.3.1 Negative refractive indexes and other "metamaterial" concepts

Possibly the most well known possiblity allowed by metamaterials is the *negative index of refraction (NIR)*. The index of refraction determines how much the speed of light is reduced in a medium, compared to in a vacuum. This is determined by Snell's Law:

$$n_1 \sin\theta_1 = n_2 \sin\theta_2, \tag{1.1}$$

in which n_1 and n_2 are the refractive indices of two materials, while θ_1 and θ_2 are the angles that a ray of light will make, to the normal, at an interface between the two media. Snell's law, named after Willebrord Snellius who derived it in 1621, had been described a few years earlier, in 1602 by Thomas Harriot. However it was in fact first described in it's current form centuries earlier, by the Islamic mathematician Abu Said al-Ala ibn Sahl [25, 26]. Ibn Sahl had been investigating the use of lenses as burning instruments, and had known of the laws of refraction by at least 984 CE. Ibn Sahl was one of a number of Islamic scholars and philosophers in this Golden Age of science in the Islamic World. A century earlier, Ya'qub ibn Ishaq al-Kindi (known as Alkindus in the West), had begun the promotion of the Greek and Hellenistic philosophies, and particularly those of Aristotle. Among his many contributions to philosophy, mathematics, and science (he wrote what is possibly the oldest known work on environmentalism and pollution), he was an accomplished optical scientist; he investigated both the Aristotelean and the Euclidean theories of optics, eventually settling,

after numerous laboratory and thought experiments, on the Euclidean ray optical theory (See Figure 1.1). The works of ibn Sahl and al-Kindi were later built upon by probably the greatest Islamic scientist, Abu Ali al-Hasan ibn al-Haytham (known in the West as Alhacen) in, among other texts, his *Kitab al-Manazir (Book of Optics)* [27] - a classic referenced for centuries afterwards by many optics scholars, including Sir Isaac Newton. Ibn al-Haytham not only investigated the theories of refraction, both theoretically and experimentally, but he also applied it to the first experimental studies of the dispersion of visible light into the colors of the rainbow. In addition, he investigated the multiple reflections within a spherical lenses [28], which is a very early precursor to a later chapter in this thesis on scattering from dielectric spheres.

Returning to the concept of a negative refractive index, Viktor Veselago showed in 1964 (with the translation to English appearing in 1968), that a media with simultaneously negative permittivity ϵ and permeability μ, a so called *double negative (DNG)* material, will exhibit a negative refractive index [29]. Applying this to Snell's Law (1.1), what this means is that light traveling through free space, and incident upon a material with a negative n, will in fact bend in a direction opposite to what one would expect with a positive index media.

In addition to the concepts of negative refraction and double negatives, Veselago also related these properties to the *handedness* of a wave, i.e. whether the $\mathbf{E}$, $\mathbf{H}$ and $\mathbf{k}$ vectors form a right- or a left-handed triplet. He showed that conventional double positive materials will exhibit right-handedness, while a DNG material will be left-handed, leading to the term *left-handed material (LHM)*. What left-handedness implies, is that for a particular electric $\mathbf{E}$ and magnetic $\mathbf{H}$ field, the phase vector $\mathbf{k}$ in a left-handed medium will point in the opposite direction to that in a right-handed one. A further result of this property is the *backward-wave*, for which the phase vector points in the opposite direction to the Poynting, or power vetor $\mathbf{S}$. In fact, this wave was first postulated for mechanical systems by Horace Lamb in 1904 [30], and Henry Pocklington in 1905 [31]. Arthur Schuster first discussed backward-

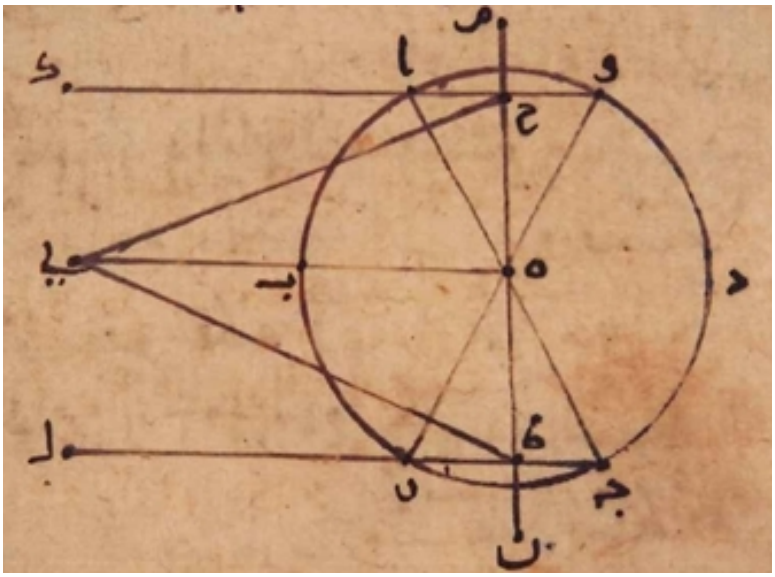

(a)

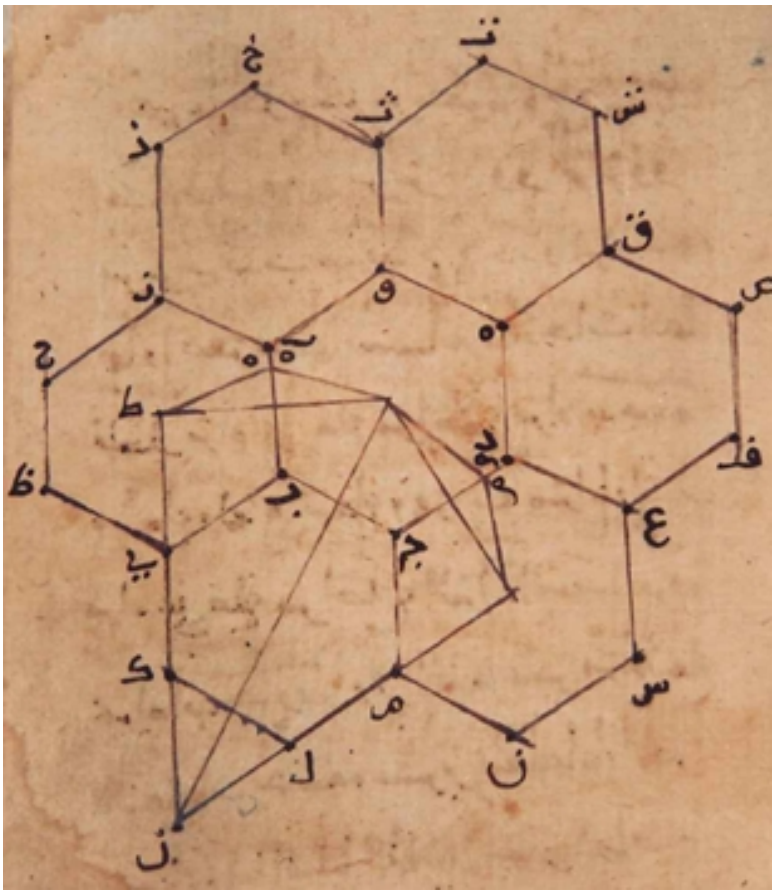

(b)

Figure 1.1: Geometrical investigations of ray optics by al-Kindi. *Courtesy of the Tareq Rajab Museum, Kuwait.*

waves for optical systems [32], with speculations on the implications for refraction. In fact in Lamb's paper, he mentions that the concept of oppositely directed group and phase velocities was proposed to him by Schuster, who noted anomalous dispersion in the absorption spectra of sodium vapor. Interestingly though, Schuster was doubtful of the applications of negative refraction, due to these highly absorbing bands. Nevertheless, in the 1950's, the backward-wave did find useful application in the form of the backward-wave oscillator [33].

Veselago did, however, note that no known naturally occurring materials simultaneously exhibited the properties he wrote of. It was not until around four decades later that further progress was made. Pendry *et al.* first proposed an artificial medium, formed by periodic arrays of wires mimicking a plasmon, that would exhibit a negative effective permittivity at microwave frequencies [34]. Three years later, in 1999, he then demonstrated a cylindrical structure formed with two split rings, now known as the *split-ring resonator (SRR)*, as well as a similar structure which he name the "Swiss roll" capacitor, that both exhibited effective magnetic permeabilities from nonmagnetic materials. Pendry showed that the designed effective permeabilities could include negative values, and thus the two components needed to create an artificial double negative medium were available. In 2000 Pendry described the creation of a material with a negative index of refraction [35], and in the same year, the first double negative structure was fabricated by Smith *et al.* [36]. A transmission line approach to left-handed materials was later developed [37, 38, 39, 40, 41], with close relation to the backward-wave oscillators of the 1950's.

The definition of a metamaterial is not, however, limited to just these double negative, left-handed media. There are a number of other exotic properties and intriguing structures that are borne out of the engineering of artificial media, including *photonic bandgap (PBG)* and *electronic bandgap (EBG)* structures [42, 43, 44, 45, 46]. In fact, the first metamaterial devices, using the current definition, were probably Kock's metal lens antenna [47] and metallic delay lens [48]. He designed them in the 1940's to take advantage of physical effects caused by many periodic, sub-wavelength conductors; in effect creating an artificial material.

A few years later, in 1952, Corkum followed these up with his own investigations of artificial dielectrics composed of spheres [49].

1.3.2 Homogenizing a material

Homogenization is the process of replacing a complex structure with an effective medium - a material that has properties which would exactly replicate the response of the structure that it has replaced. The history of homogenization is almost as long as that of electromagnetics itself. The first significant results in electromagnetic homogenization were due to the investigations of collections of molecules or inclusions in a background environment. The works of Octavio Mossotti in 1850 [50], and Rudolf Clausius in 1870 [51] led to the Clausius-Mossotti formulas. Lord Rayleigh later studied the effective material parameters of a cubic lattice of spherical or cylindrical inclusions [52], later generalizing his theory to ellipsoidal inclusions [53]. James Clerk Maxwell-Garnett derived the Maxwell-Garnett formula, based on his work on the color of glasses due to metal inclusions [54]. Dirk Anton George Bruggeman then developed his theory, the Bruggeman formula, in another important step for mixing theory [55]. Joseph Keller followed Lord Rayleigh's lead by looking at the effective material properties of arrays of spheres and cylinders [56], and then provided a breakthrough in homogenization theory, revolutionizing the field by using variational calculus to obtain an effective conductivity for an array of cylinders [57]. A more in-depth overview of homogenization and mixing theory can be found in [24, 58, 59].

Pendry took a classic technique to homogenization in [60], when he used a volume integral [59] to average the fields over the unit cell enclosing his structure. More popular lately, due to their experimentally simple and numerically efficient implementation, have been variations of the Nicolson-Ross-Weir [61, 62] transmission line-based material characterization method. Using this technique, the reflection and transmission coefficients are measured with a wave incident upon a slab of an unknown material, followed by an inversion to provide the material parameters [63]. Chapter 4 will cover this topic in more detail, including the demonstration

of a method for extracting the anisotropic permittivity and permeability tensors of a slab of unknown material.

1.3.3 Applications of metamaterials

Since the development of Kock's artificial dielectric antennas, a number of applications have been both theorized, and demonstrated for metamaterials. Amongst the most well known has been Pendry's so-called *perfect lens* [35], with which a negative refractive material can beat the *diffraction limit*, and focus sub-wavelength light. Additionally, he conjectured the surprising result that a single-negative material is capable of amplifying evanescent waves, and thus focusing the near-fields. He proposed that silver, which demonstrates negative permittivity, plasmonic behavior at optical frequencies, if only a few nanometers thick, can behave as a sub-wavelength focusing lens. This was verified experimentally by the group of Xiang Zhang [64], when a silver lens used in conjunction with atomic force microscopy, was capable of achieving superior resolution to what is normally possible.

At microwave frequencies, the transmission line approach to metamaterials has resulted in a number of beneficial applications, including novel directional couplers [65], leaky-wave antennas with backfire-to-endfire scanning capabilities [66], and miniaturized antennas [67, 68]. At terahertz frequencies, liquid crystals have allowed the design of *zero-index* and tunable metamaterials [69], with which the refractive index may be tuned from negative, to zero, and to positive values. Applied in the terahertz gap, this may see significant benefit as a filtering device.

Chapter 2

Terahertz Materials Characterization

2.1 Dielectric characterization

The dielectric properties of materials are vitally important in the design and application of any particular device at any frequency range. The dielectric behavior of a material is defined by its complex permittivity, $\epsilon = \epsilon' - j\epsilon''$. However, we generally deal separately with the relative permittivity, $\epsilon_r = \epsilon'/\epsilon_0$ (referred to as the dielectric constant κ in the materials community), and the loss tangent, $\tan\delta = \epsilon''/\epsilon'$ (or alternatively quality factor, $Q = 1/\tan\delta$) . A variety of characterization techniques exist that would allow one to obtain these dielectric properties, but the availability of so many different techniques can also lead to some confusion; each one of the plethora of material characterization methods has its own advantages and disadvantages, and they are each suitable for use in a particular frequency range, from close to DC up to the infrared frequencies. Above these frequencies, the macroscopic material models begin to fail.

Figure 2.1 shows the electromagnetic spectrum from DC up to the ultraviolet frequencies, with the THz gap in between. At frequencies below the THz gap, we have the electronic regime. Here we can find the radio waves, including the microwaves (300 MHz to 300 GHz). Above 300 GHz, and up to the edge of the visible light spectrum (450 THz to 750 THz), the infrared waves (300 GHz to 450 THz) can be found. The THz gap is in fact a part of the near-IR band, and above the gap we have the optical regime. Just as the sources and

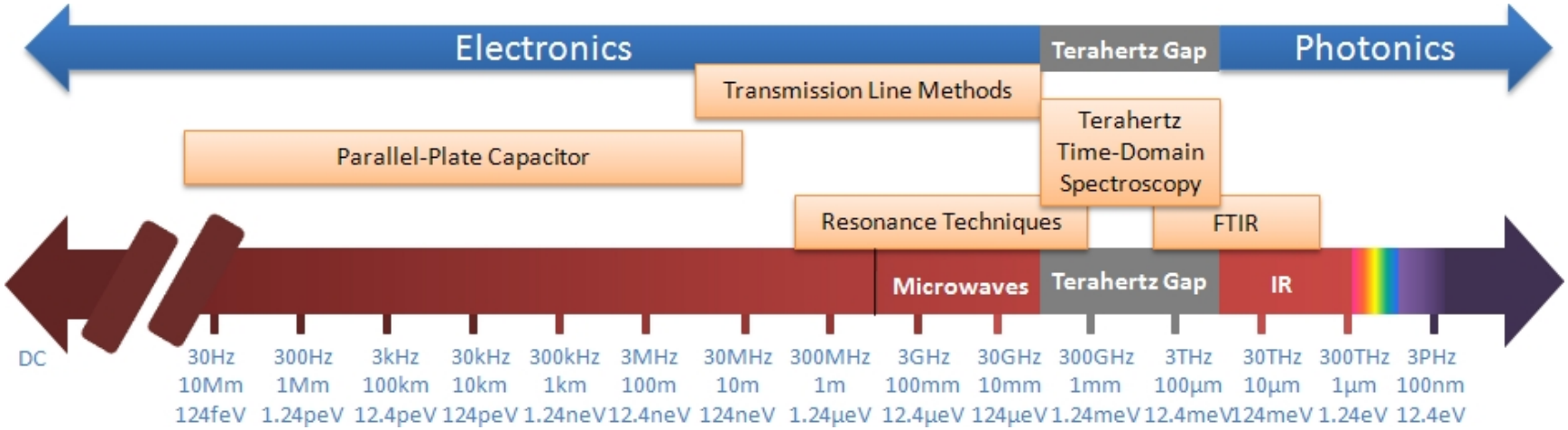

Figure 2.1: Electromagnetic spectrum, from DC up to visible and ultraviolet wavelengths, where macroscopic models of materials begin to fail. The spectrum is split up into the electronic and photonic regimes, with the THz gap in between. Various classes of material characterization techniques are shown, covering different frequency ranges.

devices change between these two regimes, the material characterization techniques, along with the response of the materials themselves change.

2.2 Outside the terahertz Gap – material characterization techniques

Before we discuss dielectric characterization techniques at terahertz frequencies, an overview of the available methods outside the terahertz gap will be provided. This will give the reader the context in which to place the terahertz techniques, as well as an idea of the frequency ranges that we may cover. As well as splitting the electromagnetic spectrum into electronic and photonic regimes, Figure 2.1 also summarizes a number of the available techniques. It is impossible to be truly exhaustive; however, the most widely used methods are included.

Low frequency techniques, up to around the 10 MHz range, rely on the measurement of quasistatic parameters (i.e., capacitance or impedance). At microwave frequencies, a variety of techniques exist, each of which can loosely be defined as either a resonant or a broadband measurement. The resonant techniques have the ability to measure high quality factor (high Q), low loss materials, with small sample sizes, albeit only in a narrow frequency band (or bands). In general though, low loss dielectrics have very little change in the permittivity over a broad frequency range, so resonant techniques are ideally suited for these materials. They are however limited in measuring high-loss (low Q) materials. The broadband techniques, on the other hand, are well suited to measuring high-loss samples, at a large range of frequencies, although they require larger sample dimensions. At the upper end of the frequency scale, reflectivity measurements are used to obtain the broadband dielectric characteristics of a material. The Electromagnetics Division of the National Institute of Standards and Technology have published a series of comprehensive reviews covering a large number of different characterization techniques [70, 71, 72]. Afsar et al. have also covered a number of techniques in [73]. The interested reader is referred to these reviews; however,

we will briefly introduce a number of the most important characterization techniques.

2.2.1 Parallel plate ($\sim$ DC - 30 MHz)

Below 30 MHz, LCR meter or impedance analyzer measurements are used to obtain the permittivity [73]. This involves the measurement of the parallel-plate capacitance of an electroded dielectric. The permittivity is then obtained from the capacitance measurement and the material dimensions. We should also note that capacitor geometries are not limited to parallel plates; interdigital capacitors have been shown to be suitable in certain circumstances, e.g., biosensors for remote complex permittivity determination [74]. This method is more mathematically complicated however, as complex mapping techniques are needed to reduce the geometry into a solveable problem. This also limits accuracy.

Table 2.1: Summary of material characterization techniques.

Measurement Technique	Approximate Freq. Range	Advantages	Disadvantages	Key References
Parallel plate	DC - 30 MHz	Accurate measurements Sub-wavelength samples Simple technique	Uniform field required	[73]
Open cavity (resonant)	0.5 - 50 GHz	Accurate for low losses High Q Small samples Easily available equipment setup	Not for high losses	[75, 76, 77]
Fabry Perot resonator (resonant)	20 - 300 GHz	Suitable for thin, low loss samples High Q High frequency measurements	Limited high-loss accuracy due to metal mirrors	[78, 79]
Split-cylinder cavity (resonant)	10 - 20 GHz	Accurate for low losses High Q Flexibility with sample area	Inaccurate for high losses Samples must be smooth Difficult to manufacture cavity	[80, 81]
Cavity perturbation (resonant)	1-25 GHz	Accurate Arbitrary sample (with known dimensions)	Approximation errors Not for low losses (rectangular) Difficult to manufacture cavity (cylindrical)	[82]
Ring resonator (resonant)	0.5 - 40 GHz	Accurate for permittivity Simple calculations Physically intuitive	Difficult to measure loss Loss dominated by conductor	[83, 84]

continued on next page

continued from previous page

Measurement Technique	Approximate Freq. Range	Advantages	Disadvantages	Key References
Coaxial probe (Transmission line)	10 MHz - 25 GHz	Very large frequency range Suitable for liquids and semi-solids	Air gaps cause significant errors Air bubbles (liquids) cause significant errors Thick Sample Limited accuracy	[85, 86]
Coaxial transmission line	0.5 - 25 GHz	Broad frequency range Suitable for high loss samples	Difficult to manufacture Inaccurate for low losses	[61, 62, 87]
Rectangular waveguide (transmission line)	1 - 25 GHz	Relatively broadband Suitable for high loss samples	Low loss inaccuracy Cut-off defines lower frequency Large samples for low frequencies	[61, 62, 87]
Planar transmission line	1 - 25 GHz	Simple technique	Loss dominated by metal Fabrication difficulty	[88]
Free space (transmission line)	1 - 100 GHz	High frequency measurements Non-contacting Measurement flexibility	Large sample for low frequencies Dielectric lenses required Complicated calibration Flat, smooth samples required	[89]
Terahertz time-domain spectroscopy	0.1 - 10 THz	Non-contacting Phase coherence Suitable for high-/low-temperature measurements	Expensive setup Atmospheric absorption bands Smaller spectral range than FT-IR	[11, 90, 91] [92]
Fourier transform infrared	1 - 100 THz	Non-contacting Very broadband	Phase incoherent Complicated permittivity fitting procedure Atmospheric absorption bands Limited spectral resolution	[93]

2.2.2 Resonant cavity ($\sim$ 0.5 - 50 GHz)

Resonant cavities have the advantage of being high Q structures. The cavities are usually an easily-analyzed geometry, such as a rectangle or a cylinder, where the resonant modes can be determined as functions of the dimensions and ϵ_r. The general idea is to extract the permittivity, knowing the resonant frequency and the dimensions. The dimensions are measured to within an acceptable level of error (error analysis will be discussed in a later section), while the frequency sweep is usually measured with a vector network analyzer. Subsequently, from the bandwidth of the measured peak, the material's loss tangent or Q may also be extracted. From these techniques we are able to measure extremely high Qs (on the order of 10,000), albeit only at a single frequency (or a few frequencies if we use multiple modes).

Open cavity techniques are very widely used, since samples can be conveniently fabricated, and is generally small in size with respect to the wavelength. This is of particular benefit at low frequencies, for example at 1 GHz where the wavelength in free space is 30 cm. The classical geometry for this technique is the dielectric cylinder, as demonstrated by Hakki and Coleman [75, 76]. A more recent method makes use of the nonradiative dielectric waveguide (NRD), and allows the measurement range to be extended to higher frequencies [77]. As an example of the sample dimensions that would yield a 1 GHz resonance for $\epsilon_r = 10$, the Hakki-Coleman cylinder that would give a TM_{011} resonance here could have a diameter of 10 cm, and a thickness of 8.6 cm. The NRD waveguide LSE_{101} resonance could occur here with dimensions of 7 cm $\times$ 5 cm $\times$ 10 cm. The Fabry-Perot open resonator is a technique suitable for characterization up to 300 GHz [78, 79] . In this case, a coupling aperture in a mirror is used to excite a thin dielectric that is rested on a second planar mirror. The setup has very high quality factors, enabling the measurement of low losses, however metal losses from the mirrors lead to inaccuracy.

Another resonance technique is the split-cylinder cavity method [80, 81]. The fixture here consists of a fixed lower cylindrical cavity, and un upper cavity that is lowered to sandwich

the material in-between. The sample is a thin dielectric slab that is larger than the cross-sectional area of the cavity. One may then use the TE_{011} resonant mode of the system to obtain the complex permittivity of the enclosed dielectric.

Other examples of resonant techniques at microwave frequencies include perturbational cavity methods [82], and ring resonator techniques [83, 84].

2.2.3 Transmission line methods ($\sim$ 0.01 - 300 GHz)

Broadband characterization methods at microwave frequencies generally consist of various transmission line techniques. The transmission lines may be microstrips, coaxial and rectangular waveguides [61, 62, 87, 94], or even free space. A wave propagating along any transmission line will have a phase velocity determined by the structure, so the analysis of the phase of the reflection (S_{11} and S_{22}) or transmission (S_{21} and S_{12}) coefficients will yield the relative permittivity. This, in conjunction with the magnitudes of those coefficients, could allow one to extract tanδ as well. And because the techniques do not rely on any particular resonances, they are broadband, allowing characterization over a large frequency range. However, they are by their nature, inaccurate when measuring materials with low tanδ.

Coaxial transmission lines are formed by an outer conductor enclosing a dielectric, with an inner conductor running through the center. They can be used both as an open-ended probe [85, 86], with S_{11} measurements of a dielectric covering the end of the line, or as a two-port transmission line. As a characterization method, they provide results over a broad frequency range, going down to MHz frequencies for the case of the open-ended probe. This technique does, however, have limited ϵ_r accuracy, and as with all transmission line techniques, it is inaccurate when measuring low losses. On the other hand, the two port coaxial transmission line provides more accurate ϵ_r results. The difficulty with using this technique stems from its awkward geometry. A sample must fit snuggly within the conductors. As a result, this method is most suitable for liquids, powders, and semi-solids (such as bio-materials). Similar

techniques take advantage of other structures, such as the rectangular waveguide, in place of the coaxial line. The rectangular waveguide is, however, limited by a lower cut-off frequency of a supported mode. Nevertheless, the geometry is more conducive to measurements of most solid dielectrics.

A microstrip consists of a thin conducting strip on top of one side of a dielectric substrate. The reverse side of the substrate is generally a conducting ground plane. The characterization methods rely on the measurements of the phase of a wave transmitted through the structure, and this phase can be used to extract an effective permittivity, based on the speed of propagation of the wave through the structure. Analytical formulas can then be used to obtain ϵ_r. Similar planar technologies such as coplanar waveguides may be used in place of the microstrip [88].

The free-space measurement technique [89] is a transmission line method in the loosest sense of the term. The transmission line is in fact just the free space in between two antennas (most often horns). A sample is placed in-between the horns, and the measured S-parameters are used to determine the material characteristics. Although it appears straight-forward at first glance, there are in fact experimental difficulties that make it less than trivial to operate. The primary difficulty is with the nature of the experimental setup; theoretically, the material is assumed to have infinite area, while the propagating wave is assumed to be a perfect plane wave. Both of these assumptions are obviously incorrect, but we can try to get as close to the ideal case as possible. A dielectric lens may be used to focus the beam to the center of the sample. Additionally, a sample area of at least a wavelength squared is generally required, which may be prohibitively large at low frequencies. A further difficulty is the calibration of the setup, as there are no connectors. The TRL (Thru-Reflect-Line) calibration method applies well to this technique though, with a large conducting plate acting as the Reflect standard. Additionally, if the network analyzer in use allows it, time-domain gating may be used to remove artifacts of the system and improve the calibration. The use of absorbers can also improve measurements. Despite these difficulties, the technique is very useful at

mm-wave frequencies, up to around 100 GHz. Much above these frequencies, the size of the horn antennas become prohibitively small and traditional microwave frequency sources do not work. This technique is of particular interest to us because it is most similar to, and relies on the same principles, as that of the terahertz time-domain spectroscopy (THz TDS) characterization methods that will be described in this chapter.

2.2.4 Fourier-transform infrared spectroscopy ($\sim$ 1 - 100 THz)

At infrared frequencies, Fourier-transform infrared spectroscopy (FT-IR) can be used to obtain the complex permittivity, or more commonly at these wavelengths, the complex refractive index $\tilde{n} = n - j\kappa$ (where the imaginary part of the refractive index, κ is not to be confused with the materials community's dielectric constant) [93]. The absorption coefficient, α, of a material can also be defined as

$$\alpha = \frac{2\omega\kappa}{c}. \tag{2.1}$$

A variety of similar techniques exist, but a common one makes use of reflectivity measurements. The magnitude of the light reflected off a sample can be measured over a broad frequency range, however FTIR is insensitive to phase. The Kramers-Kronig causality relations can be used to obtain a good approximation for the phase [95]. With the measurements of the polar phonon modes, as well as the high frequency permittivity ϵ_∞, a model dielectric function can be fit to obtain the complex permittivity over the frequency range of interest. This dispersion analysis is not straightforward though, and numerical approximations must be made to approximate the phase function. Additionally, reflection measurements are sensitive to surface roughness, and hence, the sample surfaces must be smooth. It should also be noted that Fourier-transform spectroscopy can also be applied at millimeter-wave frequencies, for example with a two-beam polarization interferometer, to obtain broadband characterization in the 30 - 300 GHz range [79].

2.3 Terahertz time-domain spectroscopy ($\sim$ 0.1 - 10 THz)

With the increasing interest in the development of applications within the terahertz gap, material characterization techniques are necessary for frequencies between 100 GHz and 10 THz. These frequencies are not well covered by either the microwave techniques, or by FT-IR. Terahertz time-domain spectroscopy is one method that can be used to fill this gap. This spectroscopic technique operates with an ultrashort pulse of terahertz radiation, transmitted through a material. The pulse is probed, either after transmission or reflection. The measured signature can be transformed to the frequency domain. The spectrum subsequently provides amplitude and phase information of the material. This information can be used for a variety of applications, including materials characterization, tomographic imaging, and chemical detection.

Before we discuss the dielectric characterization techniques, the experimental setup will be described so as to provide the reader with an overview of the system (see Figure 2.2). The experimental setup can be split into five main operations subsequent to the source producing the laser: beam splitting; signal delay; THz generation; propagation through the sample; and, THz detection. A laser with an appropriately short pulse will generate a beam, which is split so that the majority of its intensity forms the pump beam, used for THz generation. The remaining portion of the beam is used as a probe beam for detection. Once the beam has been split, the pump beam is directed through a delay line. The length of the delay line is swept, so that the entire pulse amplitude is obtained as a function of time. This delayed pump beam is then used for THz generation. The most common method of generating THz waves is by use of a biased photoconducting gallium arsenide (GaAs) aperture antenna [96, 97]. A laser pulse generates carriers in the conduction band of the semiconductor, effectively causing it to turn from an insulator into a conductor. The bias voltage across the antenna accelerates the carriers so that a current is formed, and the rapid switching of the pulses induces the generation of THz radiation, in a manner similar to an antenna working at microwave frequencies. Other generation schemes include the use of

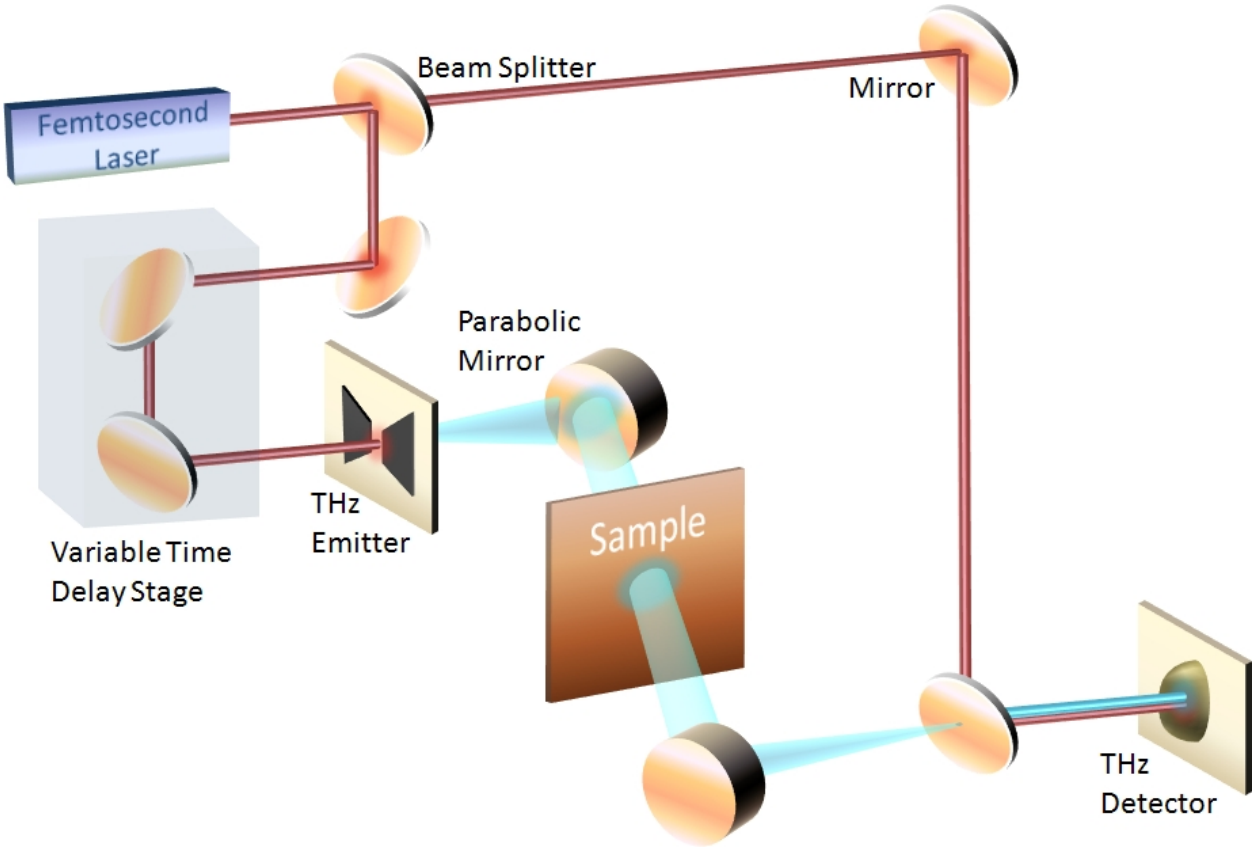

Figure 2.2: Typical setup for THz TDS. The ultrafast laser beam is split into a probe beam and a pump beam. The pump beam is delayed, and then used for THz generation. The THz waves are collimated and focused on the sample, and then again collimated and focused, along with the probe beam, onto a THz detector, so as to obtain the temporal profile of the electric field.

crystalline materials. Once the THz waves have been generated, they are free to propagate and interact with the sample. A detector is placed in an appropriate position to measure the signal of interest (for example transmission or reflection). Photoconducting antennas and electro-optic crystals may also be used for detection. The probe pulse that was split from the pump beam is delayed so that it arrives at the detector at the same time as the THz pulse. For detection with an electro-optic crystal [9, 98, 99], the polarization is rotated slightly, as the probe pulse travels through the birefringent crystal simultaneously to a point in the THz pulse. This rotation is proportional to the amplitude of the THz field, and the direction of rotation is proportional to the sign. Polarizers and photodiodes can be used to determine these polarization changes.

The setup we used is set up as follows: a diode laser pumped Ti:Sapphire laser emits 60 μs pulses at a center wavelength of 790 nm, operating at 80 MHz. The beam is split so that 90% of the intensity is used as a pump beam for THz generation, with the other 10% used as a probe beam for detection. THz generation was provided by excitation of a biased GaAs photo-conductive aperture antenna, with the THz pulses collimated and focused by a series of off-axis parabolic mirrors through the sample, and onto a 1 mm thick ZnTe crystal.

2.3.1 Transmission

Once the time domain signal has been measured, the frequency spectrum is obtained with a discrete Fourier transform (DFT). Numerically, this would be done by way of a fast Fourier transform (FFT). A reference spectrum, with no sample present, is first measured. This is best done through a nitrogen-purged atmosphere, so as to minimize water absorption and remove resonances. A second spectrum is then measured with the sample in place.

Figure 2.3 shows the transmitted time domain signals through the reference and through a sample specimen. The delay is evident in the pulse traveling through the sample, as light is slowed down due to the material's refractive index. An approximation of the average permittivity of the material over the pulse's measured bandwidth can be determined using this delay, as:

$$\epsilon_r = \left(1 + \frac{c}{d}\Delta t\right)^2, \tag{2.2}$$

where c is the speed of light in free space, d is the sample thickness, and Δt, shown in Figure 2.3, is the delay between the peak amplitudes of the reference and sample pulses.

This is, however, just a rough approximation, and does not give us much more than a crude estimate of the permittivity over the frequency range. To find the frequency-dependent complex permittivity of the sample, an FFT should be performed on the signal. We will now have the complex transmission spectrums of the reference and the sample, the magnitudes and unwrapped phases of which are shown in Figure 2.4. These transmission spectra may be used to investigate the dielectric properties of the sample. We can view the sample's system

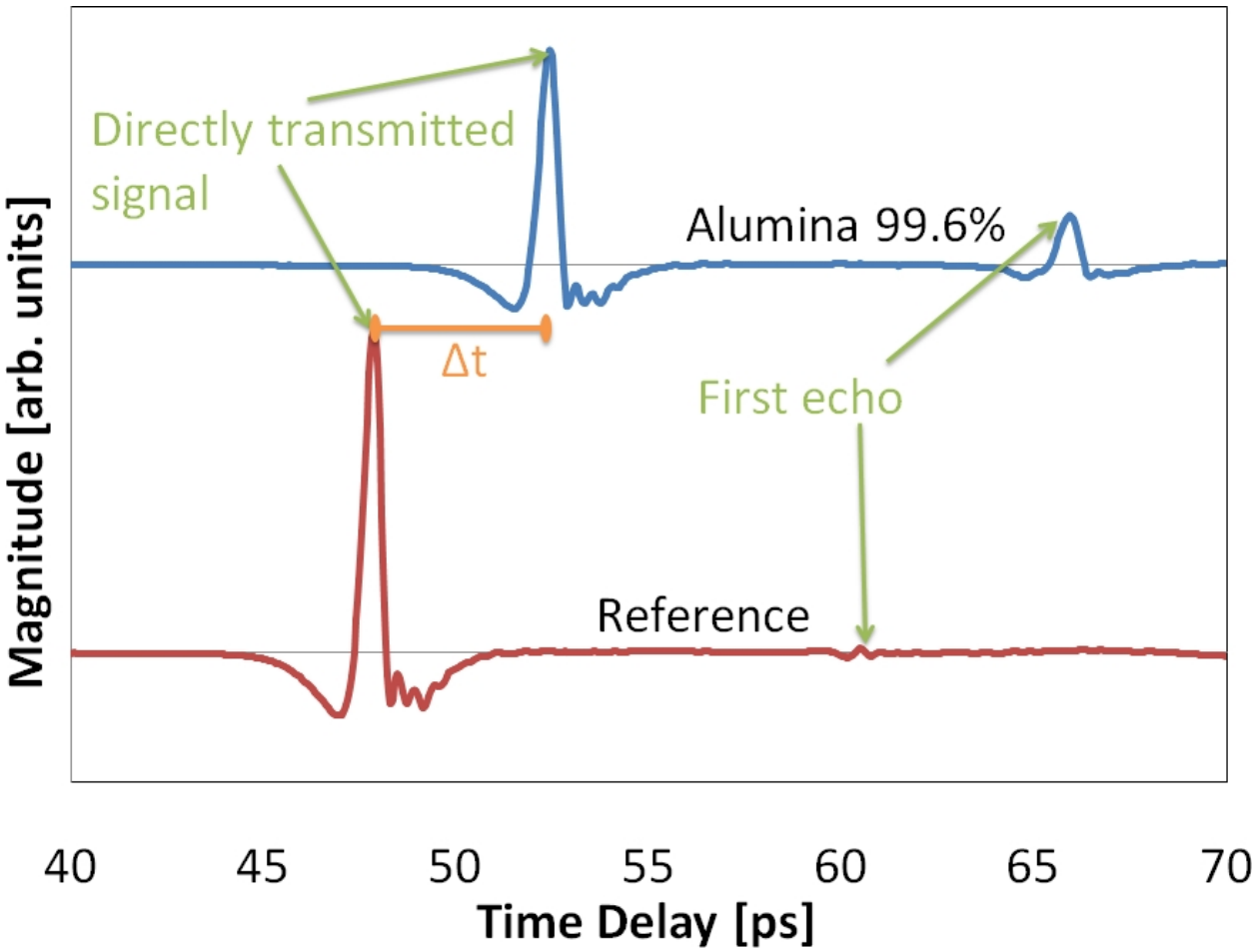

Figure 2.3: Time Domain signal.

as a three-medium (air - dielectric - air) Fabry-Perot resonator. The transmission, $t(\omega)$ is derived from the Fresnel formulas as [90]:

$$t(\omega) = \frac{T_{sample}(\omega)}{T_{ref}(\omega)} = \tau(\omega)P(\omega, d) \cdot \frac{1}{1 - r(\omega)P^2(\omega, d)} \cdot \exp\left(j\frac{\omega d}{c}\right), \tag{2.3}$$

where $T_{sample}(\omega)$ and $T_{ref}(\omega)$ are the complex transmission spectra through the sample and the reference, respectively, and $\omega = 2\pi f$ is the radial frequency. The reflection, transmission and propagation coefficients are represented by $r(\omega)$, $\tau(\omega)$, and $P(\omega, d)$ respectively, where,

$$r(\omega) = \frac{\left[\tilde{n}(\omega) - 1\right]^2}{\left[\tilde{n}(\omega) + 1\right]^2} \tag{2.4a}$$

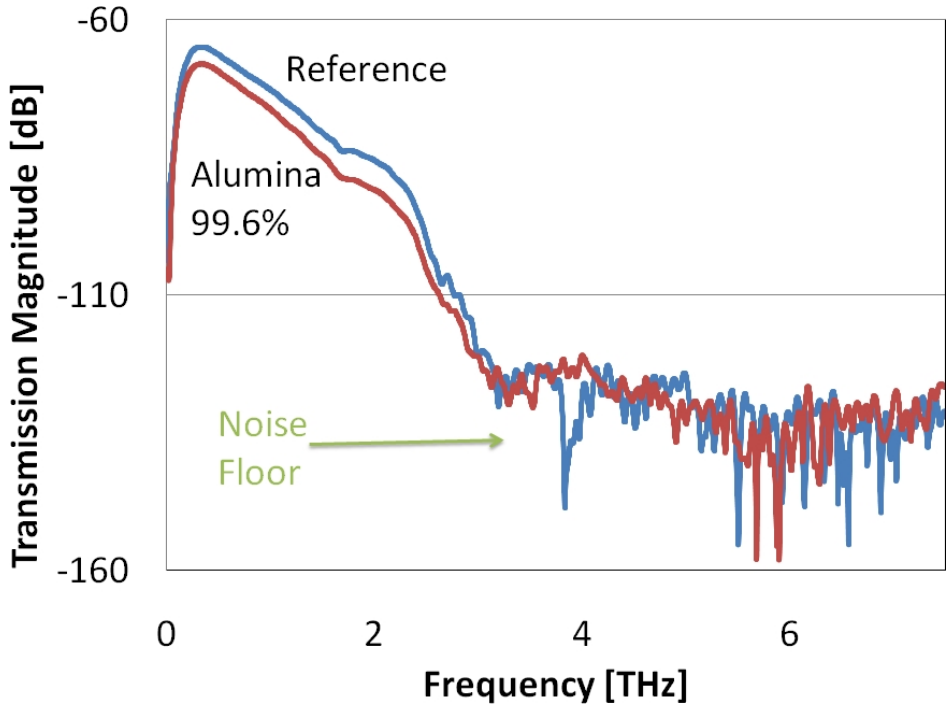

(a) Magnitude.

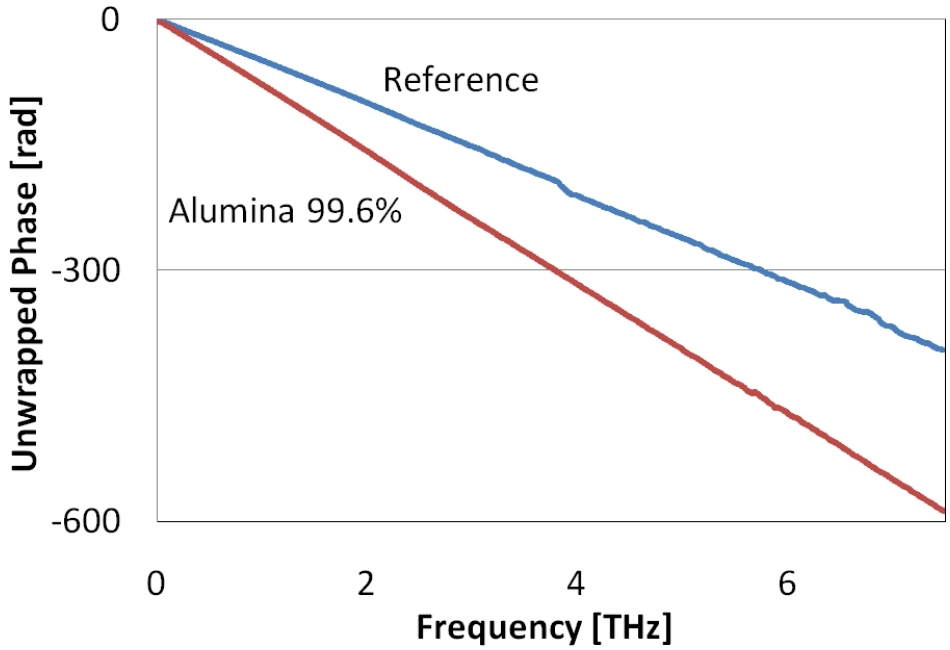

(b) Unwrapped phase.

Figure 2.4: Reference and sample transmission spectra.

$$\tau(\omega) = \frac{4\tilde{n}(\omega)}{\left[\tilde{n}(\omega)+1\right]^2} \tag{2.4b}$$

$$P(\omega, d) = \exp\left[-j\frac{\omega\tilde{n}(\omega)d}{c}\right]. \tag{2.4c}$$

For a non-magnetic material the complex permittivity $\epsilon(\omega)/\epsilon_0 = \sqrt{\tilde{n}(\omega)}$.

Although this solution is exact, in practice (2.3) is not the best method of solving for the material characteristics. Temporal echoes, as seen in Figure 2.3, are caused by reflections in the slab that lead to time-delayed transmitted pulses. The equation is derived by assuming that all temporal echoes have been measured, implying an infinite time measurement. In practice a signal of only a few tens of picoseconds is measured, which may not allow sufficient damping of the transmitted peaks before they can be neglected. Furthermore, reflections from the experimental setup will eventually interfere with measurements. Numerical techniques are also necessary to solve for $\tilde{n}$, rendering this technique impractical.

We will now look at a more efficient and accurate technique that also uses the measured transmission spectra. This technique compares the spectra of two different samples of the same material, but with different thicknesses. The trick here is to treat the reference as a material with *zero* thickness. The solution, as will be outlined below, has been derived to separately treat each of the temporal echoes. The directly transmitted signal, which is represented by the 0^{th} echo, is suitable for use when all echoes are neglected. Following the method of Duvillaret et al. [91, 100], the spectral component of the transmitted field through a sample, $E_t(\omega)$, can be expressed as:

$$E_t(\omega) = E_i(\omega)\tau(\omega)P(\omega, d)\sum_{p=0}^{\infty}\left[r(\omega)P^2(\omega, d)\right]^p, \tag{2.5}$$

where r, τ and P were defined in (2.4), and $E_i(\omega)$ is the incident field. This equation is consistent with (2.3) if we simplify the geometric series with

$$\sum_{p=0}^{N} x^p = \frac{x^{N+1}-1}{x-1} \Rightarrow \sum_{p=0}^{\infty}\left[r(\omega)P^2(\omega, d)\right]^p = \frac{1}{1-r(\omega)P^2(\omega, d)}. \tag{2.6}$$

E_t corresponds to the transmission through the sample, T_{sample}. T_{ref} is not, however, the

incident field, but the field transmitted through the reference. This is just the incident field modified by a phase term, such that $T_{ref} = E_i \cdot \exp(j\omega d/c)$, and so (2.5) is equivalent to (2.3), with the summation term representing the Fabry-Perot effect. Although the form of (2.3) appears simpler than that of (2.5), we wish to take advantage of the nature of the infinite geometric series, as each successive term will represent a temporal echo. Thus, using (2.5) we can handle a finite number of temporal echoes.

Defining the sample's transmission coefficient for an echo p,

$$t(p,\omega) = \frac{T_{sample}(p,\omega)}{T_{ref}(p,\omega)} = \tau(\omega) r^p(\omega) P^{2p+1}(\omega, d) \cdot \exp\left[j\frac{\omega d}{c}\right], \tag{2.7}$$

we can find its magnitude and phase as:

$$\begin{aligned} |t(p,\omega)| &= |\tau(\omega)| \cdot |r(\omega)|^p \cdot |P(\omega,d)|^{2p+1} \\ &= \frac{4|\tilde{n}| \cdot \left[(n-1)^2 + \kappa^2\right]^p}{\left[(n+1)^2 + \kappa^2\right]^{p+1}} \times \exp\left[-\kappa(2p+1)\frac{\omega d}{c}\right] \end{aligned} \tag{2.8a}$$

$$\begin{aligned} \varphi(p,\omega) &\equiv \arg\left[t(p,\omega)\right] \\ &= \arg[\tau(\omega)] + p \cdot \arg[r(\omega)] + (2p+1) \cdot \arg[P(\omega,d)] + \frac{\omega d}{c} \\ &= -\left[(2p+1)n - 1\right]\frac{\omega d}{c} - 2p \cdot \arctan\left(\frac{2\kappa}{|\tilde{n}|^2 - 1}\right) + \\ &\quad + \arctan\left[\frac{\kappa\left(|\tilde{n}|^2 - 1\right)}{|\tilde{n}|^2(n+2) + n}\right]. \end{aligned} \tag{2.8b}$$

Note that eq. (3) in [91] contains an error in the phase term. φ represents the difference in phase between the T_{sample} and T_{ref}. The phases of these terms should be unwrapped before the difference is taken. Assuming a relatively low loss sample, i.e. $\kappa \ll n$, we can solve for n and α using (2.8a) and (2.8b), as well as (2.1) to get:

$$n = \frac{1}{(2p+1)} \cdot \left[1 - \frac{c}{\omega d}\varphi(p,\omega)\right] \tag{2.9a}$$

$$\alpha = \frac{-2}{(2p+1)d} \cdot \ln\left[\frac{(n+1)^{2p+2}}{4n(n-1)^{2p}}\,|t(p,\omega)|\right]. \tag{2.9b}$$

The refractive index and absorption coefficient can be found from the measurement of the directly transmitted signal. Substituting $p = 0$ into the equations above, we have

$$n = \left[1 - \frac{c}{\omega d}\varphi(0,\omega)\right] \tag{2.10a}$$

$$\alpha = \frac{-2}{d} \cdot \ln\left[\frac{(n+1)^2}{4n}\,|t(0,\omega)|\right]. \tag{2.10b}$$

Figure 2.5 shows the results of these equations. Modifications to the formulas above can be used to determine the permittivity of a thin-film material [90, 92].

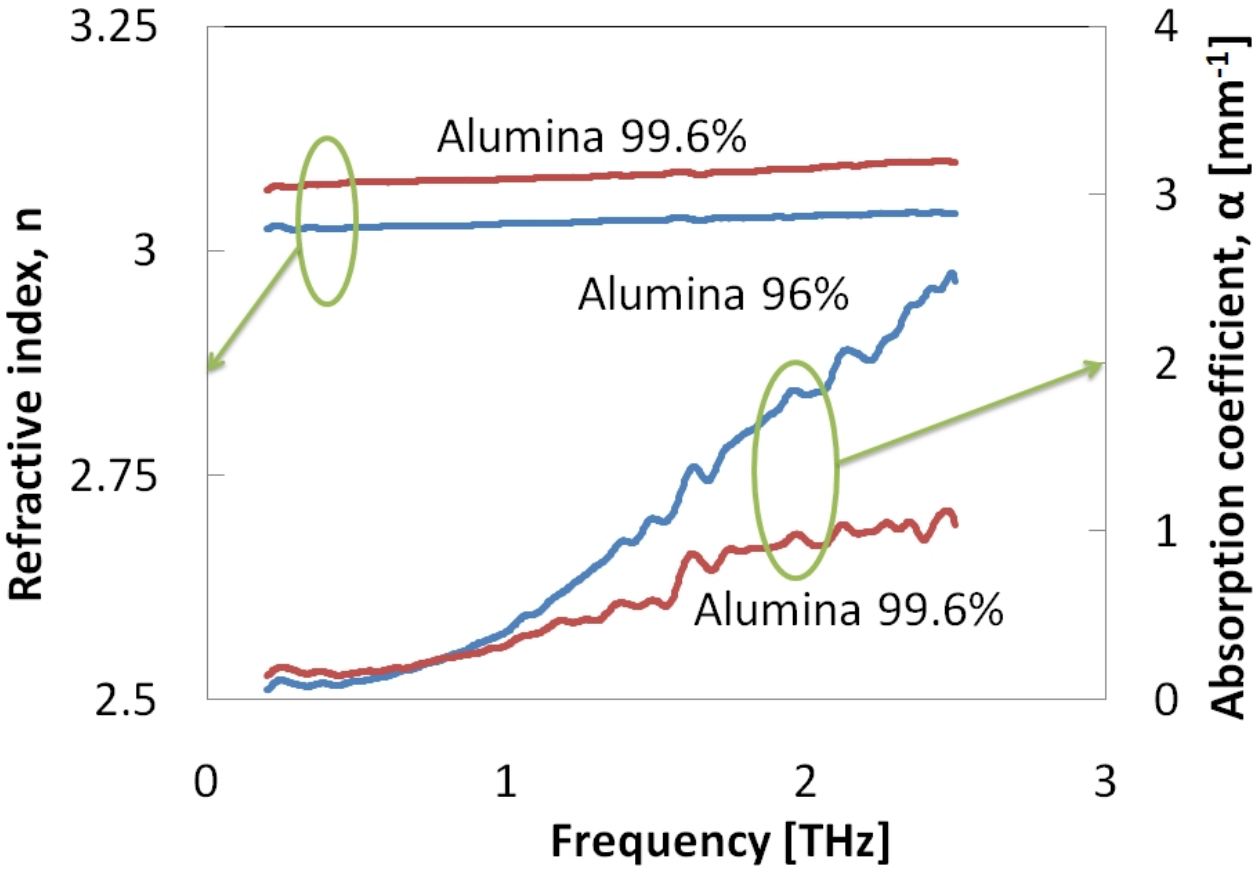

Figure 2.5: Retrieved refractive index, n, and absorption coefficient, α, for two different alumina samples.

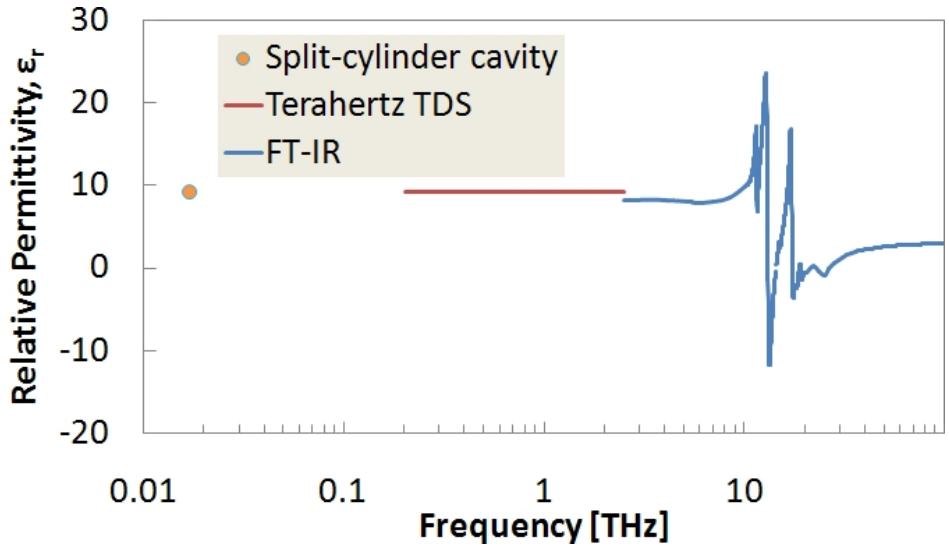

(a) Permittivity of 96% alumina.

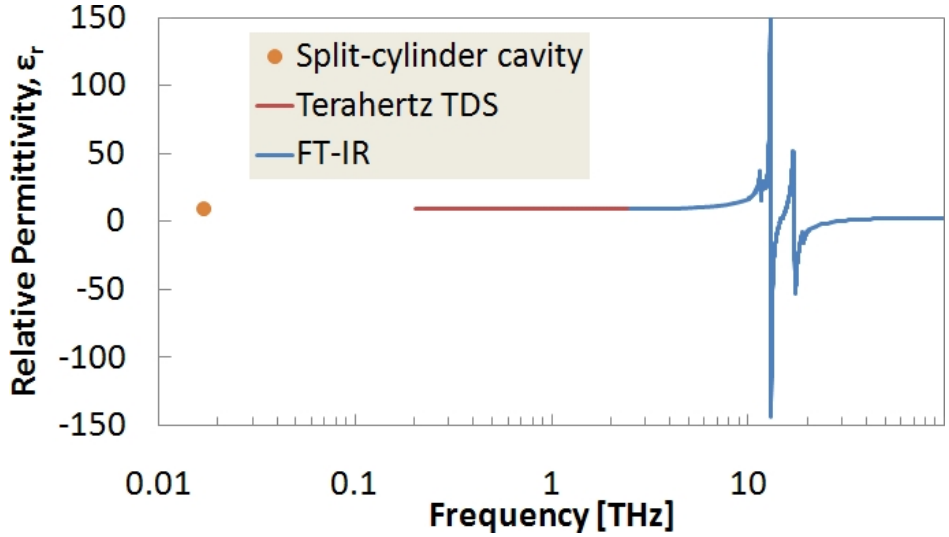

(b) Permittivity of 99.6% alumina.

Figure 2.6: Measurements performed using a split-cylinder cavity, THz TDS, and FTIR.

In Figure 2.6, the real part of the permittivity is plotted for the two different alumina samples. Measurements were performed with terahertz time-domain spectroscopy from around 200 GHz to 2.5 THz. Below these frequencies, a resonant split-cylinder cavity measurement was performed, to obtain the permittivity at 15 GHz. At higher frequencies, Fourier-transform infrared spectroscopy was used to measure the permittivity. There is good correlation between the techniques over the different bands. There is a slight mismatch between the THz TDS and the FTIR measurements of 96% alumina. This can possibly be explained

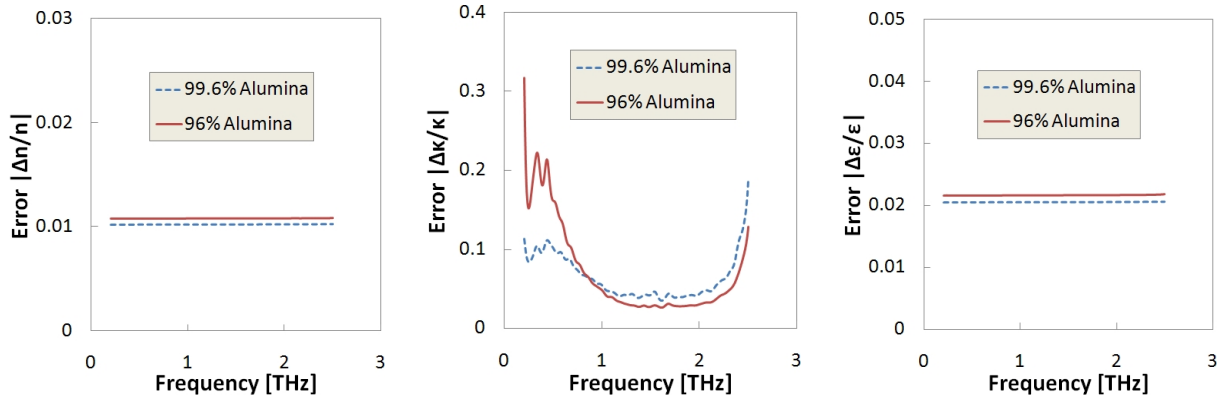

(a) Real part of the refractive index, n.

(b) Imaginary part of the refractive index, κ.

(c) Real part of the permittivity, ϵ.

Figure 2.7: Measurement errors.

by scattering at higher frequencies, which FTIR, being a reflection techniques, is particularly susceptible to. FTIR also relies on complex data fitting and analysis, which may further lead to errors. Nevertheless, it is still important to determine the uncertainty in the THz TDS characterization process.

2.3.2 Error analysis

The uncertainties in the refactive index and the absorption coefficient, Δn and $\Delta\alpha$ respectively, have been derived in [91]. We have modified them to take into account errors due to the sample thickness uncertainty. For a parameter x, the uncertainty may be expressed as:

$$\Delta x = \sqrt{\left(\frac{\partial x}{\partial \varphi}\Delta\varphi\right)^2 + \left(\frac{\partial x}{\partial |t|}\Delta|t|\right)^2 + \left(\frac{\partial x}{\partial d}\Delta d\right)^2}. \tag{2.11}$$

The error Δd is determined by the measurement technique in use. $\Delta\varphi$ and $\Delta|t|$ are obtained from the standard deviation of the measured transmission coefficient $t(p,\omega)$.

In [91] it is shown that

$$\Delta|t(p,\omega)| = \left[\frac{\left\langle |t_N(p,\omega)|^2 \right\rangle}{2}\right]^{1/2} \tag{2.12a}$$

$$\Delta\varphi(p,\omega) = \frac{\Delta|t(p,\omega)|}{|t(p,\omega)|} \tag{2.12b}$$

$$\Delta n = \frac{c|\varphi|}{\omega d}\sqrt{\left(\frac{\Delta\varphi}{\varphi}\right)^2 + \left(\frac{\Delta d}{d}\right)^2} \tag{2.13a}$$

$$\Delta\alpha = \frac{2}{d}\sqrt{\left(\frac{\Delta\,|T|}{|T|}\right)^2 + \left(\frac{\Delta n}{n}\right)^2\left[\frac{(n-1)^2}{(n^2-1)}\right]^2}, \tag{2.13b}$$

where $\langle\cdot\rangle$ denotes the average value of the enclosed function, and $t_N(p,\omega)$ is the noise in the measured transmission.

In Figure 2.7, the calculated errors in the real and imaginary parts of the refractive index, and in the real part of the permittivity, are plotted with frequency. In common with transmission techniques at microwave frequencies, the accuracy is very good for the real part, but the loss measurement succumb to errors, particularly at higher frequencies.

2.3.3 Scattering from complex structures

In addition to the characterization of ceramics, THz TDS can be used to examine the transmission through more complex structures. We have measured the transmission through an array of silicon nitride ($\epsilon_r = 8.9$) spheres, shown in Figure 2.8. The effective representation of composite media is of interest, and so it may be tempting to view the aggregation of spheres as a slab of material, and to extract the effective parameters using the equations in this chapter. However, the scattering from resonant spheres is complex, and may not simply be replaced by a slab. The scattering from multiple spheres will be considered in chapter 3.

2.4 Summary

A terahertz time-domain spectroscopy system was presented that allows the measurement of phase-coherent transmission in the terahertz gap, from around 100 GHz up to around 5 THz. The system was applied towards the characterization of dielectric materials, in order

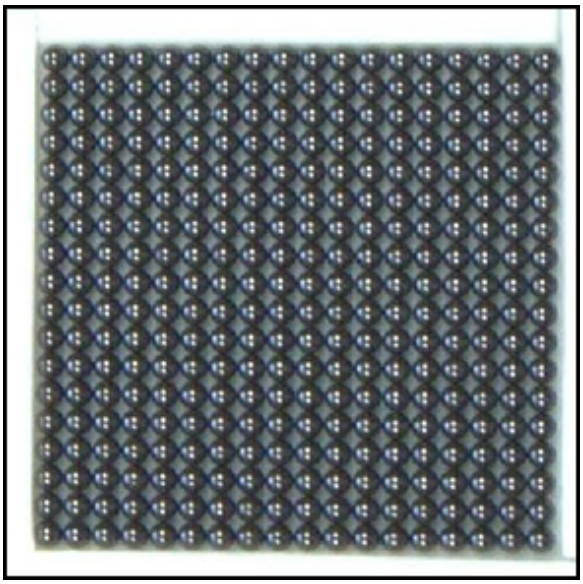

(a) Array of silicon nitride spheres, Si_3N_4.

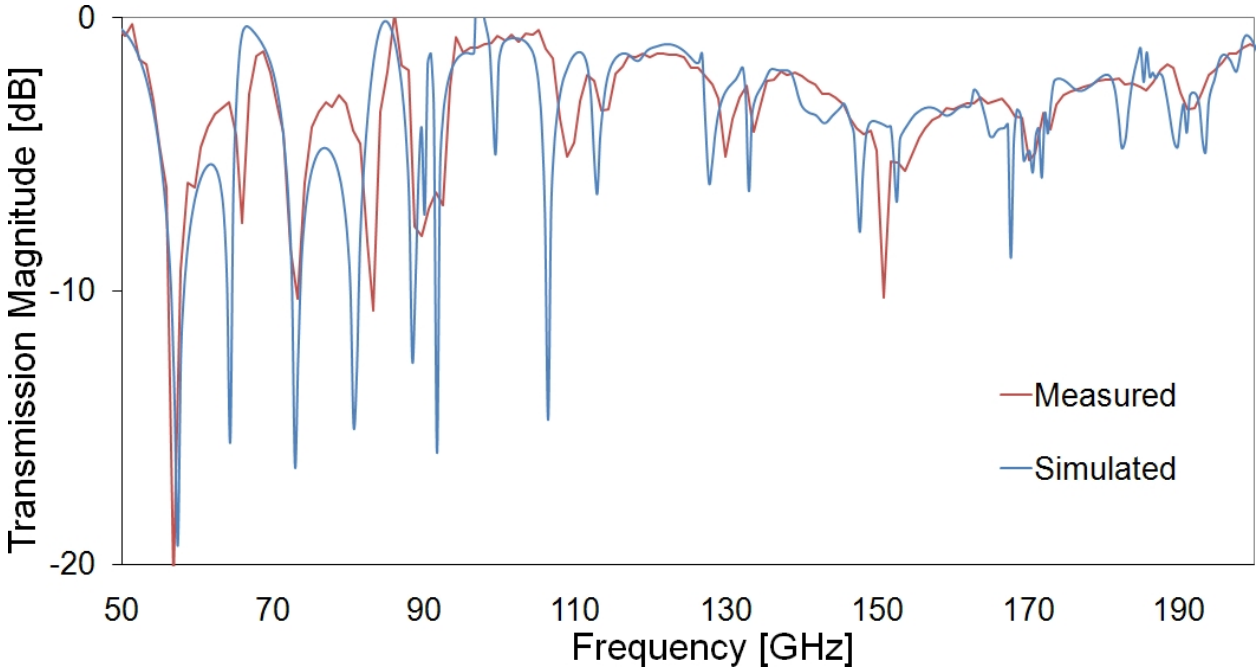

(b) Transmission through the array of spheres.

Figure 2.8: Array of silicon nitride spheres, Si_3N_4, for measurement at terahertz frequencies.

to determine the material parameters, including the permittivity and the loss tangent (or Q), or the refractive index and the absorption coefficient. Error analysis was performed in order to determine the effects of measurement errors. THz TDS was also used to measure the transmission through a composite media formed of arrays of Si_3N_4 spheres.

Chapter 3

Scattering from Aggregates of Spheres

3.1 Introduction

Electromagnetic scattering from spheres has provided a continuous stream of applications and scientific interest, dating back centuries, in part due to its inherent symmetry, as well as its relative agreement with the geometries of many naturally occurring objects. A very early study of the dielectric sphere was performed in Baghdad, in the 11^{th} century, by Ibn al-Haytham [25, 27, 28]. He developed a geometric theory on the multiple reflections of light (which he viewed as small particles) within a spherical lens, which he used as a burning device, and with which he argued that light was produced by an external source and detected by the eye, and not produced by the eye as the ancient Greek Ptolemic theories suggested. Three centuries later, Kamal al-Din al Farisi used Ibn al-Haytham's work to provide an explanation for rainbows [25, 101]. Subsequent investigations of spheres have benefited many fields, including the atmospheric sciences and astronomy [102], numerical electromagnetic code verification, artificial dielectrics [49], and more recently the study of metamaterials [103, 104, 105].

An important contribution to the modern theory of scattering by spheres was produced in 1871 by John Strutt, more popularly known as Lord Rayleigh [106]. Rayleigh scattering is the scattering of light by small particles, with respect to the wavelength, and was used to explain the color of the blue sky [107]. Prior to that, in 1863 Alfred Clebsch had investigated

the scattering by reflecting spheres [108]. The modern formulation of the scattering from spheres is solved using the separation of variables, along with the boundary conditions. These were applied to spheres by Gustav Mie in 1908 [109, 110], however the same results were obtained independently even earlier by Ludvig Lorenz [111], and also by Peter Debye [112]. These formulations were not restricted to just small spheres, but were capable of determining the scattered fields from any sized sphere with any material composition. An important contribution to the formulation of the scattering problem was developed by P. C. Waterman in the 1960's and 70's. Waterman used the Ewald-Oseen extinction theorem, known also as the null field theorem, to develop the transfer, or T-matrix formulation of scattering [113, 114]. This formulation has been particularly beneficial for numerical computation, with the popularization of the digital computer.

The scattering of multiple object significantly complicates matters. Not only must the solution of the objects be determined in isolation, but their mutual interactions are also necessarily found. A solution to the boundary value problem for two spheres has been available as far back as 1935, when Trinks presented his solution for broadside and endfire plane-wave incidence on identical spheres [115]. He employed an *addition theorem* to represent the harmonics around one sphere in terms of the coordinate system of another. However, due to the difficulty in calculating the coefficients of the addition theorems, he was limited to only very small Rayleigh-sized spheres, with radius much less than the wavelength. In 1945 Leslie Foldy presented his *multiple scattering theory* for the approximation of the averaged scalar fields of an ensemble of randomly oriented scatterers [116]. Waterman further developed this averaging theory with his own work on multiple scattering [117] with vector fields. However, exact solutions for scattering from even a small number of particles were difficult to obtain. Work was performed by Victor Twersky, who first studied the two-dimensional problem of two parallel circular cylinders [118], and then provided solutions to multiple scattering theory [119, 120]. These lacked explicit calculations of the scattered fields, but they did provide the rigorous basis for solving the problems. It was the addition theorems of Stein [121] and

Cruzan [122] that laid the foundation for the next series of breakthroughs. Liang and Lo used these addition theorems to provide numerical results for scattering from two metallic spheres [123], followed by Bruning and Lo, who solved the scattering problems of arbitrarily sized dielectric and conducting spheres, at any angle of incidence, and compared the results to measurements [124, 125, 126]. Their results were demonstrated for two or three spheres in a linear array, with the possibility of expanding the technique to an arbitrary number of spheres, again arranged linearly. A key contribution of theirs was the development of an efficient set of recurrence relations for the addition theorems, for translation along the z-axis. These relations significantly decreased the time and effort it took to calculate the addition theorem coefficients.

As computational power increased, later researchers studied scattering from many spheres in various arrangements. Peterson and Ström extended Waterman's T-matrix formulation of scattering to multiple spheres (both acoustic [127] and electromagnetic [128]). Various authors built on this technique, including Lakhtakia [129], who extended the formulation to spheroids. Later on Chew [130, 131, 132] developed a more efficient recursive T-matrix formulation. An extensive review may be found in [133]. In this method, the T-matrix is calculated first for N spheres, after which they are treated as single sphere as the interaction with the $(N+1)$st sphere is calculated. However, violations of the additions theorems are caused when the $(N+1)$st sphere is within the larger sphere encompassing the other N spheres. This leads to inaccuracies, although efforts have been made to reduce these errors by windowing [134]. In addition to these violations, double-truncation of the addition formulas lead to further inaccuracies in the calculated scattered fields, particularly for spheres located in close proximity to one another [135, 136].

In this chapter, a new technique based on the Characteristic Basis Function Method (CBFM) is presented. The CBFM is a procedure for computing computationally large problems by reducing the problem with appropriately selected basis functions [137, 138, 139]. The technique enables one to calculate the scattered fields from any number of spheres, in any

arrangement, and illuminated by an arbitrary incident field. It is shown that the technique is comparable in accuracy to multiple scattering theory; in addition, it is numerically more efficient. The formulation is also conducive to iterative matrix inversion, which can significantly reduce computation time, and allow the determination of extremely large scattering problems.

We will begin the chapter with an introduction to vector spherical basis functions, that are necessary for the representation of the fields in a spherical coordinate system. To guide the reader through the development of the CBFM, the multiple scattering theory will be presented first as a lead-on to the CBF technique. Although the chapter will be mathematically involved, it is designed to highlight the differences between the two approaches, and to provide their physical interpretations. Each technique is presented, first with the simplest case of a single sphere, followed by an extension to the two sphere case, and finally to the general case. This should enable the reader to develop a greater appreciation of the effect of adding additional spheres to an existing system. Once the theoretical background has been developed, computational aspects will be discussed. The incident wave coefficients will be provided, and then far field computation will be discussed. Finally, efficient methods of solving the resulting linear system of equations are presented, along with comparisons between the computational complexities of multiple scattering theory, and the CBFM.

3.1.1 Scalar wave equations

The Helmholtz equation, the time-invariant form of the wave equation, is an elliptic partial differential equation that must be solved to obtain the solution of an electromagnetic boundary value problem.

Although in general we will be dealing with a vector problem, it is nevertheless useful to discuss the scalar Helmholtz equation. As one would expect, the solutions of the scalar and vector equations are closely related, and play a particularly important role in the definition of the scalar and vector transformation operators. We will discuss these shortly, but we remark

here that these operators are critical in the handling of multiple objects in any coordinate system, which is spherical in our case.

The scalar Helmholtz equation is written as,

$$\nabla^2\psi + k^2\psi = 0, \tag{3.1}$$

where ψ is a scalar function, ∇^2 is the scalar Laplacian, and k is the wavenumber.

Using the method of separation of variables, a solution to (3.1) can be expressed as

$$\psi_{mn}(r,\theta,\phi) = z_n^{(J)}(kr)Y_n^m(\theta,\phi). \tag{3.2}$$

For the radial component of the solution, $z_n^{(J)}(kr)$, we choose the appropriate type of spherical Bessel function, viz., $j_n, y_n, h_n^{(1)}$ or $h_n^{(2)}$ for $J = 1, 2, 3$ or 4. $Y_n^m(\theta,\phi)$ is the spherical harmonic function, and forms the angular dependent factor of the solution of (3.1). In this thesis, by convention $\theta \in [0,\pi]$ is the zenith (polar) angle, while $\phi \in [0, 2\pi)$ is the azimuthal angle (see Figure 3.1). Definitions, properties, and recursion relations for efficient calculation of the spherical Bessel and harmonic functions can be found in Appendix A. It is important to note that there are infinitely many solutions to the scalar Helmholtz equation, with $n = 0, \ldots, \infty$ and $m = -n, \ldots, n$.

When one finds a solution, an appropriate coordinate system is selected that effectively represents the geometry in question. For the case of a sphere, this generally means placing the origin of the coordinate system at the center of the sphere. Problems arise when another sphere is brought into the system, since its center will not coincide with the origin of the initial system (providing, of course, that layered spheres are not a concern). To circumvent this problem, the origin of the coordinate system should be translated between the centers of each of the spheres. Fortunately, just such a translation exists, and the details may be found in Appendix B. It is based on the Legendre addition theorem for spherical harmonic,

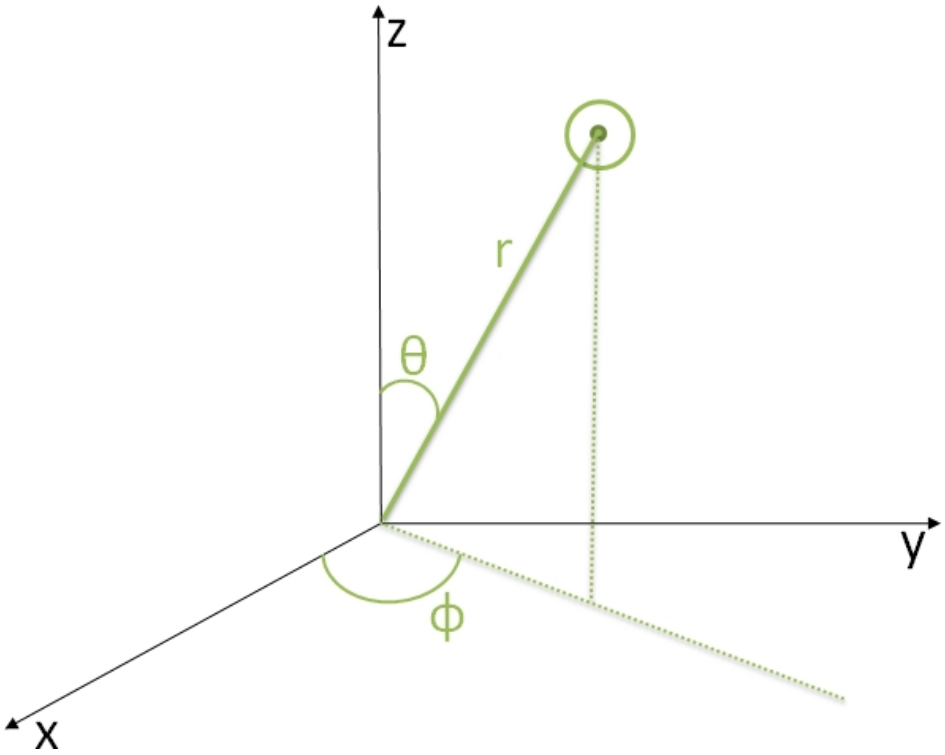

Figure 3.1: Coordinate system, where the location of an observation point is defined by (r, θ, ϕ), where r is the distance, θ is the zenith (polar) angle, and ϕ is the azimuthal angle.

and can be stated as

$$\psi_{mn}^{(J)}(\mathbf{r}_{jx}) = \sum_{\nu=0}^{\infty} \sum_{\mu=-\nu}^{\nu} \psi_{\mu\nu}^{(J)}(\mathbf{r}_{ix}) \beta_{\mu\nu}^{mn}(j, i), \tag{3.3}$$

which implies that a solution in one coordinate system is equivalent to a doubly-infinite summation of solutions in another system, multiplied by the β coefficients. Although closed-form solutions are available for these coefficients, they involve many summations of Wigner $3j$-symbols, that are themselves functions of many double factorials. As a result, the calculation of the required coefficients, using these closed-form solutions, is relatively complex and numerically intensive. A more efficient method would be to use recurrence relations, so that an initial calculated coefficient would recursively generate all the required coefficients. Of the many recurrence relations that have been developed, we have chosen to use the relations presented by Chew [140, 141], because they are both efficient and stable. Further details, including the stating of the recurrence relations used, may be found in Appendix B.

3.1.2 Vector wave equations

As mentioned previously, the electromagnetic problems of interest herein are vectorial in nature. Although the vector equation may be split into a number of scalar equations (see e.g., [142, p. 336]), we will choose to follow Stratton's formulation [143, p. 415] instead and solve the vector form of the Helmholtz equation for $\mathbf{\Psi}$, given by

$$\nabla \times \nabla \times \mathbf{\Psi} - k^2 \mathbf{\Psi} = 0. \tag{3.4}$$

Following Stratton we express the solutions to the above equation in terms of three vector functions, $\mathbf{L}$, $\mathbf{M}$, and $\mathbf{N}$ as follows.

$$\mathbf{L} = \nabla \mathbf{\Psi} \tag{3.5a}$$

$$\mathbf{M} = \nabla \times \mathbf{R}\mathbf{\Psi} = \mathbf{L} \times \mathbf{R} = \frac{1}{k} \nabla \times \mathbf{N} \tag{3.5b}$$

$$\mathbf{N} = \frac{1}{k} \nabla \times \mathbf{M}, \tag{3.5c}$$

where the position vector $\mathbf{R}$ is defined in the (r, θ, ϕ) system as

$$\mathbf{R} = (\hat{\mathbf{r}}, \hat{\boldsymbol{\theta}}, \hat{\boldsymbol{\phi}}). \tag{3.6}$$

Again following Stratton's definitions, we can write the spherical basis vectors explicitly as

$$\mathbf{L}_{mn}^{(J)}(r, \theta, \phi) = \Bigg(\partial_r \big[z_n^{(J)}(kr) \big] Y_n^m(\theta, \phi), \\ , \frac{z_n^{(J)}(kr)}{r} \partial_\theta \big[Y_n^m(\theta, \phi) \big], im \frac{z_n^{(J)}(kr)}{r} \frac{Y_n^m(\theta, \phi)}{\sin \theta} \Bigg) \tag{3.7a}$$

$$\mathbf{M}_{mn}^{(J)}(r, \theta, \phi) = z_n^{(J)}(kr) \cdot \left(0, im \frac{Y_n^m(\theta, \phi)}{\sin \theta}, -\partial_\theta \big[Y_n^m(\theta, \phi) \big] \right) \tag{3.7b}$$

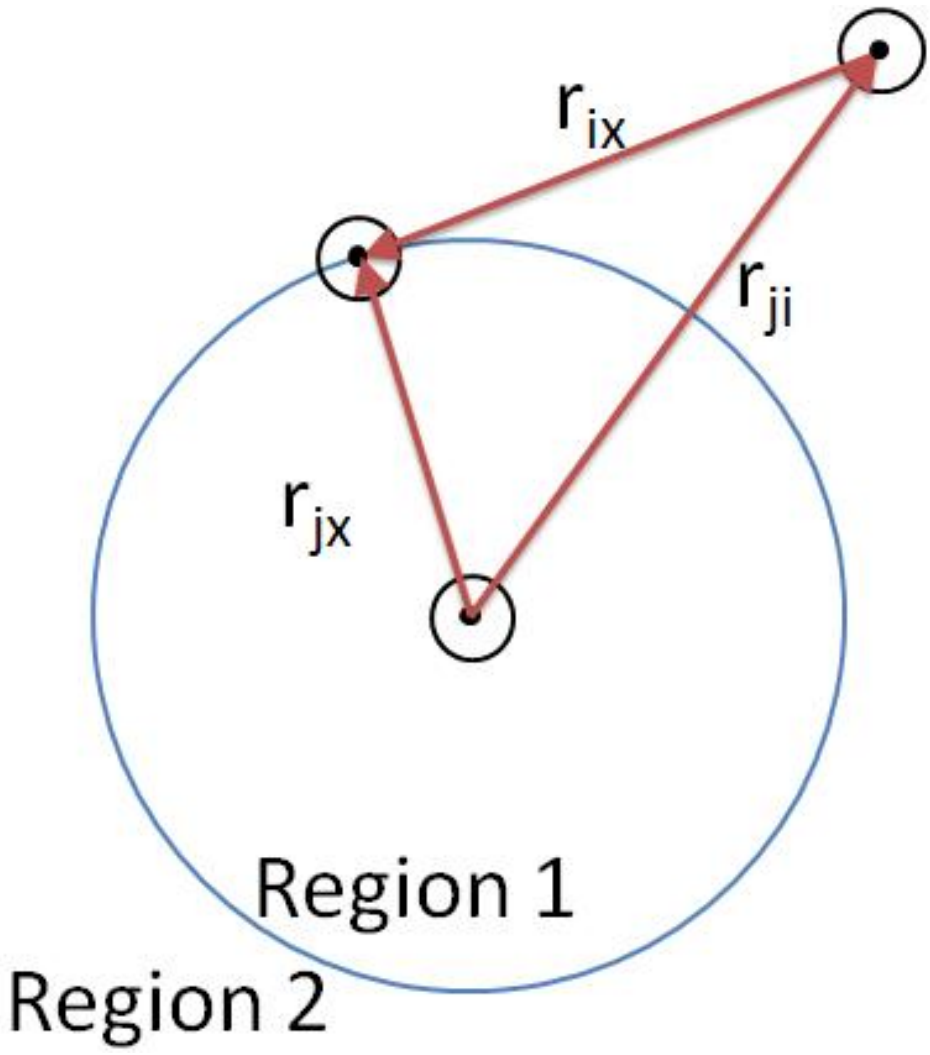

Figure 3.2: Translation of a coordinate system with the observation point x. The origin of the system is translated from a point j to a point i. Translation theorem depends on the region that i is in.

$$\mathbf{N}_{mn}^{(J)}(r,\theta,\phi) = \Bigg(n(n+1)\frac{z_n^{(J)}(kr)}{r} Y_n^m(\theta,\phi), \\ , \frac{\partial_r\big[r z_n^{(J)}(kr)\big]}{kr}\partial_\theta\big[Y_n^m(\theta,\phi)\big], im\frac{\partial_r\big[r z_n^{(J)}(kr)\big]}{kr}\frac{Y_n^m(\theta,\phi)}{\sin\theta}\Bigg). \quad (3.7c)$$

The **L** vector is included only for the sake of completeness. In fact for a divergenceless incident field, as is true in our case, $\mathbf{L} = 0$, and will be neglected from here on.

In analogy to the scalar field solutions, a translation theorem is needed for the **M** and **N** vectors. The vector addition theorem is slightly more complex than the scalar case, in

that it is dependent on whether the field is outgoing ($J = 3$) or regular ($J = 1$), and on the position vector of interest with respect to the two coordinate systems. Below, for example, the translation theorems are given for an outgoing wave that is translated to within region 1 in Figure 3.2. This is the translation theorem that will be used in solving the boundary conditions for the multiple sphere problem.

$$\mathbf{M}_{mn}^{(3)}(\mathbf{r}_{jx}) = \sum_{\nu=1}^{\infty} \sum_{\mu=-\nu}^{\nu} \left[\mathbf{M}_{\mu\nu}^{(1)}(\mathbf{r}_{ix}) A_{\mu\nu}^{mn}(j,i) + \mathbf{N}_{\mu\nu}^{(1)}(\mathbf{r}_{ix}) B_{\mu\nu}^{mn}(j,i) \right] \tag{3.8a}$$

$$\mathbf{N}_{mn}^{(3)}(\mathbf{r}_{jx}) = \sum_{\nu=1}^{\infty} \sum_{\mu=-\nu}^{\nu} \left[\mathbf{M}_{\mu\nu}^{(1)}(\mathbf{r}_{ix}) B_{\mu\nu}^{mn}(j,i) + \mathbf{N}_{\mu\nu}^{(1)}(\mathbf{r}_{ix}) A_{\mu\nu}^{mn}(j,i) \right] \tag{3.8b}$$

The representation of the translation theorems in (3.8a) and (3.8b) is quite unwieldy. It can be presented more succinctly in a matrix form. For translation from a coordinate system i to j, the fields at an observation point x are found using one of:

$$\text{Region 1:} \qquad Ou\boldsymbol{\Psi}(k\mathbf{r}_{jx}) = \bar{\boldsymbol{\alpha}}_{ij} \cdot Rg\boldsymbol{\Psi}(k\mathbf{r}_{ix}) \qquad \text{if } \left|\mathbf{r}_{ix}\right| < \left|\mathbf{r}_{ij}\right| \tag{3.9a}$$

$$\text{Region 2:} \qquad Ou\boldsymbol{\Psi}(k\mathbf{r}_{jx}) = \bar{\boldsymbol{\beta}}_{ij} \cdot Ou\boldsymbol{\Psi}(k\mathbf{r}_{ix}) \qquad \text{if } \left|\mathbf{r}_{ix}\right| > \left|\mathbf{r}_{ij}\right| \tag{3.9b}$$

$$\text{All regions:} \qquad Rg\boldsymbol{\Psi}(k\mathbf{r}_{jx}) = \bar{\boldsymbol{\beta}}_{ij} \cdot Rg\boldsymbol{\Psi}(k\mathbf{r}_{ix}) \qquad \text{if } \forall\left|\mathbf{r}_{ix}\right| \tag{3.9c}$$

where $Rg\boldsymbol{\Psi}$ refers to the regular vector wave function, while $Ou\boldsymbol{\Psi}$ is the outgoing function, and

$$\bar{\boldsymbol{\alpha}}_{ij} = \left(\begin{array}{c|c} \bar{\mathbf{A}}_{ij} & \bar{\mathbf{B}}_{ij} \\ \hline \bar{\mathbf{B}}_{ij} & \bar{\mathbf{A}}_{ij} \end{array} \right) \tag{3.10a}$$

$$\bar{\boldsymbol{\beta}}_{ij} = \left(\begin{array}{c|c} \bar{\mathbf{C}}_{ij} & \bar{\mathbf{D}}_{ij} \\ \hline \bar{\mathbf{D}}_{ij} & \bar{\mathbf{C}}_{ij} \end{array} \right) \tag{3.10b}$$

and

$$\bar{\mathbf{F}} = \overset{mn}{\downarrow}\left(F_{\mu\nu}^{mn}\right)^{\mu\nu\longrightarrow} \tag{3.11a}$$

$$\mathbf{\Psi} = \{\cdots \mathbf{N}_{mn} \cdots \qquad \cdots \mathbf{M}_{mn} \cdots\}^T, \tag{3.11b}$$

where F is any one of A, B, C or D. Recursive relations to find them are again found in Appendix B. Equation (3.9a) is in fact equivalent to (3.8a) and (3.8b) in matrix form. Before we apply these translation theorems for the calculation of the scattered fields from a conglomerate of spheres, we will first derive the scattered fields of a single sphere.

3.2 Multiple scattering theory

3.2.1 Single sphere

Lord Rayleigh's work [107] explaining the color of the blue sky, published in 1899, was based on the scattering of electromagnetic waves off of spheres much smaller than the wavelength. As remarkable as this discovery was, this solution was limited only to small size factors, where the size factor is defined as $x = ka \ll 1$, and where a is the radius of the sphere, and $k = 2\pi/\lambda$ is the wavenumber. However, by the end of the 19^{th} and the beginning of the 20^{th} centuries, Lorenz, Mie and Debye had all independently arrived at full solutions for the scattering from a single homogeneous, isotropic dielectric sphere of any size.

To fully describe the scattering from any number of spheres, we follow a procedure very similar to those used by Lorenz, Mie, and Debye:

1. Represent all incident, scattered, and internal electric and magnetic fields, with unknown coefficients.

2. Enforce the boundary conditions.

3. Use orthogonality relations to obtain a linear system with the relevant number of equations.

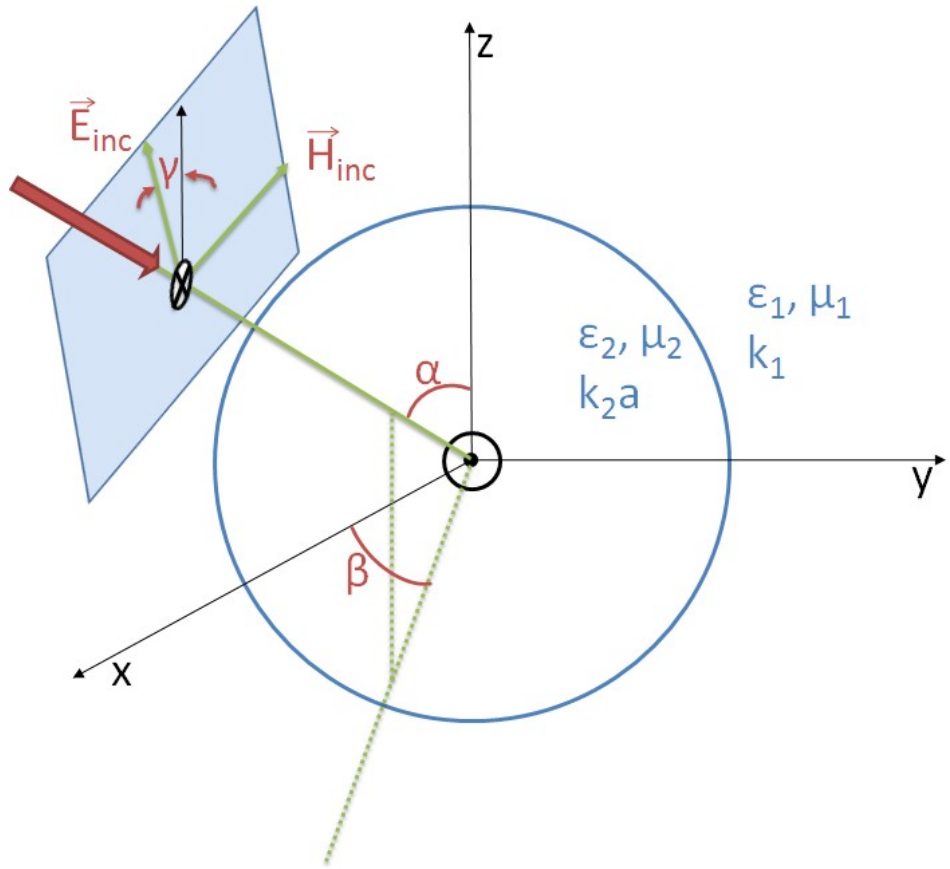

Figure 3.3: Wave incident on a single sphere. Sphere has material characteristics (ϵ_2, μ_2), and radius a. Incident wave is defined by the Euler angles (α, β, γ), where α is the zenith angle, β is the azimuthal angle, and γ represent the polarization with another rotation along the elevation plane.

4. Solve equations for the unknown coefficients.

To demonstrate this procedure, we will first apply it to a single sphere. The geometry of the problem is shown in Figure 3.3.

Step 1: Fields

The electric **E** and magnetic **H** fields can be represented as:

$$\begin{aligned} \mathbf{E}^{\mathbf{inc}} &= \sum_{mn} \left\{ p_{mn} \mathbf{N}_{mn}^{(1)}(k_1 \mathbf{r}) + q_{mn} \mathbf{M}_{mn}^{(1)}(k_1 \mathbf{r}) \right\} \\ &= \mathbf{a_{inc}} \cdot Rg\mathbf{\Psi}(k_1 \mathbf{r}) \end{aligned} \tag{3.12a}$$

$$\begin{aligned}\mathbf{E^{sca}} &= \sum_{mn} \left\{ a_{mn}\mathbf{N}^{(3)}_{mn}(k_1\mathbf{r}) + b_{mn}\mathbf{M}^{(3)}_{mn}(k_1\mathbf{r}) \right\} \\ &= \mathbf{a_{sca}} \cdot Ou\mathbf{\Psi}(k_1\mathbf{r}) \end{aligned} \tag{3.12b}$$

$$\begin{aligned}\mathbf{E^{int}} &= \sum_{mn} \left\{ d_{mn}\mathbf{N}^{(1)}_{mn}(k_2\mathbf{r}) + c_{mn}\mathbf{M}^{(1)}_{mn}(k_2\mathbf{r}) \right\} \\ &= \mathbf{a_{int}} \cdot Rg\mathbf{\Psi}(k_2\mathbf{r}) \end{aligned} \tag{3.12c}$$

$$\mathbf{H^{inc}} = \frac{1}{j\eta_1} \sum_{mn} \left\{ q_{mn}\mathbf{N}^{(1)}_{mn}(k_1\mathbf{r}) + p_{mn}\mathbf{M}^{(1)}_{mn}(k_1\mathbf{r}) \right\} \tag{3.13a}$$

$$\mathbf{H^{sca}} = \frac{1}{j\eta_1} \sum_{mn} \left\{ b_{mn}\mathbf{N}^{(3)}_{mn}(k_1\mathbf{r}) + a_{mn}\mathbf{M}^{(3)}_{mn}(k_1\mathbf{r}) \right\} \tag{3.13b}$$

$$\mathbf{H^{int}} = \frac{1}{j\eta_2} \sum_{mn} \left\{ c_{mn}\mathbf{N}^{(1)}_{mn}(k_2\mathbf{r}) + d_{mn}\mathbf{M}^{(1)}_{mn}(k_2\mathbf{r}) \right\} \tag{3.13c}$$

where

$$\mathbf{a_{inc}} = \left\{ \cdots p_{mn} \cdots \qquad \cdots q_{mn} \cdots \right\}, \tag{3.14}$$

and $\mathbf{\Psi}$ is defined in (3.11b). It is important to note that the p and q coefficients are dependent solely on the nature of the incident wave, and thus are predetermined values. However, we will leave them undefined for now, to preserve the generality of the problem. The coefficients a, b, c, and d are the unknowns to be solved for. With the range of n and m given previously, it would appear that there are an infinite number of coefficients to be determined, however, we can select a truncation point N, where N will determine the largest value of n that will be considered in calculations. It must be selected so as to reduce the errors to within a negligible level. Many such empirical formulas exist, and we will use those

given by Wiscombe ([144]):

$$N = \begin{cases} 1 + x + 4x^{1/3} & \text{if } 0.02 \leq x \leq 8 \\ 2 + x + 4.05x^{1/3} & \text{if } 8 < x < 4200 \\ 2 + x + 4x^{1/3} & \text{if } 4200 \leq x \leq 20,000. \end{cases} \tag{3.15}$$

So with $n = 1 \ldots N$, and $m = -n \ldots n$, we are left with $N(N+2)$ coefficients for each of a, b, c and d, and thus we will need $4 \cdot N(N+2)$ equations to solve them.

Step 2: Boundary conditions

To obtain the relevant number of equations, we make use of the boundary conditions at the interface between the sphere and the surrounding medium. The tangential fields at the interface must be continuous at the surface of the sphere, with

$$\hat{\mathbf{n}} \times \left[\mathbf{E}^{\mathbf{ext}}(a^+) - \mathbf{E}^{\mathbf{int}}(a^-)\right] = 0 \Rightarrow E^{ext}_{(\theta,\phi)}(a^+) = E^{int}_{(\theta,\phi)}(a^-) \tag{3.16a}$$

$$\hat{\mathbf{n}} \times \left[\mathbf{H}^{\mathbf{ext}}(a^+) - \mathbf{H}^{\mathbf{int}}(a^-)\right] = 0 \Rightarrow H^{ext}_{(\theta,\phi)}(a^+) = H^{int}_{(\theta,\phi)}(a^-). \tag{3.16b}$$

We may then use the following boundary conditions:

$$E^{inc}_{(\theta,\phi)}(a) + E^{sca}_{(\theta,\phi)}(a) = E^{int}_{(\theta,\phi)}(a) \tag{3.17a}$$

$$H^{inc}_{(\theta,\phi)}(a) + H^{sca}_{(\theta,\phi)}(a) = H^{int}_{(\theta,\phi)}(a), \tag{3.17b}$$

into which we can substitute (3.12) – (3.13) to yield

$$\sum_{mn}\Bigg\{\Big[p_{mn}N^{(1)}_{mn}(k_1a)+a_{mn}N^{(3)}_{mn}(k_1a)-d_{mn}N^{(1)}_{mn}(k_2a)\Big]+ \\ +\Big[q_{mn}M^{(1)}_{mn}(k_1a)+b_{mn}M^{(3)}_{mn}(k_1a)-c_{mn}M^{(1)}_{mn}(k_2a)\Big]\Bigg\}=0 \tag{3.18a}$$

$$\sum_{mn}\Bigg\{\left[\frac{q_{mn}N^{(1)}_{mn}(k_1a)+b_{mn}N^{(3)}_{mn}(k_1a)}{\eta_1}-\frac{c_{mn}N^{(1)}_{mn}(k_2a)}{\eta_2}\right]+ \\ +\left[\frac{p_{mn}M^{(1)}_{mn}(k_1a)+a_{mn}M^{(3)}_{mn}(k_1a)}{\eta_1}-\frac{d_{mn}M^{(1)}_{mn}(k_2a)}{\eta_2}\right]\Bigg\}=0, \tag{3.18b}$$

where N and M can represent either the θ or ϕ components of their respective vectors.

Step 3: Orthogonality

Next we discuss how to extract $4\cdot N(N+2)$ separate equations from just two equations. The key is that each of those equations is made up of an M and an N component, and each of those two components are a summation of $N(N+2)$ terms. To obtain an equation for each of those terms, we make use of the orthogonality properties of N and M:

$$\Big\langle M^{(J)}_{\mu\nu}(k_ia)\Big|M^{(J')}_{mn}(k_ja)\Big\rangle=\Big[C_Mz^{(J')}_n(k_ja)\Big]\cdot z^{(J)}_n(k_ia)\delta_{m\mu}\delta_{n\nu} \tag{3.19a}$$

$$\Big\langle N^{(J)}_{\mu\nu}(k_ia)\Big|N^{(J')}_{mn}(k_ja)\Big\rangle=\left[C_N\frac{\partial_a\big[z^{(J')}_n(k_ja)\big]}{k_ja}\right]\cdot\frac{\partial_a\big[z^{(J)}_n(k_ia)\big]}{k_ia}\delta_{m\mu}\delta_{n\nu} \tag{3.19b}$$

$$\Big\langle M^{(J)}_{\mu\nu}(k_ia)\Big|N^{(J')}_{mn}(k_ja)\Big\rangle=\Big\langle N^{(J)}_{\mu\nu}(k_ia)\Big|M^{(J')}_{mn}(k_ja)\Big\rangle=0, \tag{3.19c}$$

where

$$\big\langle X\big|Y\big\rangle\equiv\oiint X\cdot Y^*\,\mathrm{d}\Omega. \tag{3.20}$$

C_M and C_N are constants which will cancel out, along with the the other term in the square brackets. The type of spherical Bessel (or Hankel) function (i.e. the selection of J') that

is applied as the orthogonalization operator is not important; after applying orthogonality relationships they will all cancel out leaving only the original spherical Bessel functions. We also note that the relationships are independent of m, and so we can reduce the problem down to one of only $4 \cdot N$ unknowns. Inserting (3.18) into (3.19), we obtain the following linear system of four equations:

$$p_{mn}\partial_a\big[aj_n(k_1a)\big] + a_{mn}\partial_a\big[ah_n^{(1)}(k_1a)\big] - d_{mn}\partial_a\big[aj_n(k_2a)\big] = 0 \tag{3.21a}$$

$$q_{mn}j_n(k_1a) + b_{mn}h_n^{(1)}(k_1a) - c_{mn}j_n(k_2a) = 0 \tag{3.21b}$$

$$\frac{q_{mn}\partial_a\big[aj_n(k_1a)\big] + b_{mn}\partial_a\big[ah_n^{(1)}(k_1a)\big]}{\eta_1} - \frac{c_{mn}\partial_a\big[aj_n(k_2a)\big]}{\eta_2} = 0 \tag{3.21c}$$

$$\frac{p_{mn}j_n(k_1a) + a_{mn}h_n^{(1)}(k_1a)}{\eta_1} - \frac{d_{mn}j_n(k_2a)}{\eta_2} = 0. \tag{3.21d}$$

It should be noted that, to utilize the orthogonality condition, it is in fact possible to use only the spherical harmonic, or it's derivative with respect to θ; as we noted, the spherical Bessel functions that we apply will cancel out, however, for consistency we use the full M and N functions. This procedure of selecting the testing function to be equal to the basis functions is called the Galerkin method [145, p. 692], and we will use this later with the CBFM.

Step 4: Solution

The final step is to solve for the unknown coefficients. This involves rearranging the equations above, to yield

$$a_{mn} = \frac{\mu_2\psi_n(k_1a)\psi_n'(k_2a) - \mu_1\psi_n(k_2a)\psi_n'(k_1a)}{\mu_1\psi_n(k_2a)\xi_n'(k_1a) - \mu_2\xi_n(k_1a)\psi_n'(k_2a)}p_{mn} \tag{3.22a}$$

$$b_{mn} = \frac{\epsilon_2\psi_n(k_1a)\psi_n'(k_2a) - \epsilon_1\psi_n(k_2a)\psi_n'(k_1a)}{\epsilon_1\psi_n(k_2a)\xi_n'(k_1a) - \epsilon_2\xi_n(k_1a)\psi_n'(k_2a)}q_{mn} \tag{3.22b}$$

$$c_{mn} = \frac{\mu_2\big[\psi_n(k_1a)\xi_n'(k_1a) - \xi_n(k_1a)\psi_n'(k_1a)\big]}{\eta_2N_1\psi_n(k_2a)\xi_n'(k_1a) - \eta_1N_2\xi_n(k_1a)\psi_n'(k_2a)}q_{mn} \tag{3.22c}$$

$$d_{mn} = \frac{\mu_2\left[\psi_n(k_1a)\xi_n'(k_1a) - \xi_n(k_1a)\psi_n'(k_1a)\right]}{\mu_1\psi_n(k_2a)\xi_n'(k_1a) - \mu_2\xi_n(k_1a)\psi_n'(k_2a)}p_{mn}, \tag{3.22d}$$

where the Riccati-Bessel functions are

$$\psi(x) = xj_n(x) \tag{3.23a}$$

$$\xi(x) = xh_n^{(1)}(x), \tag{3.23b}$$

and for either of the functions,

$$' \equiv \frac{\partial}{\partial x}. \tag{3.24}$$

Recursion relations for these functions are found in the Appendix A. We are primarily concerned with the a and b coefficients, as these determine the scattered fields.

T-Matrix solution

As with the field representations, it is once again possible to represent the solutions more succinctly in matrix form. As we are dealing with a linear system, we may express the coefficients in terms of a *transfer* matrix, or T-matrix, as follows:

$$\bar{\mathbf{T}}_{\mathbf{sca}} = \left(\begin{array}{cc|cc} \ddots & & & \\ & a_{mn} & & \\ & & \ddots & \\ \hline & & \ddots & \\ & & & b_{mn} \\ & & & & \ddots \end{array}\right). \tag{3.25a}$$

The same is also true for the internal field coefficients:

$$\bar{\mathbf{T}}_{\mathbf{int}} = \left(\begin{array}{cc|cc} \ddots & & & \\ & d_{mn} & & \\ & & \ddots & \\ \hline & & \ddots & \\ & & & c_{mn} \\ & & & & \ddots \end{array}\right). \tag{3.25b}$$

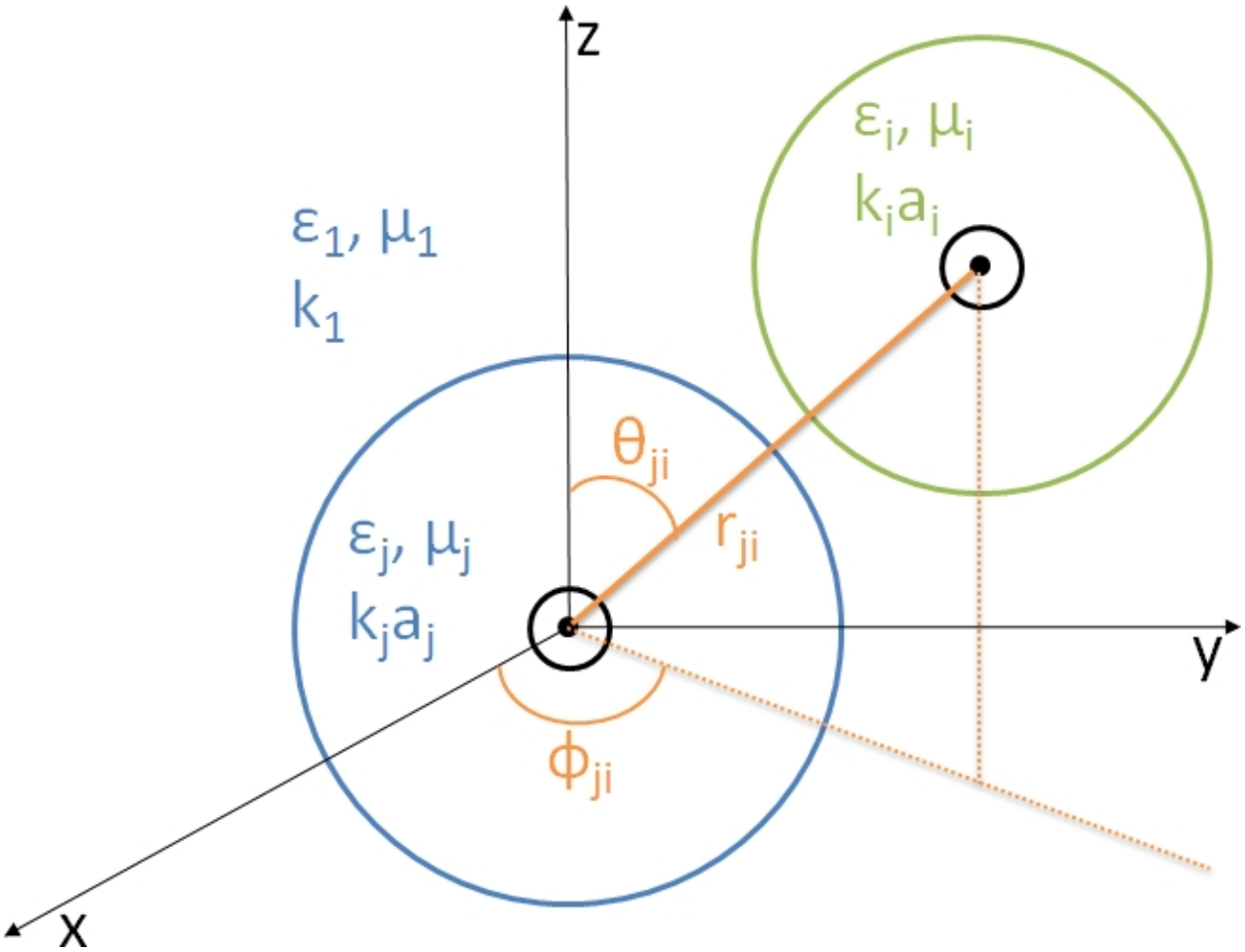

Figure 3.4: Wave incident on a two sphere system. Coordinate system is centered on sphere with material characteristics (ϵ_j, μ_j), and radius a_j. Second sphere has material characteristics (ϵ_i, μ_i), and radius a_i. In the coordinate system of sphere j, sphere i is located at $(r_{ji}, \theta_{ji}, \phi_{ji})$.

This allows us to rewrite (3.12b) and (3.12c), and write the final solutions to the problem as:

$$\mathbf{E}^{\mathbf{sca}} = \mathbf{a}_{\mathbf{inc}} \cdot \bar{\mathbf{T}}_{\mathbf{sca}} \cdot Ou\mathbf{\Psi}(k_1\mathbf{r}) \tag{3.26a}$$

and

$$\mathbf{E}^{\mathbf{int}} = \mathbf{a}_{\mathbf{inc}} \cdot \bar{\mathbf{T}}_{\mathbf{int}} \cdot Rg\mathbf{\Psi}(k_2\mathbf{r}). \tag{3.26b}$$

3.2.2 Two spheres

When a second sphere is introduced to the system, we have the added complexity that the two spheres will couple to each other. Electromagnetic waves will scatter from one sphere to the next, and it is this phenomenon that forms the basis of the multiple scattering theory. The physical idea behind this technique is that the fields scattered from one sphere are considered as secondary incident waves on the other sphere. However the procedure for solving for the unknown coefficients will follow the same four steps as discussed previously.

Step 1: Fields

The electric and magnetic fields are listed below for a sphere j, in the presence of a second sphere i (see Figure 3.4):

$$\begin{aligned}\mathbf{E}^{\mathbf{inc(primary),j}} &= \sum_{mn}\left\{p_{mn}^{(j)}\mathbf{N}_{mn}^{(1)}(k_1\mathbf{r}) + q_{mn}^{(j)}\mathbf{M}_{mn}^{(1)}(k_1\mathbf{r})\right\} \\ &= \mathbf{a}_{\mathbf{inc}}^{(j)} \cdot Rg\mathbf{\Psi}(k_1\mathbf{r}) \end{aligned} \tag{3.27a}$$

$$\begin{aligned}\mathbf{E}^{\mathbf{inc(secondary),j}} &= \sum_{mn}\sum_{\mu\nu}\Bigg\{\Big[a_{mn}^{(i)}A_{\mu\nu}^{mn}(i,j) + b_{mn}^{(i)}B_{\mu\nu}^{mn}(i,j)\Big]\mathbf{N}_{\mu\nu}^{(1)}(k_1\mathbf{r}) + \\ &\quad + \Big[a_{mn}^{(i)}B_{\mu\nu}^{mn}(i,j) + b_{mn}^{(i)}A_{\mu\nu}^{mn}(i,j)\Big]\mathbf{M}_{\mu\nu}^{(1)}(k_1\mathbf{r})\Bigg\} \\ &= \mathbf{a}_{\mathbf{sca}}^{(i)} \cdot \bar{\boldsymbol{\alpha}}_{ij} \cdot Rg\mathbf{\Psi}(k_1\mathbf{r}) \end{aligned} \tag{3.27b}$$

$$\begin{aligned}\mathbf{E}^{\mathbf{sca,j}} &= \sum_{mn}\left\{a_{mn}^{(j)}\mathbf{N}_{mn}^{(3)}(k_1\mathbf{r}) + b_{mn}^{(j)}\mathbf{M}_{mn}^{(3)}(k_1\mathbf{r})\right\} \\ &= \mathbf{a}_{\mathbf{sca}}^{(j)} \cdot Ou\mathbf{\Psi}(k_1\mathbf{r}) \end{aligned} \tag{3.27c}$$

$$\begin{aligned}\mathbf{E}^{\mathbf{int,j}} &= \sum_{mn}\left\{d_{mn}^{(j)}\mathbf{N}_{mn}^{(1)}(k_j\mathbf{r})+c_{mn}^{(j)}\mathbf{M}_{mn}^{(1)}(k_j\mathbf{r})\right\}\\ &= \mathbf{a}_{\mathbf{int}}^{(j)}\cdot Rg\mathbf{\Psi}(k_j\mathbf{r})\end{aligned} \tag{3.27d}$$

$$\mathbf{H}^{\mathbf{inc(primary),j}} = \frac{1}{j\eta_1}\sum_{mn}\left\{q_{mn}^{(j)}\mathbf{N}_{mn}^{(1)}(k_1\mathbf{r})+p_{mn}^{(j)}\mathbf{M}_{mn}^{(1)}(k_1\mathbf{r})\right\} \tag{3.28a}$$

$$\begin{aligned}\mathbf{H}^{\mathbf{inc(secondary),j}} &= \frac{1}{j\eta_1}\sum_{mn}\sum_{\mu\nu}\Bigg\{\Big[a_{mn}^{(i)}B_{\mu\nu}^{mn}(i,j)+b_{mn}^{(i)}A_{\mu\nu}^{mn}(i,j)\Big]\mathbf{N}_{\mu\nu}^{(1)}(k_1\mathbf{r})+\\ &\quad+\Big[a_{mn}^{(i)}A_{\mu\nu}^{mn}(i,j)+b_{mn}^{(i)}B_{\mu\nu}^{mn}(i,j)\Big]\mathbf{M}_{\mu\nu}^{(1)}(k_1\mathbf{r})\Bigg\}\end{aligned} \tag{3.28b}$$

$$\mathbf{H}^{\mathbf{sca,j}} = \frac{1}{j\eta_1}\sum_{mn}\left\{b_{mn}^{(j)}\mathbf{N}_{mn}^{(3)}(k_1\mathbf{r})+a_{mn}^{(j)}\mathbf{M}_{mn}^{(3)}(k_1\mathbf{r})\right\} \tag{3.28c}$$

$$\mathbf{H}^{\mathbf{int,j}} = \frac{1}{j\eta_j}\sum_{mn}\left\{c_{mn}^{(j)}\mathbf{N}_{mn}^{(1)}(k_j\mathbf{r})+d_{mn}^{(j)}\mathbf{M}_{mn}^{(1)}(k_j\mathbf{r})\right\} \tag{3.28d}$$

The scattered and internal fields have the same forms as those for the single sphere case. However, the incident field in this case consists of a primary and a secondary component. The primary incident field for the two sphere case will correspond to the incident field from the single sphere case. The secondary incident field, as described previously, is the scattered field from the other sphere in the system, and it involves the use of translation formulas from either (3.8a) and (3.8b) or (3.9a). The translation involves expressing the scattered fields from sphere i in the coordinates of sphere j. It will also be useful to find the fields at the sphere i, and to do this we simply interchange i and j in the equations above. This leads us to a total of $2\times 4N(N+2)$ unknowns for the problem. To solve for these unknowns, we again go to the step of imposing the boundary conditions.

Step 2: Boundary conditions

We use (3.16) to obtain two boundary conditions at the interface of sphere j:

$$E^{inc(primary),\,j}_{(\theta,\phi)}(a_j) + E^{inc(secondary),\,j}_{(\theta,\phi)}(a_j) + E^{sca,\,j}_{(\theta,\phi)}(a_j) = E^{int,\,j}_{(\theta,\phi)}(a_j) \tag{3.29a}$$

$$H^{inc(primary),\,j}_{(\theta,\phi)}(a_j) + H^{inc(secondary),\,j}_{(\theta,\phi)}(a_j) + H^{sca,\,j}_{(\theta,\phi)}(a_j) = H^{int,\,j}_{(\theta,\phi)}(a_j) \tag{3.29b}$$

Substituting eqs. (3.27) and (3.28) into these we get

$$\begin{aligned}\sum_{mn}\Bigg\{\Bigg[p^{(j)}_{mn}\mathbf{N}^{(1)}_{mn}(k_1a_j) + \sum_{\mu\nu}\Big[a^{(i)}_{mn}A^{mn}_{\mu\nu}(i,j) + b^{(i)}_{mn}B^{mn}_{\mu\nu}(i,j)\Big]\mathbf{N}^{(1)}_{\mu\nu}(k_1a_j) + \\ + a^{(j)}_{mn}\mathbf{N}^{(3)}_{mn}(k_1a_j) - d^{(j)}_{mn}\mathbf{N}^{(1)}_{mn}(k_ja_j)\Bigg] + \\ + \Bigg[q^{(j)}_{mn}\mathbf{M}^{(1)}_{mn}(k_1a_j) + \sum_{\mu\nu}\Big[a^{(i)}_{mn}B^{mn}_{\mu\nu}(i,j) + b^{(i)}_{mn}A^{mn}_{\mu\nu}(i,j)\Big]\mathbf{M}^{(1)}_{\mu\nu}(k_1a_j) + \\ + b^{(j)}_{mn}\mathbf{M}^{(3)}_{mn}(k_1a_j) - c^{(j)}_{mn}\mathbf{M}^{(1)}_{mn}(k_ja_j)\Bigg]\Bigg\}\end{aligned} \tag{3.30a}$$

$$\begin{aligned}\sum_{mn}\Bigg\{\frac{1}{\eta_1}\Bigg[q^{(j)}_{mn}\mathbf{N}^{(1)}_{mn}(k_1a_j) + \sum_{\mu\nu}\Big[b^{(i)}_{mn}A^{mn}_{\mu\nu}(i,j) + a^{(i)}_{mn}B^{mn}_{\mu\nu}(i,j)\Big]\mathbf{N}^{(1)}_{\mu\nu}(k_1a_j) + \\ + b^{(j)}_{mn}\mathbf{N}^{(3)}_{mn}(k_1a_j)\Bigg] - \frac{1}{\eta_j}c^{(j)}_{mn}\mathbf{N}^{(1)}_{mn}(k_ja_j) + \\ + \frac{1}{\eta_1}\Bigg[p^{(j)}_{mn}\mathbf{M}^{(1)}_{mn}(k_1a_j) + \sum_{\mu\nu}\Big[b^{(i)}_{mn}B^{mn}_{\mu\nu}(i,j) + a^{(i)}_{mn}A^{mn}_{\mu\nu}(i,j)\Big]\mathbf{M}^{(1)}_{\mu\nu}(k_1a_j) + \\ + a^{(j)}_{mn}\mathbf{M}^{(3)}_{mn}(k_1a_j)\Bigg] - \frac{1}{\eta_j}d^{(j)}_{mn}\mathbf{M}^{(1)}_{mn}(k_ja_j)\Bigg\}\end{aligned} \tag{3.30b}$$

We can replace j with i to obtain the equivalent conditions for the second sphere. This gives us four boundary conditions, which we can use to obtain the requisite number of equations.

Step 3: Orthogonality

We again apply the orthogonality relations (3.19) to the boundary conditions (3.30), to get the following equations:

$$\partial_a\big[aj_n(k_1a_j)\big]\cdot\left\{p^{(j)}_{mn}+\sum_{\mu\nu}\Big[a^{(i)}_{\mu\nu}A^{\mu\nu}_{mn}(i,j)+b^{(i)}_{\mu\nu}B^{\mu\nu}_{mn}(i,j)\Big]\right\}+$$
$$+a^{(j)}_{mn}\partial_a\big[ah^{(1)}_n(k_1a_j)\big]-d^{(j)}_{mn}\partial_a\big[aj_n(k_ja_j)\big]=0 \quad (3.31a)$$

$$j_n(k_1a_j)\cdot\left\{q^{(j)}_{mn}+\sum_{\mu\nu}\Big[b^{(i)}_{\mu\nu}A^{\mu\nu}_{mn}(i,j)+a^{(i)}_{\mu\nu}B^{\mu\nu}_{mn}(i,j)\Big]\right\}+$$
$$+b^{(j)}_{mn}h^{(1)}_n(k_1a_j)-c^{(j)}_{mn}j_n(k_ja_j)=0 \quad (3.31b)$$

$$\frac{\partial_a\big[aj_n(k_1a_j)\big]}{\eta_1}\cdot\left\{q^{(j)}_{mn}+\sum_{\mu\nu}\Big[b^{(i)}_{\mu\nu}A^{\mu\nu}_{mn}(i,j)+a^{(i)}_{\mu\nu}B^{\mu\nu}_{mn}(i,j)\Big]\right\}+$$
$$+\frac{1}{\eta_1}b^{(j)}_{mn}\partial_a\big[ah^{(1)}_n(k_1a_j)\big]-\frac{1}{\eta_j}c^{(j)}_{mn}\partial_a\big[aj_n(k_ja_j)\big]=0 \quad (3.31c)$$

$$\frac{j_n(k_1a_j)}{\eta_1}\cdot\left\{p^{(j)}_{mn}+\sum_{\mu\nu}\Big[a^{(i)}_{\mu\nu}A^{\mu\nu}_{mn}(i,j)+b^{(i)}_{\mu\nu}B^{\mu\nu}_{mn}(i,j)\Big]\right\}+$$
$$+\frac{1}{\eta_1}a^{(j)}_{mn}h^{(1)}_n(k_1a_j)-\frac{1}{\eta_j}d^{(j)}_{mn}j_n(k_ja_j)=0. \quad (3.31d)$$

Again, we will have the same equations for sphere i by interchanging i and j. It is useful to note that both the primary and secondary incident waves are composed of the same regular fields, hence their coefficients will all have the same multiplicative factor. In the equations above they are collected within curly {}-brackets, and in the solutions they can be dealt with together.

Step 4: Solution

Rearranging the equations above, we can solve for the unknown coefficients. The solutions are identical to the single sphere case, but with the collected primary - and secondary - incident field coefficients replacing the lone incident field coefficients. With $\mathrm{a}_{mn}^{(j)}$ and $\mathrm{b}_{mn}^{(j)}$ representing the single sphere solutions from eq. (3.22), we have:

$$a_{mn}^{(j)} = \mathrm{a}_{mn}^{(j)} \left\{ p_{mn}^{(i)} + \sum_{\mu\nu} \left[a_{\mu\nu}^{(i)} A_{mn}^{\mu\nu}(i,j) + b_{\mu\nu}^{(i)} B_{mn}^{\mu\nu}(i,j) \right] \right\} \tag{3.32a}$$

$$b_{mn}^{(j)} = \mathrm{b}_{mn}^{(j)} \left\{ q_{mn}^{(i)} + \sum_{\mu\nu} \left[b_{\mu\nu}^{(i)} A_{mn}^{\mu\nu}(i,j) + a_{\mu\nu}^{(i)} B_{mn}^{\mu\nu}(i,j) \right] \right\} \tag{3.32b}$$

$$a_{mn}^{(i)} = \mathrm{a}_{mn}^{(i)} \left\{ p_{mn}^{(j)} + \sum_{\mu\nu} \left[a_{\mu\nu}^{(j)} A_{mn}^{\mu\nu}(j,i) + b_{\mu\nu}^{(j)} B_{mn}^{\mu\nu}(j,i) \right] \right\} \tag{3.32c}$$

$$b_{mn}^{(i)} = \mathrm{b}_{mn}^{(i)} \left\{ q_{mn}^{(j)} + \sum_{\mu\nu} \left[b_{\mu\nu}^{(j)} A_{mn}^{\mu\nu}(j,i) + a_{\mu\nu}^{(j)} B_{mn}^{\mu\nu}(j,i) \right] \right\} \tag{3.32d}$$

***T*-Matrix solution**

We can again represent the solution to the problem in a matrix form, using a T-matrix. Not only does this allow a more succinct representation of the solution, but it also provides us with an efficient method of solving for the coefficients. The matrices are comprised of smaller submatrices, each created with the coefficients of the isolated spheres as follows:

$$\bar{\mathbf{T}}_{\mathbf{sca}} = \left(\begin{array}{c|c} \bar{\mathbf{T}}_{\mathbf{sca}}^{(j)} & \\ \hline & \bar{\mathbf{T}}_{\mathbf{sca}}^{(i)} \end{array} \right) \tag{3.33a}$$

$$\mathbf{a}_{\mathbf{inc}} = \left(\begin{array}{c|c} \mathbf{a}_{\mathbf{inc}}^{(j)} & \mathbf{a}_{\mathbf{inc}}^{(i)} \end{array} \right) \tag{3.33b}$$

$$\bar{\boldsymbol{\alpha}} = \left(\begin{array}{c|c} \mathbf{0} & \bar{\boldsymbol{\alpha}}_{ij} \\ \hline \bar{\boldsymbol{\alpha}}_{ji} & \mathbf{0} \end{array}\right). \tag{3.33c}$$

The scattered field is then found as

$$\mathbf{E^{sca}} = \mathbf{a_{inc}} \cdot \bar{\mathbf{T}}_{\mathbf{sca}} \cdot \left[\bar{\mathbf{I}} - \bar{\mathbf{T}}_{\mathbf{sca}} \cdot \bar{\boldsymbol{\alpha}}\right]^{-1} \cdot Ou\boldsymbol{\Psi}_{\mathbf{t}}(k_1\mathbf{r}), \tag{3.34}$$

where $Ou\boldsymbol{\Psi}_{\mathbf{t}}$ is composed by stacking the $Ou\boldsymbol{\Psi}$ vector for each of the spheres. The solution is equivalent to solving for the coefficients in eqs. (3.32a) – (3.32d) and substituting them into (3.27c).

3.2.3 Multiple spheres

For the most general case involving an arbitrary number of spheres, the setup of the problem follows almost exactly the same lines as that for the two-sphere case. The only difference is that secondary field incident on each sphere is made up of the scattered fields from a summation of all other spheres, as opposed to from just one other sphere.

Step 1: Fields

For a system of N_s spheres, the fields on a sphere j in the presence of all other spheres $i = 1 \ldots N_s - 1$ follow the same form as that for the two-sphere case. The primary incident fields, along with the scattered and internal fields can be described using (3.27) and (3.28). The only difference lies with the secondary incident fields, which as mentioned earlier, are

composed of a summation of scattered fields from $N_s - 1$ spheres.

$$\begin{aligned}\mathbf{E}^{\mathbf{inc(secondary)}} &= \sum_i \sum_{mn} \sum_{\mu\nu} \Bigg\{ \Big[a_{mn}^{(i)} A_{\mu\nu}^{mn}(i,j) + b_{mn}^{(i)} B_{\mu\nu}^{mn}(i,j) \Big] \mathbf{N}_{\mu\nu}^{(1)}(k_1\mathbf{r}) + \\ &\quad + \Big[a_{mn}^{(i)} B_{\mu\nu}^{mn}(i,j) + b_{mn}^{(i)} A_{\mu\nu}^{mn}(i,j) \Big] \mathbf{M}_{\mu\nu}^{(1)}(k_1\mathbf{r}) \Bigg\} \\ &= \sum_i \mathbf{a}_{\mathbf{sca}}^{(i)} \cdot \bar{\boldsymbol{\alpha}}_{ij} \cdot Rg\boldsymbol{\Psi}(k_1\mathbf{r}) \end{aligned} \tag{3.35}$$

$$\begin{aligned}\mathbf{H}^{\mathbf{inc(secondary)}} &= \frac{1}{j\eta_1} \sum_i \sum_{mn} \sum_{\mu\nu} \Bigg\{ \Big[a_{mn}^{(i)} B_{\mu\nu}^{mn}(i,j) + b_{mn}^{(i)} A_{\mu\nu}^{mn}(i,j) \Big] \mathbf{N}_{\mu\nu}^{(1)}(k_1\mathbf{r}) + \\ &\quad + \Big[a_{mn}^{(i)} A_{\mu\nu}^{mn}(i,j) + b_{mn}^{(i)} B_{\mu\nu}^{mn}(i,j) \Big] \mathbf{M}_{\mu\nu}^{(1)}(k_1\mathbf{r}) \Bigg\} \end{aligned} \tag{3.36}$$

Step 2: Boundary conditions

Using (3.29),we again obtain expressions that are similar to (3.30), and they read

$$\begin{aligned}\sum_{mn} \Bigg\{ \Bigg[& p_{mn}^{(j)} \mathbf{N}_{mn}^{(1)}(k_1 a_j) + \sum_i \sum_{\mu\nu} \Big[a_{mn}^{(i)} A_{\mu\nu}^{mn}(i,j) + b_{mn}^{(i)} B_{\mu\nu}^{mn}(i,j) \Big] \mathbf{N}_{\mu\nu}^{(1)}(k_1 a_j) + \\ & + a_{mn}^{(j)} \mathbf{N}_{mn}^{(3)}(k_1 a_j) - d_{mn}^{(j)} \mathbf{N}_{mn}^{(1)}(k_j a_j) \Big] + \\ & + \Bigg[q_{mn}^{(j)} \mathbf{M}_{mn}^{(1)}(k_1 a_j) + \sum_i \sum_{\mu\nu} \Big[a_{mn}^{(i)} B_{\mu\nu}^{mn}(i,j) + b_{mn}^{(i)} A_{\mu\nu}^{mn}(i,j) \Big] \mathbf{M}_{\mu\nu}^{(1)}(k_1 a_j) + \\ & + b_{mn}^{(j)} \mathbf{M}_{mn}^{(3)}(k_1 a_j) - c_{mn}^{(j)} \mathbf{M}_{mn}^{(1)}(k_j a_j) \Bigg] \Bigg\} \end{aligned} \tag{3.37a}$$

$$\sum_{mn}\Bigg\{\frac{1}{\eta_1}\Bigg[q_{mn}^{(j)}\mathbf{N}_{mn}^{(1)}(k_1a_j)+\sum_i\sum_{\mu\nu}\Big[b_{mn}^{(i)}A_{\mu\nu}^{mn}(i,j)+a_{mn}^{(i)}B_{\mu\nu}^{mn}(i,j)\Big]\mathbf{N}_{\mu\nu}^{(1)}(k_1a_j)+$$
$$+b_{mn}^{(j)}\mathbf{N}_{mn}^{(3)}(k_1a_j)\Bigg]-\frac{1}{\eta_j}c_{mn}^{(j)}\mathbf{N}_{mn}^{(1)}(k_ja_j)+$$
$$+\frac{1}{\eta_1}\Bigg[p_{mn}^{(j)}\mathbf{M}_{mn}^{(1)}(k_1a_j)+\sum_i\sum_{\mu\nu}\Big[b_{mn}^{(i)}B_{\mu\nu}^{mn}(i,j)+a_{mn}^{(i)}A_{\mu\nu}^{mn}(i,j)\Big]\mathbf{M}_{\mu\nu}^{(1)}(k_1a_j)+$$
$$+a_{mn}^{(j)}\mathbf{M}_{mn}^{(3)}(k_1a_j)\Bigg]-\frac{1}{\eta_j}d_{mn}^{(j)}\mathbf{M}_{mn}^{(1)}(k_ja_j)\Bigg\}. \tag{3.37b}$$

Step 3: Orthogonality

Once again we apply the orthogonality relationships, given in (3.19), to get

$$\partial_a\big[aj_n(k_1a_j)\big]\cdot\Bigg\{p_{mn}^{(j)}+\sum_i\sum_{\mu\nu}\Big[a_{\mu\nu}^{(i)}A_{mn}^{\mu\nu}(i,j)+b_{\mu\nu}^{(i)}B_{mn}^{\mu\nu}(i,j)\Big]\Bigg\}+$$
$$+a_{mn}^{(j)}\partial_a\big[ah_n^{(1)}(k_1a_j)\big]-d_{mn}^{(j)}\partial_a\big[aj_n(k_ja_j)\big]=0 \tag{3.38a}$$

$$j_n(k_1a_j)\cdot\Bigg\{q_{mn}^{(j)}+\sum_i\sum_{\mu\nu}\Big[b_{\mu\nu}^{(i)}A_{mn}^{\mu\nu}(i,j)+a_{\mu\nu}^{(i)}B_{mn}^{\mu\nu}(i,j)\Big]\Bigg\}+$$
$$+b_{mn}^{(j)}h_n^{(1)}(k_1a_j)-c_{mn}^{(j)}j_n(k_ja_j)=0 \tag{3.38b}$$

$$\frac{\partial_a\big[aj_n(k_1a_j)\big]}{\eta_1}\cdot\Bigg\{q_{mn}^{(j)}+\sum_i\sum_{\mu\nu}\Big[b_{\mu\nu}^{(i)}A_{mn}^{\mu\nu}(i,j)+a_{\mu\nu}^{(i)}B_{mn}^{\mu\nu}(i,j)\Big]\Bigg\}+$$
$$+\frac{1}{\eta_1}b_{mn}^{(j)}\partial_a\big[ah_n^{(1)}(k_1a_j)\big]-\frac{1}{\eta_j}c_{mn}^{(j)}\partial_a\big[aj_n(k_ja_j)\big]=0 \tag{3.38c}$$

$$\frac{j_n(k_1 a_j)}{\eta_1} \cdot \left\{ p_{mn}^{(j)} + \sum_i \sum_{\mu\nu} \left[a_{\mu\nu}^{(i)} A_{mn}^{\mu\nu}(i,j) + b_{\mu\nu}^{(i)} B_{mn}^{\mu\nu}(i,j) \right] \right\} +$$
$$+ \frac{1}{\eta_1} a_{mn}^{(j)} h_n^{(1)}(k_1 a_j) - \frac{1}{\eta_j} d_{mn}^{(j)} j_n(k_j a_j) = 0, \quad (3.38d)$$

for a sphere j, where the summation over i represents all other spheres.

Step 4: Solution

The last step is to solve for the unknown coefficients, to derive expressions that are equivalent to (3.32), except for the summation, which is now over all other spheres i.

$$a_{mn}^{(j)} = \mathrm{a}_{mn}^{(j)} \left\{ p_{mn}^{(i)} + \sum_i \sum_{\mu\nu} \left[a_{\mu\nu}^{(i)} A_{mn}^{\mu\nu}(i,j) + b_{\mu\nu}^{(i)} B_{mn}^{\mu\nu}(i,j) \right] \right\} \quad (3.39a)$$

$$b_{mn}^{(j)} = \mathrm{b}_{mn}^{(j)} \left\{ q_{mn}^{(i)} + \sum_i \sum_{\mu\nu} \left[b_{\mu\nu}^{(i)} A_{mn}^{\mu\nu}(i,j) + a_{\mu\nu}^{(i)} B_{mn}^{\mu\nu}(i,j) \right] \right\}. \quad (3.39b)$$

The $\mathrm{a}_{mn}^{(j)}$ and $\mathrm{b}_{mn}^{(j)}$ expressions are again the single sphere scattering coefficients.

$\boldsymbol{T}$-Matrix solution

Following the exact same procedure as we used for the two sphere case, we get the following matrix expressions:

$$\bar{\mathbf{T}}_{\mathbf{sca}} = \begin{pmatrix} \bar{\mathbf{T}}_{\mathbf{sca}}^{(j)} & & & & & \\ & \bar{\mathbf{T}}_{\mathbf{sca}}^{(1)} & & & & \\ & & \ddots & & & \\ & & & \bar{\mathbf{T}}_{\mathbf{sca}}^{(i)} & & \\ & & & & \ddots & \\ & & & & & \bar{\mathbf{T}}_{\mathbf{sca}}^{(N_s-1)} \end{pmatrix} \quad (3.40a)$$

$$\mathbf{a}_{\mathbf{inc}} = \begin{pmatrix} \mathbf{a}_{\mathbf{inc}}^{(j)} & \mathbf{a}_{\mathbf{inc}}^{(1)} & \cdots & \mathbf{a}_{\mathbf{inc}}^{(i)} & \cdots & \mathbf{a}_{\mathbf{inc}}^{(N_s-1)} \end{pmatrix} \quad (3.40b)$$

$$\bar{\boldsymbol{\alpha}} = \begin{pmatrix} \mathbf{0} & \bar{\boldsymbol{\alpha}}_{1j} & \cdots & \bar{\boldsymbol{\alpha}}_{ij} & \cdots & \bar{\boldsymbol{\alpha}}_{(N_s-1)j} \\ \bar{\boldsymbol{\alpha}}_{j1} & \mathbf{0} & \cdots & \bar{\boldsymbol{\alpha}}_{i1} & \cdots & \bar{\boldsymbol{\alpha}}_{(N_s-1)1} \\ \vdots & \vdots & \ddots & \vdots & \ddots & \vdots \\ \bar{\boldsymbol{\alpha}}_{ji} & \bar{\boldsymbol{\alpha}}_{1i} & \cdots & \mathbf{0} & \cdots & \bar{\boldsymbol{\alpha}}_{(N_s-1)i} \\ \vdots & \vdots & \ddots & \vdots & \ddots & \vdots \\ \bar{\boldsymbol{\alpha}}_{j(N_s-1)} & \bar{\boldsymbol{\alpha}}_{1(N_s-1)} & \cdots & \bar{\boldsymbol{\alpha}}_{i(N_s-1)} & \cdots & \mathbf{0} \end{pmatrix}, \tag{3.40c}$$

so that the final expression for the total scattered field can be written:

$$\mathbf{E^{sca}} = \mathbf{a_{inc}} \cdot \bar{\mathbf{T}}_{\mathbf{sca}} \cdot \left[\bar{\mathbf{I}} - \bar{\mathbf{T}}_{\mathbf{sca}} \cdot \bar{\boldsymbol{\alpha}}\right]^{-1} \cdot Ou\boldsymbol{\Psi}_{\mathbf{t}}(k_1\mathbf{r}). \tag{3.41}$$

3.3 Characteristic basis function method (CBFM)

In this section we present a technique that is numerically efficient for calculating the scattered fields of a system of spheres. It achieves the efficiency by reducing the size of the matrix that we need to invert. As mentioned previously, in multiple scattering theory a secondary incident wave on a given is comprised of the fields scattered from all other spheres. The concept is equally valid in the present technique, but the crucial difference that the secondary incident wave will now be decomposed into a multitude of characteristic basis functions. To systematically develop the CBFM, we will, once again begin with a trivial single sphere case, then move onto a two sphere case, and finally, we will address the problem of a completely arbitrary system. The general procedure for solving the problem will still follow the same outline as that of the multiple scattering theory, in that we will begin with the representation of the fields, followed by the imposition of the boundary conditions, then finally use orthogonality relationships to generate the requisite number of linear equations for the unknowns.

3.3.1 Single sphere

Let us begin the demonstration of the CBFM by presenting the trivial case of a single sphere. Although this will reduce to the same problem that we have solved previously in subsection 3.2.1, it will serve to highlight the differences between the methods.

Step 1: Fields

We again proceed to represent the incident, as well as scattered and internal fields for the sphere. The notation used is the same as before, except for the fact that the vector of incident field coefficients $\mathbf{a_{inc}}$, as defined in (3.14), will now have a superscript index, p, because the secondary incident field will now be decomposed into a number of basis functions. The primary incident wave has the index $p = 0$, while for a decomposition of P basis functions, or incident waves, the subsequent waves will have the indices $p = 1 \dots P$. For a single sphere system, we would not expect a secondary incident field as there are no other scatterers. Nevertheless, for any incident plane wave, the T-matrices from (3.25a) and (3.25b) will define the scattered and internal fields due to that wave; hence, the total scattered and internal fields will be represented by a summation of those fields.

$$\mathbf{E^{inc}} = \mathbf{a}_{\mathbf{inc}}^{(0)} \cdot Rg\mathbf{\Psi}(k_1\mathbf{r}) \tag{3.42a}$$

$$\mathbf{E^{sca}} = \sum_p z_p \cdot \mathbf{a}_{\mathbf{inc}}^{(p)} \cdot \bar{\mathbf{T}}_{\mathbf{sca}} \cdot Ou\mathbf{\Psi}(k_1\mathbf{r}) \tag{3.42b}$$

$$\mathbf{E^{int}} = \sum_p z_p \cdot \mathbf{a}_{\mathbf{inc}}^{(p)} \cdot \bar{\mathbf{T}}_{\mathbf{int}} \cdot Rg\mathbf{\Psi}(k_2\mathbf{r}). \tag{3.42c}$$

The incident field is identical to that of (3.12a). As stated previously, the scattered and internal fields are a summation of P scattered and internal fields found using the relevant T-matrices. Every term due to a basis function p will have an unknown coefficient z_p, and we will be solving for these coefficients. Again, for this trivial case there are no secondary incident fields, and so one would expect all z coefficients to equal zero, apart from that

coinciding with the incident wave. I.e., for an incident plane wave, if we select $\mathbf{a}_{\mathbf{inc}}^{(1)} = \mathbf{a}_{\mathbf{inc}}^{(0)}$, then we would expect $z_1 = 1$, and $z_p = 0$ if $p > 1$.

Step 2: Boundary conditions

Using the boundary conditions from (3.17), and substituting in (3.42), we obtain:

$$\mathbf{a}_{\mathbf{inc}}^{(0)} \cdot Rg\Psi_{(\theta,\phi)}(k_1\mathbf{r}) + \sum_p z_p \cdot \mathbf{a}_{\mathbf{inc}}^{(p)} \cdot \bar{\mathbf{T}}_{\mathbf{sca}} \cdot Ou\Psi_{(\theta,\phi)}(k_1\mathbf{r}) = \sum_p z_p \cdot \mathbf{a}_{\mathbf{inc}}^{(p)} \cdot \bar{\mathbf{T}}_{\mathbf{int}} \cdot Rg\Psi_{(\theta,\phi)}(k_2\mathbf{r})$$

$$\Rightarrow \mathbf{a}_{\mathbf{inc}}^{(0)} \cdot Rg\Psi_{(\theta,\phi)}(k_1\mathbf{r}) = \sum_p z_p \cdot \mathbf{a}_{\mathbf{inc}}^{(p)} \cdot \left[\bar{\mathbf{T}}_{\mathbf{int}} \cdot Rg\Psi_{(\theta,\phi)}(k_2\mathbf{r}) - \bar{\mathbf{T}}_{\mathbf{sca}} \cdot Ou\Psi_{(\theta,\phi)}(k_1\mathbf{r})\right]$$

$$= \sum_p z_p \cdot \mathbf{a}_{\mathbf{inc}}^{(p)} \cdot Rg\Psi_{(\theta,\phi)}(k_1\mathbf{r}). \tag{3.43}$$

This indicates that the incident wave can be decomposed into P secondary waves. The question now is, how do we solve for the coefficients of these plane waves, in order to obtain the solution to the problem at hand?

Step 3: Orthogonality

We again use Galerkin's Method to generate a matrix to solve for z_p. So for an incident wave p', the inner product, defined in (3.20), is taken with (3.43) to get:

$$\begin{aligned}\left\langle \mathbf{a}_{\mathbf{inc}}^{(0)} \cdot Rg\Psi_{(\theta,\phi)}(k_1\mathbf{r}) \middle| \mathbf{a}_{\mathbf{inc}}^{(p')} \cdot Rg\Psi_{(\theta,\phi)}(k_1\mathbf{r}) \right\rangle = \\ = \left\langle \sum_p z_p \cdot \mathbf{a}_{\mathbf{inc}}^{(p)} \cdot Rg\Psi_{(\theta,\phi)}(k_1\mathbf{r}) \middle| \mathbf{a}_{\mathbf{inc}}^{(p')} \cdot Rg\Psi_{(\theta,\phi)}(k_1\mathbf{r}) \right\rangle = \\ = \sum_p z_p \cdot \left\langle \mathbf{a}_{\mathbf{inc}}^{(p)} \cdot Rg\Psi_{(\theta,\phi)}(k_1\mathbf{r}) \middle| \mathbf{a}_{\mathbf{inc}}^{(p')} \cdot Rg\Psi_{(\theta,\phi)}(k_1\mathbf{r}) \right\rangle. \quad (3.44)\end{aligned}$$

At this point it is important to note that the wave vectors $\mathbf{a}_{\mathbf{inc}}^{(p)}$ must be made orthogonal to one another. So as to not diverge too much from the present discussion, the methods of orthogonalization will be deferred to a later section. For now, it suffices to say (for now) that the most efficient and stable method is based on the use of the Singular Value Decomposition (SVD) method, which automatically creates an orthonormal basis of vectors. We can define the following function to simplify the relationship between plane waves with the arbitrary indices p and p':

$$\varphi(p', p) = \left\langle \mathbf{a}_{\mathbf{inc}}^{(p)} \cdot Rg\Psi_{(\theta,\phi)}(k_1\mathbf{r}) \middle| \mathbf{a}_{\mathbf{inc}}^{(p')} \cdot Rg\Psi_{(\theta,\phi)}(k_1\mathbf{r}) \right\rangle. \quad (3.45)$$

Step 4: Solution

We are now ready to generate a set of equations whose solution will provide us with the desired coefficients. We can generate the following matrix to solve for z:

$$\bar{\mathbf{\Phi}} \cdot \mathbf{Z} = \mathbf{A}. \quad (3.46)$$

The matrix is generated by forming the inner product for all values of $p' = 1 \ldots P$, and using (3.44) to generate the elements of the $\bar{\bar{\mathbf{\Phi}}}$ matrix as follows:

$$\bar{\bar{\mathbf{\Phi}}} = \begin{pmatrix} \varphi(0,0) & \cdots & \varphi(0,p) & \cdots & \varphi(0,P) \\ \vdots & \ddots & \vdots & \ddots & \vdots \\ \varphi(p',0) & \cdots & \varphi(p',p) & \cdots & \varphi(p',P) \\ \vdots & \ddots & \vdots & \ddots & \vdots \\ \varphi(P,0) & \cdots & \varphi(P,p) & \cdots & \varphi(P,P) \end{pmatrix}. \tag{3.47a}$$

The vector $\mathbf{Z}$ in (3.46) is comprised of the unknown z coefficients, while the vector $\mathbf{A}$ is determined by the incident field:

$$\mathbf{Z} = \begin{pmatrix} z_0 \\ \vdots \\ z_p \\ \vdots \\ z_P \end{pmatrix} \tag{3.47b}$$

$$\mathbf{A} = \begin{pmatrix} \varphi(0,0) \\ \vdots \\ \varphi(p',0) \\ \vdots \\ \varphi(P,0) \end{pmatrix}. \tag{3.47c}$$

By selecting the incident angles so that they are orthogonal to one another, $\bar{\mathbf{\Phi}}$ is reduced to a diagonal matrix:

$$\bar{\mathbf{\Phi}} = \begin{pmatrix} \varphi(0,0) & & & & \\ & \ddots & & & \\ & & \varphi(p',p) & & \\ & & & \ddots & \\ & & & & \varphi(P,P) \end{pmatrix}, \tag{3.48a}$$

and $\mathbf{A}$ is simplified to:

$$\mathbf{A} = \begin{pmatrix} \varphi(0,0) \\ \vdots \\ 0 \\ \vdots \\ 0 \end{pmatrix}. \tag{3.48b}$$

The solution is trivial in this case, with $z_0 \neq 0$, and $z_p = 0$ for $p \neq 0$. However this was expected, with the final expression for the scattered field matching that of (3.26a).

3.3.2 Two spheres

The introduction of a second sphere to the system enables us to examine the treatment of the secondary waves incident on a sphere. Again, these secondary incident waves are a result of the scattered waves from the other sphere in the system. They will be treated as a summation of basis functions, with unknown coefficients.

Step 1: Fields

In a similar manner to the previous section, we will represent the incident field coefficients vector as $\mathbf{a}_{\mathbf{inc}}^{(j)}$. The basis functions will be relabeled as $\mathbf{a}_{\perp}^{(p,j)}$, with $\perp$ representing their orthogonality to one another. Each incident wave has an index p, while a sphere will have

an index j. The index j has been included to account for the variation of the incident wave dependent on the location of the sphere in question. For a sphere j, with the coordinate system origin at its center, and in the presence of another sphere i, the fields are represented as:

$$\mathbf{E}^{\mathbf{inc(primary)}} = \mathbf{a}_{\mathbf{inc}}^{(j)} \cdot Rg\mathbf{\Psi}(k_1\mathbf{r}) \tag{3.49a}$$

$$\mathbf{E}^{\mathbf{inc(secondary)}} = \sum_p z_p^{(i)} \cdot \mathbf{a}_{\perp}^{(p,i)} \cdot \bar{\mathbf{T}}_{\mathbf{sca}}^{(i)} \cdot \boldsymbol{\alpha}_{ij} \cdot Rg\mathbf{\Psi}(k_1\mathbf{r}) \tag{3.49b}$$

$$\mathbf{E}^{\mathbf{sca}} = \sum_p z_p^{(j)} \cdot \mathbf{a}_{\perp}^{(p,j)} \cdot \bar{\mathbf{T}}_{\mathbf{sca}}^{(j)} \cdot Ou\mathbf{\Psi}(k_1\mathbf{r}) \tag{3.49c}$$

$$\mathbf{E}^{\mathbf{int}} = \sum_p z_p^{(j)} \cdot \mathbf{a}_{\perp}^{(p,j)} \cdot \bar{\mathbf{T}}_{\mathbf{int}}^{(j)} \cdot Rg\mathbf{\Psi}(k_j\mathbf{r}). \tag{3.49d}$$

The above representations are similar in form to those of the single sphere case. There is the addition of the secondary incident field, which is the scattered field from sphere i translated to sphere j. The fields in the coordinate system of sphere i are found by interchanging i and j.

Step 2: Boundary conditions

Applying the boundary conditions (3.29), with (3.49) we have:

$$\mathbf{a}_{\mathbf{inc}}^{(j)} \cdot Rg\Psi_{(\theta,\phi)}(k_1\mathbf{r}) + \sum_p z_p^{(i)} \cdot \mathbf{a}_{\perp}^{(p,i)} \cdot \bar{\mathbf{T}}_{\mathbf{sca}}^{(i)} \cdot \bar{\boldsymbol{\alpha}}_{ij} \cdot Rg\Psi_{(\theta,\phi)}(k_1\mathbf{r}) = \sum_p z_p^{(j)} \cdot \mathbf{a}_{\perp}^{(p,j)} \cdot \left[\bar{\mathbf{T}}_{\mathbf{int}}^{(j)} \cdot Rg\Psi_{(\theta,\phi)}(k_j\mathbf{r}) - \bar{\mathbf{T}}_{\mathbf{sca}}^{(j)} \cdot Ou\Psi_{(\theta,\phi)}(k_1\mathbf{r})\right]$$

$$\Rightarrow \mathbf{a}_{\mathbf{inc}}^{(j)} \cdot Rg\Psi_{(\theta,\phi)}(k_1\mathbf{r}) = \sum_p z_p^{(j)} \cdot \mathbf{a}_{\perp}^{(p,j)} \cdot Rg\Psi_{(\theta,\phi)}(k_1\mathbf{r}) - \sum_p z_p^{(i)} \cdot \mathbf{a}_{\perp}^{(p,i)} \cdot \bar{\mathbf{T}}_{\mathbf{sca}}^{(i)} \cdot \bar{\boldsymbol{\alpha}}_{ij} \cdot Rg\Psi_{(\theta,\phi)}(k_1\mathbf{r}). \tag{3.50}$$

The preceding equation states that the fields on each sphere can be decomposed into a

number of basis functions. That will be equivalent to the primary incident wave, in addition to the summation of the plane waves from the other sphere that have scattered onto this one (i.e., the secondary incident waves). Rearranging this, we can express that primary incident wave as in (3.50). It is evident that we will need $2P$ equations to find the coefficients $z_p^{(i)}$ and $z_p^{(j)}$.

Step 3: Orthogonality

We again use Galerkin's Method to generate the $\bar{\bar{\mathbf{\Phi}}}$ matrix. Additionally, we note that all spherical basis functions are regular due to the translation matrix. Thus, during the process of its orthogonalization, $Rg\Psi_{(\theta,\phi)}(k_1\mathbf{r})$ may be neglected. We can therefore define the inner product, in a similar manner to (3.44) for the single sphere case, as

$$\varphi_{(j,i)}(p',p) = \begin{cases} \left\langle \mathbf{a}_\perp^{(p,j)} \middle| \mathbf{a}_\perp^{(p',j)} \right\rangle & \text{if } i = j \\ -\left\langle \mathbf{a}_\perp^{(p,i)} \cdot \bar{\bar{\mathbf{T}}}_{\mathbf{sca}}^{(i)} \cdot \bar{\bar{\boldsymbol{\alpha}}}_{ij} \middle| \mathbf{a}_\perp^{(p',j)} \right\rangle & \text{if } i \neq j, \end{cases} \tag{3.51a}$$

and similarly for the primary incident wave,

$$\varphi_{(j,j)}(p',0) = \left\langle \mathbf{a}^{(j)}{}_{\mathbf{inc}} \middle| \mathbf{a}_\perp^{(p',j)} \right\rangle. \tag{3.51b}$$

Step 4: Solution

The matrix $\bar{\bar{\mathbf{\Phi}}}$ is diagonal for the case of $i = j$

$$\bar{\bar{\mathbf{\Phi}}}_{(j,j)} = \begin{pmatrix} \varphi_{(j,j)}(1,1) & & & & \\ & \ddots & & & \\ & & \varphi_{(j,j)}(p',p) & & \\ & & & \ddots & \\ & & & & \varphi_{(j,j)}(P,P) \end{pmatrix}, \tag{3.52a}$$

but that is not true when $i \neq j$:

$$\bar{\mathbf{\Phi}}_{(i,j)} = \begin{pmatrix} \varphi_{(i,j)}(1,1) & \cdots & \varphi_{(i,j)}(1,p) & \cdots & \varphi_{(i,j)}(1,P) \\ \vdots & \ddots & \vdots & \ddots & \vdots \\ \varphi_{(i,j)}(p',1) & \cdots & \varphi_{(i,j)}(p',p) & \cdots & \varphi_{(i,j)}(p',P) \\ \vdots & \ddots & \vdots & \ddots & \vdots \\ \varphi_{(i,j)}(P,1) & \cdots & \varphi_{(i,j)}(P,p) & \cdots & \varphi_{(i,j)}(P,P) \end{pmatrix}. \tag{3.52b}$$

The matrix

$$\bar{\mathbf{\Phi}} = \left(\begin{array}{c|c} \bar{\mathbf{\Phi}}_{(j,j)} & \bar{\mathbf{\Phi}}_{(i,j)} \\ \hline \bar{\mathbf{\Phi}}_{(j,i)} & \bar{\mathbf{\Phi}}_{(i,i)} \end{array}\right) \tag{3.53a}$$

is thus composed of four submatrices. The two submatrices that form the main diagonal are themselves diagonal, and are each equivalent to the $\bar{\mathbf{\Phi}}$ matrix from the isolated single sphere case. The other two submatrices are dense, and represent the interaction coefficients between the two spheres. Additionally, for each sphere

$$\mathbf{Z}_{(i)} = \begin{pmatrix} z_1^{(i)} \\ \vdots \\ z_p^{(i)} \\ \vdots \\ z_P^{(i)} \end{pmatrix} \tag{3.53b}$$

$$\mathbf{A}_{(i)} = \begin{pmatrix} \varphi_{(i,i)}(1,0) \\ \vdots \\ \varphi_{(i,i)}(p',0) \\ \vdots \\ \varphi_{(i,i)}(P,0) \end{pmatrix}. \tag{3.53c}$$

And so

$$\mathbf{Z} = \begin{pmatrix} \mathbf{Z}_{(j)} \\ \hline \\ \mathbf{Z}_{(i)} \end{pmatrix} \tag{3.54a}$$

$$\mathbf{A} = \begin{pmatrix} \mathbf{A}_{(j)} \\ \hline \\ \mathbf{A}_{(i)} \end{pmatrix}. \tag{3.54b}$$

We can then solve for the unknowns $\mathbf{Z}$ as

$$\mathbf{Z} = \bar{\mathbf{\Phi}}^{-1} \cdot \mathbf{A}. \tag{3.55}$$

3.3.3 Multiple spheres

The two-sphere case will now be extended to the most general case, with an arbitrary (N_s) number of spheres. As with multiple scattering theory, the modification to the two-sphere case will involve only summing the contributions of $N_s - 1$ scattered waves, to form the secondary incident field on a sphere.

Step 1: Fields

The primary incident field, along with the internal and scattered fields, will once again follow the same form as their respective fields from (3.49) in the two-sphere case. The secondary incident fields will, however, be composed of the scattered fields over all other spheres i:

$$\mathbf{E}^{\mathbf{inc(secondary)}} = \sum_i \sum_p z_p^{(i)} \cdot \mathbf{a}_\perp^{(p,i)} \cdot \bar{\mathbf{T}}_{\mathbf{sca}}^{(i)} \cdot \bar{\boldsymbol{\alpha}}_{ij} \cdot Rg\mathbf{\Psi}(k_1\mathbf{r}) \tag{3.56}$$

Step 2: Boundary conditions

As for the two sphere case, we apply the boundary conditions (3.29) to obtain an expression for the fields on sphere j. The fields on a every sphere may be found in a similar manner.

$$\mathbf{a}_{\mathbf{inc}}^{(j)} \cdot Rg\Psi_{(\theta,\phi)}(k_1\mathbf{r}) + \sum_i \sum_p z_p^{(i)} \cdot \mathbf{a}_\perp^{(p,i)} \cdot \bar{\mathbf{T}}_{\mathbf{sca}}^{(i)} \cdot \bar{\boldsymbol{\alpha}}_{ij} \cdot Rg\Psi_{(\theta,\phi)}(k_1\mathbf{r}) =$$
$$\sum_p z_p^{(j)} \cdot \mathbf{a}_\perp^{(p,j)} \cdot \left[\bar{\mathbf{T}}_{\mathbf{int}}^{(j)} \cdot Rg\Psi_{(\theta,\phi)}(k_j\mathbf{r}) - \bar{\mathbf{T}}_{\mathbf{sca}}^{(j)} \cdot Ou\Psi_{(\theta,\phi)}(k_1\mathbf{r})\right]$$

$$\Rightarrow \mathbf{a}_{\mathbf{inc}}^{(j)} \cdot Rg\Psi_{(\theta,\phi)}(k_1\mathbf{r}) = \sum_i \sum_p z_p^{(j)} \cdot \mathbf{a}_\perp^{(p,j)} \cdot Rg\Psi_{(\theta,\phi)}(k_1\mathbf{r})$$
$$- \sum_p z_p^{(i)} \cdot \mathbf{a}_\perp^{(p,i)} \cdot \bar{\mathbf{T}}_{\mathbf{sca}}^{(i)} \cdot \bar{\boldsymbol{\alpha}}_{ij} \cdot Rg\Psi_{(\theta,\phi)}(k_1\mathbf{r}). \quad (3.57)$$

Step 3: Orthogonality

We apply the Galerkin procedure once again. Using the definitions (3.52a) and (3.52b), we have

$$\bar{\boldsymbol{\Phi}} = \begin{pmatrix} \bar{\boldsymbol{\Phi}}_{(1,1)} & \cdots & \bar{\boldsymbol{\Phi}}_{(1,i)} & \cdots & \bar{\boldsymbol{\Phi}}_{(1,N_s)} \\ \vdots & \ddots & \vdots & \ddots & \vdots \\ \bar{\boldsymbol{\Phi}}_{(j,1)} & \cdots & \bar{\boldsymbol{\Phi}}_{(j,i)} & \cdots & \bar{\boldsymbol{\Phi}}_{(j,N_s)} \\ \vdots & \ddots & \vdots & \ddots & \vdots \\ \bar{\boldsymbol{\Phi}}_{(N_s,1)} & \cdots & \bar{\boldsymbol{\Phi}}_{(N_s,i)} & \cdots & \bar{\boldsymbol{\Phi}}_{(N_s,N_s)} \end{pmatrix}. \quad (3.58a)$$

Again, the N_s submatrices that form the main diagonal each represent an isolated sphere's $\bar{\boldsymbol{\Phi}}$ matrix. They are once again diagonal themselves, while the off-diagonal submatrices are not. These submatrices represent the interaction coefficients between the spheres.

Part 4: Solution

Additionally,

$$\mathbf{Z} = \begin{pmatrix} \mathbf{Z}_{(1)} \\ \vdots \\ \mathbf{Z}_{(j)} \\ \vdots \\ \mathbf{Z}_{(N_s)} \end{pmatrix} \tag{3.58b}$$

$$\mathbf{A} = \begin{pmatrix} \mathbf{A}_{(1)} \\ \vdots \\ \mathbf{A}_{(j)} \\ \vdots \\ \mathbf{A}_{(N_s)} \end{pmatrix}. \tag{3.58c}$$

And we can thus solve for the unknown coefficients $\mathbf{Z}$ using (3.55).

3.4 Field computation

3.4.1 The far field approximation

Of primary interest for most applications, and our method of verification of the CBFM, is the scattered field in the far zone region. Once all coefficients have been solved for, the scattered field can be found using, e.g., (3.49c) for the general CBFM case, or (3.41) for the corresponding T-matrix solution. The final remaining task is the expression of the spherical basis vectors in their far field forms, i.e., as $r \to \infty$. Due to the fact that we are dealing solely with the outgoing field, $Ou\mathbf{\Psi}$, this will involve reducing the spherical Hankel function, $h_n^{(1)}$, and its derivative in (3.7b) and (3.7c), into their asymptotic forms,

$$h_n^{(1)}(kr) \simeq \frac{(-j)^n}{jkr} e^{jkr}, \quad kr \to \infty \tag{3.59a}$$

$$\frac{\partial_r \left[r h_n^{(1)}(kr) \right]}{kr} \simeq \frac{(-j)^n}{kr} e^{jkr}, \quad kr \to \infty. \tag{3.59b}$$

Hence, the spherical basis vectors will reduce to,

$$\mathbf{M}^{(3)}_{mn}(r,\theta,\phi) \approx D_{mn}(r) \cdot \left(0, j\tau^m_n(\theta), -\pi^m_n(\theta)\right) \cdot e^{jm\phi} \tag{3.60a}$$

$$\mathbf{N}^{(3)}_{mn}(r,\theta,\phi) \approx D_{mn}(r) \cdot \left(0, j\pi^m_n(\theta), -\tau^m_n(\theta)\right) \cdot e^{jm\phi}, \tag{3.60b}$$

where

$$D_{mn}(r) = (-j)^{2m+n} \cdot \frac{e^{jkr}}{jkr} \cdot \sqrt{\frac{(n-m)!}{(n+m)!} \cdot \frac{2n+1}{4\pi}}. \tag{3.60c}$$

The outgoing fields at a sphere j can then be found, such that,

$$Ou\Psi^{(j)}_{(\theta,\phi)} = Ou\Psi_{(\theta,\phi)} \cdot e^{-j\mathbf{r}\cdot\mathbf{d}_{0j}}. \tag{3.61a}$$

And so the total outgoing field vector, using (3.11b) is,

$$Ou\boldsymbol{\Psi}_{\boldsymbol{t}} = \left\{ \begin{array}{ccccccc} Ou\Psi & Ou\Psi^{(1)} & \cdots & Ou\Psi^{(j)} & \cdots & Ou\Psi^{(N_s-1)} \end{array} \right\}^T, \tag{3.61b}$$

where the observation vector is,

$$\mathbf{r} = r \begin{pmatrix} \sin\theta\cos\phi \\ \sin\theta\sin\phi \\ \cos\theta \end{pmatrix}. \tag{3.61c}$$

Multiple scattering

Substituting (3.61b), along with the incident field coefficients and the T-matrix $\bar{\mathbf{T}}$, into (3.41), we can obtain the scattered fields. Generally though, it is the radar cross-sectional (RCS), σ, that is plotted as a function of angle. This is given as,

$$\sigma(\theta,\phi) = \lim_{r\to\infty} 4\pi r^2 \left| \frac{E_s(r,\theta,\phi)}{E_i(r)} \right|^2. \tag{3.62}$$

CBFM

Once the $z_p^{(j)}$ coefficients have been found, the total scattered field is given by summing the fields from every sphere, and from every basis function, giving

$$\mathbf{E}^{\mathbf{sca}}_{(\theta,\phi)} = \sum_{j=1}^{N_s} \sum_{p=1}^{P} z_p^{(j)} \mathbf{a}_{\perp}^{(p,j)} \cdot \bar{\mathbf{T}}^{(j)}_{\mathbf{sca}} \cdot Ou \mathbf{\Psi}^{(j)}_{(\theta,\phi)}. \tag{3.63}$$

The RCS is then obtained from (3.62).

3.4.2 The incident wave

In the T-matrix and CBFM techniques presented here, the incident field coefficients, p_{mn} and q_{mn} from (3.14) are required to solve a scattering problem for a particular incident wave. A vector plane wave can be decomposed into a summation of spherical waves, using the technique outlined by Stratton [143, p.418-420] and Sarkar [146]. Using the associated Legendre functions, $\tau_n^m(\theta)$ and $\pi_n^m(\theta)$, defined in section A.4, and with the Eulerian incident angles (α, β, γ) from Figure 3.3, the plane wave coefficients at the origin of the coordinate system are,

$$p^0_{mn} = C_{mn} \left[\pi_n^m(\alpha) \cos\gamma + j\tau_n^m(\alpha) \sin\gamma\right] e^{-jm\beta} \tag{3.64a}$$

$$q^0_{mn} = C_{mn} \left[\tau_n^m(\alpha) \cos\gamma + j\pi_n^m(\alpha) \sin\gamma\right] e^{-jm\beta}, \tag{3.64b}$$

where

$$C_{mn} = \frac{j^{2m+n+1}}{n(n+1)} \sqrt{4\pi(2n+1) \cdot \frac{(n-m)!}{(n+m)!}}. \tag{3.64c}$$

Multiple scattering

The incident wave coefficients are required at every sphere. For a source in the far field, this can be approximated by a phase shift factor. Defining $\mathbf{a}^{(\mathbf{0})}_{\mathbf{inc}}$ and $\mathbf{a}^{(\mathbf{i})}_{\mathbf{inc}}$ using (3.14),

$$\mathbf{a}^{(\mathbf{i})}_{\mathbf{inc}} \approx \mathbf{a}^{(\mathbf{0})}_{\mathbf{inc}} \cdot \exp(j\mathbf{k} \cdot \mathbf{d}_{0i}). \tag{3.65}$$

Here, the propagation constant vector $\mathbf{k}$, and direction vector $\mathbf{d}$ are,

$$\mathbf{k} = k_1 \begin{pmatrix} \sin\alpha\cos\beta \\ \sin\alpha\sin\beta \\ \cos\alpha \end{pmatrix}, \qquad \mathbf{d}_{0i} = d_{0i} \begin{pmatrix} \sin\theta_{0i}\cos\phi_{0i} \\ \sin\theta_{0i}\sin\phi_{0i} \\ \cos\theta_{0i} \end{pmatrix}, \tag{3.66}$$

where k_1 is the wavenumber in the background medium, d_{0i} is the distance between the coordinate system origins (i.e. the distance between sphere 0 and sphere i), and the angles (θ_{0i}, ϕ_{0i}) represent the angular location of system i in terms of system 0 (see Figure 3.4, with $j = 0$). The complete incident field coefficient vector, $\mathbf{a_{inc}}$, is then obtained using (3.40b).

CBFM

The incident wave coefficients vectors, $\mathbf{a}_{\mathbf{inc}}^{(j)}$, are found in an identical manner to the multiple scattering theory, using (3.65). However, as we stated previously, the CBFM requires an orthogonal basis of vectors, such that,

$$\left\langle \mathbf{a}_{\perp}^{(p,j)} \middle| \mathbf{a}_{\perp}^{(p',j)} \right\rangle = \begin{cases} \neq 0 & \text{if } p = p' \\ = 0 & \text{if } p \neq p'. \end{cases} \tag{3.67}$$

An obvious solution would be to use a Gram-Schmidt orthogonalization. But, and we will quote from [147, p.74], "Numerically, however, because of the build-up of roundoff errors, naive Gram-Schmidt orthogonalization is *terrible*." The correct procedure, numerically, to form an orthogonal basis, would be to use the singular value decomposition (SVD). In fact, this powerful procedure will provide an orthonormal basis set, while also giving information on which basis vectors may safely be ignored. The SVD will factorize a matrix into the form $\bar{\mathbf{M}} = \bar{\mathbf{U}} \cdot \bar{\mathbf{\Sigma}} \cdot \bar{\mathbf{V}}^H$, where $\bar{\mathbf{V}}^H$ represents the conjugate transpose of the matrix $\bar{\mathbf{V}}$. The columns of the matrix $\bar{\mathbf{U}}$ are the desired orthonormal basis vectors. $\bar{\mathbf{\Sigma}}$ is a diagonal matrix in which the entries are singular values that correspond to the vectors in $\bar{\mathbf{U}}$. These act as

gain terms, such that the vectors corresponding to the small singular values can be ignored. Generally, a cutoff value is selected, with vectors corresponding to smaller values discarded.

One may ask, is it necessary to use an SVD to achieve an orthonormal basis? Why would one not just use a standard basis, i.e. $\{(1,0,0,\cdots),(0,1,0,\cdots),(0,0,1,\cdots),\cdots\}$? The reasoning for using the standard basis would be that, not only would this remove the need to perform an SVD, but it may make more physical sense to create an orthonormal basis out of the different spherical harmonics. Additionally, the T-matrices themselves are independent of the form of any incident wave, while the problem in general, being of spherical geometry, certainly will not have any predisposition to a basis of plane waves. In fact, we find that on substituting the standard basis into the requisite equations, and taking $P = 2N(N+2)$, then it is easily shown that (3.55) will become (3.41). What this means is that the CBFM is exactly equal to the multiple scattering theory, in the case that we choose an equal number of basis functions to the number of spherical harmonics. This is demonstrated in Figure 3.5, where the effect of reducing the number of basis functions is demonstrated. The multiple scattering case consists of 720 harmonic modes. However, even reducing this down to 600 basis functions leaves only a negligible error. With less than half the harmonics kept, at $P = 350$, errors are still below 1%, although at $P = 300$ the swiftly increase to significant levels.

By reducing the number of basis functions, however, the problem can be more efficiently computed. This will be discussed in more detail in a later section on computational complexity. However for now, it would be of interest to compare the use of the standard basis functions, with the use of plane waves. In Figure 3.6, it is evident that the calculations performed using plane waves will diverge a lot more rapidly than those performed using the standard basis functions. The standard basis function calculation will still provide good results using only 107 basis functions. However, the use of even 174 plane waves will result in inaccurate calculations. Thus our hypothesis that the harmonics should provide fastest convergence of the scattered fields is correct. Nevertheless, the scattering of spheres is an

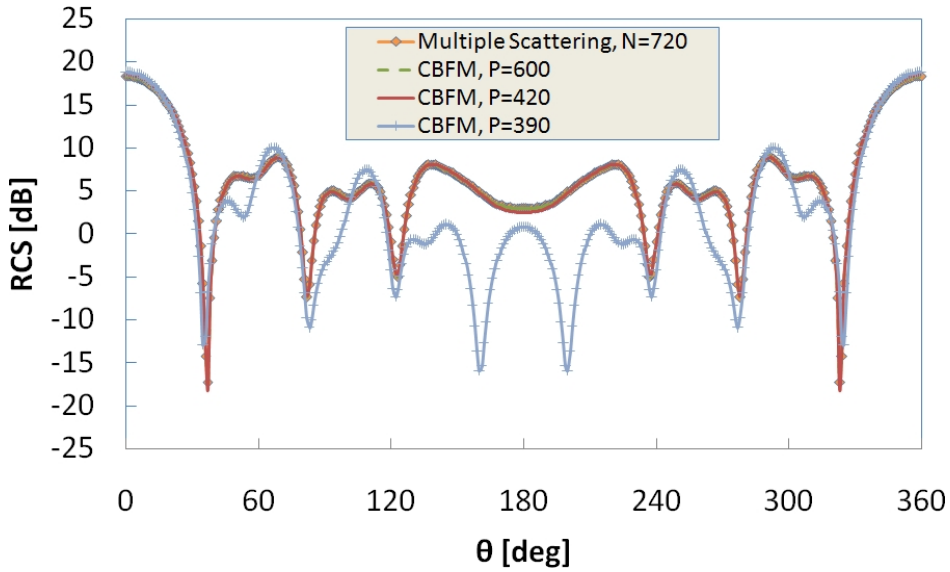

(a) RCS calculated using multiple scattering theory, and using CBFM with varying numbers of basis functions.

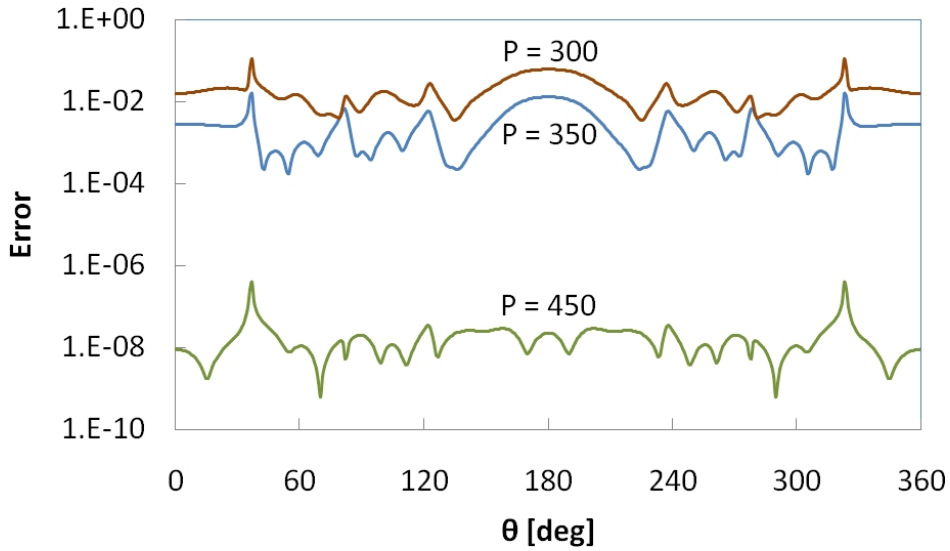

(b) Error in RCS calculated with CBFM, compared to multiple scattering.

Figure 3.5: Divergence of RCS calculated with CBFM, as the number of basis functions is decreased. The system consists of three linearly arranged spheres, each with $ka = \pi$, or $a = \lambda/2$. The spheres have a relative permittivity of $\epsilon_r = 3$, and the lattice spacing is $kd = 3ka$. The incidence is endfire, and the θ component of the electric field is displayed here.

idealized situation, and with more complex geometries, the plane waves would certainly have use.

Of additional interest is the effect that various parameters will have on the number of

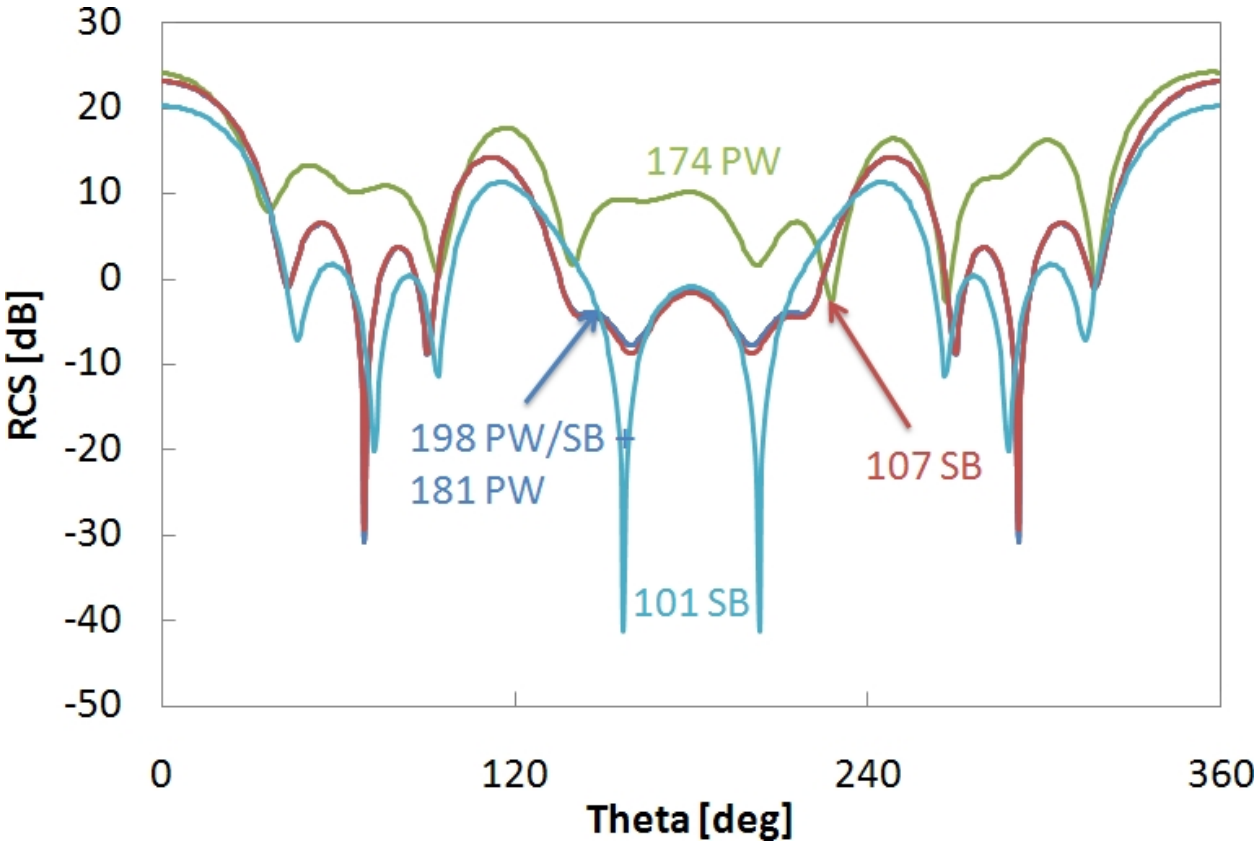

Figure 3.6: Scattering cross section (RCS) of four touching spheres, in a linear array, and with endfire incidence along the z-axis. The identical spheres each have a size factor of $ka = 2$, and a relative permittivity of $\epsilon_r = 3$. The computations are performed using both the standard basis functions, and by using plane waves. With $P = 107$, the standard basis functions still converge well to the correct solution. However, with plane waves, the results rapidly diverge when $P = 174$.

basis functions required to attain a certain level of accuracy. Table 3.1 shows the number of basis functions required to achieve a better than 0.1%, 1%, and 10% error level, as compared to when all basis functions are used. Different parameters are varied (the varying parameter is bolded in the table). It appears, however, that apart from the size factor and the number of spheres, the other parameters have little effect. The parameters varied were the incident angle and polarization, the seperation distance, and the permittivity, but there appears to be no correlation to the required number of basis functions.

Regardless of the choice of basis functions, we can now give the final form of the problem.

We may define an inner product of two vectors, $\mathbf{a}$ and $\mathbf{b}$, as the dot product,

$$\big\langle \mathbf{a} \big| \mathbf{b} \big\rangle \equiv \mathbf{a} \cdot \mathbf{b}^*. \tag{3.68}$$

Table 3.1: Number of basis functions, P, required for varying levels of accuracy with respect to the multiple scattering solution, as different parameters are varied.

Size factor,	Spheres,	Separation,	Permittivity,	Incident angle		Harmonics	N_sP for error		
ka	N_s	kd	ϵ_r	α	γ	$2N_sN(N+2)$	0.1%	1%	10%
1	**2**	2	3	0	0	192	110	110	102
		50					118	110	100
1	**10**	2	3	0	0	960	550	550	510
		50					610	550	510
1	2	2	3	**90**	**0**	192	112	112	102
				90	**90**		122	110	102
π	2	2	**3**	90	90	480	354	304	284
			10				390	340	286
			100				358	308	286

For an orthonormal set of vectors, we may rewrite (3.51a) as,

$$\varphi_{(j,i)}(p',p) = \begin{cases} \delta_{pp'} & \text{if } i = j \\ -\mathbf{a}_\perp^{(p,i)} \cdot \bar{\mathbf{T}}_{\mathbf{sca}}^{(i)} \cdot \bar{\boldsymbol{\alpha}}_{ij} \cdot \left(\mathbf{a}_\perp^{(p',j)}\right)^H & \text{if } i \neq j, \end{cases} \tag{3.69}$$

where $\mathbf{a}_\perp^{(p,i)} = \mathbf{a}_\perp^{(p,i)} \exp(j\mathbf{k} \cdot \mathbf{d}_{0i})$, such that (3.52a) will become $\bar{\bar{\mathbf{\Phi}}}_{(j,j)} = \bar{\mathbf{I}}$, where $\bar{\mathbf{I}}$ is a $P \times P$ identity matrix. (3.52b) is also filled in using (3.69), so that the entire $\bar{\bar{\mathbf{\Phi}}}$ matrix from (3.58a) is determined. In a similar manner, (3.51b) will become,

$$\varphi_{(j,j)}(p',0) = \mathbf{a}_{\mathbf{inc}}^{(j)} \cdot \left(\mathbf{a}_\perp^{(p',j)}\right)^H, \tag{3.70}$$

and so $\mathbf{A}$, from (3.58c), may be fully determined as well. The $\mathbf{Z}$ coefficient can now be found using (3.55).

It should be noted that the sphere scattering solutions in this chapter are not, of course, limited to just incident plane waves; as long as the relevant incident field coefficients can be found for an arbitrary profile, then it may be used as an excitation. Gaussian beams decompositions, for example, are examined in [148, 149, 150].

3.4.3 Solving a linear system of equations

The bulk of the computational expense in solving the scattering problems in this chapter, is the inversion of the matrices $\bar{\mathbf{\Phi}}$, for the CBFM, or $[\bar{\mathbf{I}} - \bar{\mathbf{T}}_{\mathbf{sca}} \cdot \bar{\boldsymbol{\alpha}}]$, for the multiple scattering technique. The most obvious solution would be to use Gauss-Jordan elimination (also know as "Gaussian elimination," which strictly speaking refers to a different technique) [147, p. 41]. Although this technique works well, and is very stable, is it in fact the best method to use? Gauss-Jordan elimination generally requires N^3 operations for the inversion of an $N \times N$ matrix. We will investigate two other algorithms for solving linear systems of equations; LU decomposition and the Strassen formulas, and then determine whether they are more efficient, and suitable for these scattering problems.

LU decomposition

The LU decomposition expresses a matrix $\bar{\mathbf{M}}$ as the product of an upper diagonal matrix $\bar{\mathbf{U}}$, and a lower diagonal matrix $\bar{\mathbf{L}}$, such that,

$$\bar{\mathbf{M}} = \bar{\mathbf{L}} \cdot \bar{\mathbf{U}}. \tag{3.71a}$$

So, for example, a 3×3 matrix $\bar{\mathbf{M}}$ can be decomposed as,

$$\begin{bmatrix} M_{11} & M_{12} & M_{13} \\ M_{21} & M_{22} & M_{23} \\ M_{31} & M_{32} & M_{33} \end{bmatrix} = \begin{bmatrix} L_{11} & 0 & 0 \\ L_{21} & L_{22} & 0 \\ L_{31} & L_{32} & L_{33} \end{bmatrix} \cdot \begin{bmatrix} U_{11} & U_{12} & U_{13} \\ U_{21} & U_{22} & 0 \\ U_{31} & 0 & 0 \end{bmatrix} \tag{3.71b}$$

The procedure for performing an LU decomposition is quite standard in most numerical computation packages, and so for details the readers are referred to [147, p. 48]. Once the decomposition has been performed though, it makes the solution of a linear system very straightforward. It is easily shown that a linear set, such as the CBFM equation $\bar{\mathbf{\Phi}} \cdot \mathbf{Z} = \mathbf{A}$ can be broken up into two successive linear sets, by solving first for the intermediate vector $\mathbf{y}$,

$$\bar{\mathbf{L}} \cdot \bar{\mathbf{y}} = \bar{\mathbf{A}}, \tag{3.72a}$$

and then solving for $\mathbf{Z}$,

$$\bar{\mathbf{U}} \cdot \bar{\mathbf{Z}} = \bar{\mathbf{y}}. \tag{3.72b}$$

Although there are now two sets of linear equations to solve, the problem is in fact greatly simplified, as the triangular matrices allow the coefficients to be solved for algebraically, using forward and backsubstitution. (3.72a) is first solved as,

$$\begin{aligned} y_1 &= \frac{A_1}{L_{00}} \\ y_i &= \frac{1}{L_{ii}} \left[A_i - \sum_{j=1}^{i-1} L_{ij} y_j \right] \quad i = 2, 3, \cdots, N, \end{aligned} \tag{3.73a}$$

and then the coefficients of $\mathbf{Z}$ can be solved for as,

$$\begin{aligned} Z_N &= \frac{A_N}{U_{NN}} \\ Z_i &= \frac{1}{U_{ii}} \left[Z_i - \sum_{j=i+1}^{N} U_{ij} Z_j \right] \quad i = N-1, N-2, \cdots, 1. \end{aligned} \tag{3.73b}$$

The advantage of this technique is that we do not, in fact, have to perform a matrix inversion. The LU decomposition will give us the solution to the linear set, requiring only $\frac{1}{3}N^3$ operations. This is three times less than if were to perform an inversion using Gauss-Jordan elimination. Additionally, the LU decomposition may still be used to easily solve the set for different values of the vector $\mathbf{A}$, and so that benefit of the T-matrix techniques is not lost.

The Strassen formulas

In his seminal paper, published in 1967, Volker Strassen showed that Gauss-Jordan elimination is not, in fact, optimal for matrix multiplication and inversion [151]. He demonstrated efficient techniques that were of order $O(N^{\log_2 7}) \approx O(N^{2.808})$. For smaller matrices, there is little benefit to this technique as the size of the constant in front of the power term is much larger than with Gauss-Jordan elimination. However, depending on the numerical implementation and the hardware used, the Strassen algorithm can see substantial computational savings. Of most benefit to us is the inversion algorithm. For the inversion of a matrix $\bar{\mathbf{M}}$, it is first split up into four smaller block matrices,

$$\bar{\mathbf{M}} = \left[\begin{array}{c|c} \bar{\mathbf{A}} & \bar{\mathbf{B}} \\ \hline \bar{\mathbf{C}} & \bar{\mathbf{D}} \end{array}\right], \tag{3.74}$$

where $\bar{\mathbf{A}} \in \mathbb{C}^{\,m\times m}$, $\bar{\mathbf{B}} \in \mathbb{C}^{\,m\times n}$, $\bar{\mathbf{C}} \in \mathbb{C}^{\,n\times m}$, and $\bar{\mathbf{D}} \in \mathbb{C}^{\,n\times n}$. The inversion may be found as,

$$\bar{\mathbf{M}}^{-1} = \left[\begin{array}{c|c} \bar{\mathbf{A}}^{-1} + \bar{\mathbf{A}}^{-1}\bar{\mathbf{B}}(\bar{\mathbf{D}} - \bar{\mathbf{C}}\bar{\mathbf{A}}^{-1}\bar{\mathbf{B}})^{-1}\bar{\mathbf{C}}\bar{\mathbf{A}}^{-1} & -\bar{\mathbf{A}}^{-1}\bar{\mathbf{B}}(\bar{\mathbf{D}} - \bar{\mathbf{C}}\bar{\mathbf{A}}^{-1}\bar{\mathbf{B}})^{-1} \\ \hline -(\bar{\mathbf{D}} - \bar{\mathbf{C}}\bar{\mathbf{A}}^{-1}\bar{\mathbf{B}})^{-1}\bar{\mathbf{C}}\bar{\mathbf{A}}^{-1} & (\bar{\mathbf{D}} - \bar{\mathbf{C}}\bar{\mathbf{A}}^{-1}\bar{\mathbf{B}})^{-1} \end{array}\right]. \tag{3.75}$$

There are now two smaller matrices that have to be inverted, and less operations overall. The approach we take to matrix inversion is, in fact, to divide $\bar{\mathbf{M}}$ into $P \times P$ smaller matrices, each of size $n \times n$, such that $N = nP$. This division is conducive to a recursive method,

in which we can begin with the inversion of the top left $n \times n$ matrix, and then use this to find the inversion of the $2n \times 2n$ matrix of which it is a part, which in turn may be used to solve for the inversion of the $3n \times 3n$ matrix, and so on until the entire $Pn \times Pn$ matrix has been inverted. As an example, a recursive approach to obtaining a $3n \times 3n$ matrix is shown below, where $\bar{\mathbf{Q}}^{(i)}$ is the i_{th} iteration of the inversion process, with $\bar{\mathbf{Q}}^{(3)}$ giving the inversion of the entire matrix.

$$\begin{bmatrix} \bar{\mathbf{Q}}_{11}^{(1)} & & \\ & & \\ & & \end{bmatrix} \longrightarrow \begin{bmatrix} \bar{\mathbf{Q}}_{11}^{(2)} & \bar{\mathbf{Q}}_{12}^{(2)} & \\ \bar{\mathbf{Q}}^{(2)} & \bar{\mathbf{Q}}^{(2)} & \\ & & \end{bmatrix} \longrightarrow \begin{bmatrix} \bar{\mathbf{Q}}_{11}^{(3)} & \bar{\mathbf{Q}}_{12}^{(3)} & \bar{\mathbf{Q}}_{13}^{(3)} \\ \bar{\mathbf{Q}}_{21}^{(3)} & \bar{\mathbf{Q}}_{22}^{(3)} & \bar{\mathbf{Q}}_{23}^{(3)} \\ \bar{\mathbf{Q}}_{31}^{(3)} & \bar{\mathbf{Q}}_{32}^{(3)} & \bar{\mathbf{Q}}_{33}^{(3)} \end{bmatrix} \tag{3.76}$$

The benefit of this technique is that the largest inversion required is only an $n \times n$ matrix, and at each iteration, only one further inversion, corresponding to $(\bar{\mathbf{D}} - \bar{\mathbf{C}}\bar{\mathbf{A}}^{-1}\bar{\mathbf{B}})^{-1}$, will be required, as $\bar{\mathbf{A}}^{-1}$ is found in the preceding iteration. This method is particularly beneficial for the inversion that we will use for the scattering problems, as their diagional submatrices are identity matrices, and so their inversion are trivial. Additionally, this method is extremely useful for the inversion of very large matrices when only limited computer memory is available. The block submatrices may be stored to a physical drive, and called only as they are needed for an operation. Although there is a speed cost, it allows the solution of problems that otherwise would not be possible. A further advantage of the block matrix-approach to inversion, is that it may be used to iteratively invert the matrix, increasing the number of basis functions (and blocks), until a requisite level of accuracy has been achieved.

Table 3.2 shows the time taken to compute the matrix $\bar{\mathbf{Z}}$ from (3.55), using the different techniques. First, a regular inversion is performed using Gauss-Jordan elimination. This is compared to the Strassen algorithm, LU decomposition, and the Strassen algorithm with physical drive-storage. The comparisons are done for a number of different sphere sizes, and with a varying number of spheres. The Strassen algorithm and LU decomposition are significantly faster than the traditional technique, with the Strassen algorithm showing

significant benefit as the number of spheres increases, or the number of spherical harmonics are increased (or sphere sizes are larger). On the other hand, as we expect,the use of the physical drive significantly decreases the performance. However, only this technique is able to solve the larger problems. Therefore, it should be used only when absolutely necessary. Additionally, for comparison purposes, the storage technique was programmed so that each sphere interaction submatrix was called only when required, and operations where performed only with these matrices. It would be more efficient if full use was made of available memory, with larger matrices kept in memory and only sent to storage when required. This would be useful for the case when the scattering of a very large number of small spheres is to be calculated.

Table 3.2: Computational times for inversion of matrices for various aggregations of spheres

Size factor,	Harmonics,	Number of spheres,	Matrix size,	Computation time, s			
ka	N	N_s	$2N_sN(N+2)$	G-J	Strassen	LU	Storage
		10	160	0.17	0.09	0.08	4.84
0.01	2	20	320	0.72	0.41	0.36	39.1
		50	800	13.58	5.39	5.80	554
		2	140	0.14	0.11	0.08	0.49
0.5	5	10	700	9.39	2.23	3.78	67.8
		20	1400	74.7	17.4	34.3	560
		2	480	2.17	1.00	1.078	4.64
π	10	5	1200	43.6	10.9	20.8	106
		8	1920	N/A	N/A	N/A	452
		2	1020	31.1	15.7	15.3	26.8
2π	15	3	1530	127	49.2	56.6	124
		4	2040	N/A	N/A	N/A	326

3.4.4 Computational complexity

It is of interest to determine the computational complexity of the CBFM, as compared to multiple scattering. This is achieved by determining the order of the number of calculations required to solve a problem so, e.g., an $N \times N$ matrix requires $O(N^3)$ to invert, assuming Gauss-Jordan elimination is used.

Multiple scattering

For a system of N_s spheres, recall that the fields from each sphere will be represented by $N(N+2)$ spherical harmonics. There are two computationally intensive sets of calculations to perform: the first is the determination of all the special functions, and in particular the vector addition theorem coefficients. Direct calculation of all the special functions and addition theorem coefficients would be extremely inefficient. However, recurrence relations are presented in Appendix A and Appendix B that significantly decrease the computational cost. The second computationally intensive calculation is the matrix inversion in (3.41). For simplicity in comparing computational complexity, we will assume inversions are done using Gauss-Jordan elimination. So for the multiple scattering case, performing the required inversion will require $O(N_s^3 M^3)$ operations to solve the problem, where $M \equiv N(N+2)$.

CBFM

In the same manner as the multiple scattering solution, the vector addition theorem coefficients and the special functions can be solved for using recurrence relations. The inversion in this case, will require $O(N_s^3 P^3)$ operations, again assuming Gaussian elimination is used. This is where the computational complexity is decreased. The selection of the basis functions will at most keep the size of the problem the same, with $P \leq M$. In reality though, P will be smaller than M, and in many cases it will be significantly smaller. This can reduce the size of the problem by many times.

3.5 Summary

In this chapter a novel technique was presented for calculating the scattered fields from an aggregate of spheres. The characteristic basis function method is a highly efficient technique that allows the calculation of larger scattering problems than multiple scattering theory. It is capable of handling dielectric, magnetic, and conducting spheres, with sizes ranging from much less than a wavelength (Rayleigh regime) to multiple wavelengths in diameter. The physical idea behind the CBFM is that the waves incident upon any particular sphere in a system, can be decomposed into a number of weighted waves, or basis functions, that are incident from other spheres. Each of these waves can be treated individually, as a plane wave incident on an isolated sphere. The weightings of each of these waves are then determined, and this gives the solution to the scattering problem. It was also shown that in the case when the number of waves is equal to the total number of spherical harmonics, then the CBFM is equivalent to the multiple scattering formulation.

In addition, a number of numerical techniques were discussed for solving the linear system of equations. It was found that the Strassen algorithms for matrix inversion are well suited to this problem, and significantly reduce computational time. Additionally, the algorithm allows the iterative inversion of a matrix, while also allowing the solution of larger problems, by storing blocks of the matrix on a physical drive. With this technique, as long as round-off errors are kept to an acceptable level, then the size of the problem that can be solved is increased by many times.

Chapter 4

Effective Media Representation of Anisotropic Materials

With the increased interest in electromagnetic metamaterials over the past few years, a large amount of attention has been focused on the treatment of these metamaterials as homogeneous effective media [34, 36, 60, 152]. Techniques have been developed to extract the effective material properties of a slab composed of a metamaterial [63, 153, 154, 155]. These techniques are generally based on the inversion of the reflection and transmission parameters of a wave, normally incident on the slab, to give the effective refractive index n and impedance z. The effective permittivity ϵ and permeability μ are then calculated as $\epsilon = n/z$ and $\mu = nz$. These methods are all basically extensions of the more traditional techniques described in chapter 2 [61, 62, 94], but applied to structures with negative values of ϵ and/or μ. All these techniques have been limited to the characterization of homogeneous, isotropic media, and at normal incidence. The vast majority of attempts at measuring the refractive index or other material parameters at oblique incidence (see e.g. [152]), or accounting for anisotropy [156], have relied on fitting techniques. In [157], a reflection/transmission technique is presented that allows the extraction of bianisotropic material parameters for a slab with a normally incident wave. This method provides the main-diagonal tensor parameters for $\bar{\boldsymbol{\epsilon}}$ and $\bar{\boldsymbol{\mu}}$: ϵ_{xx}, ϵ_{yy}, ϵ_{zz}, μ_{xx}, μ_{yy}, and μ_{zz}, in addition to the bianisotropic term ξ_0. However, the technique is limited to normal incidence, and does not provide information on the off-diagonal tensor

terms. Additionally, six different incidences (the first three TE and TM) are required for extraction, significantly complicating the procedure.

In this chapter, a material characterization technique is presented that allows the retrieval of the twelve different $\bar{\boldsymbol{\epsilon}}$ and $\bar{\boldsymbol{\mu}}$ parameters, using transmission and reflection measurements at oblique incidence. The method requires the measurement of two different homogeneous slabs, of the same material but with different thicknesses. The method will first be verified with the analytically calculated reflection and transmission coefficients of an anisotropic slab, followed by simulations of the same slab. The technique will then be applied towards the parameter extraction of composite material, composed of lattices of spheres. In [63], it is shown that the extracted parameters of a single-layered wire medium will differ from the extracted parameters of the *bulk* medium, composed of a larger number of layers. It is evident from these results that there exists a lower bound of unit cell layers, such that the material can be treated as homogeneous bulk medium. It will be shown in this chapter that the eigenvectors of a slab's T-matrices, as the thickness is varied, may be compared to quantify whether or not the extracted material parameters for a particular slab thickness match up with those of the bulk material. In other words, it will be shown that, as the thickness of the slab is increased, the eigenvectors will eventually reach a point of saturation, at which they will no longer vary with increasing thickness (assuming the slab is not so thick that there are longitudinal resonances), and the extracted material parameters will thus be equivalent to those of the bulk material. This test is critical in confirming whether or not these effective media models may be used in the design of new devices utilizing these metamaterial structures.

4.1 Structure symmetry and its relation to the physical properties

Before we discuss the material property extraction techniques, a brief introduction will be provided on the forms of the material parameters that we can expect. In the study of crystal structures, the symmetry of a structure will determine the form of its material tensors. This

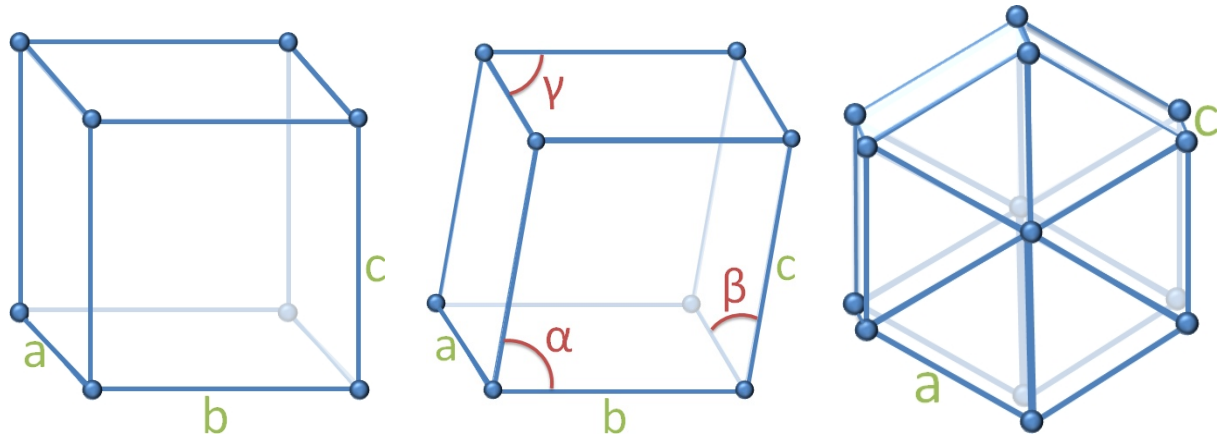

(a) Cubic, tetragonal, or orthorhombic system

(b) Triclinic, monoclinic, or rhombohedral (trigonal) system

(c) Hexagonal system

Figure 4.1: The seven lattice systems

is stated as *Neumann's Principle* [158]:

> *The symmetry elements of any physical property of a crystal must include the symmetry elements of the point group of the crystal.*

The point group of a crystal is the group of macroscopic symmetry elements that its structure possesses. What this means, is that all crystal structures can be divided into one of seven different lattice symmetry systems, and within each symmetry system, the material tensors will follow the same form. Figure 4.1 shows the structures of the different symmetry system unit cells, where interaxial angles α, β, and γ, and the unit cell lengths a, b, and c are used to differentiate between them. Table 4.1 summarizes the geometrical properties of these seven different systems, along with their optical classifications as isotropic, uniaxial, or biaxial. The form of a material property's tensor for each of the systems is given, where X can represent ϵ or μ. An isotropic material's permittivity tensor, for example, will be represented by a single ϵ coefficient, while a triclinic material will need up to six independent coefficients. The three uniaxial systems: tetragonal, hexagonal, and rhombohedral (trigonal), all have the same tensor form, and so we in fact only have a total of five different tensor forms.

Table 4.1: Lattice symmetry systems and the properties of their respective second-rank tensors

Optical classification	System	Lattice dimensions	Interaxial angles	Independent coefficients	Tensor in (x,y,z) coordinate system
Isotropic (anaxial)	Cubic	$a = b = c$	$\alpha = \beta = \gamma = 90°$	1	$\begin{bmatrix} X & & \\ & X & \\ & & X \end{bmatrix}$
Uniaxial	Tetragonal	$a = b \neq c$	$\alpha = \beta = \gamma = 90°$	2	$\begin{bmatrix} X_{xx} & & \\ & X_{xx} & \\ & & X_{zz} \end{bmatrix}$
	Hexagonal	$a = b \neq c$	$\alpha = \beta = 90°, \gamma = 120°$	2	
	Rhombohedral	$a = b = c$	$\alpha, \beta, \gamma \neq 90°$	2	
Biaxial	Orthorhombic	$a \neq b \neq c$	$\alpha = \beta = \gamma = 90°$	3	$\begin{bmatrix} X_{xx} & & \\ & X_{yy} & \\ & & X_{zz} \end{bmatrix}$
	Monoclinic	$a \neq b \neq c$	$\alpha \neq 90°, \beta = \gamma = 90°$	4	$\begin{bmatrix} X_{xx} & & X_{xz} \\ & X_{yy} & \\ X_{xz} & & X_{zz} \end{bmatrix}$
	Triclinic	$a \neq b \neq c$	$\alpha, \beta, \gamma \neq 90°$	6	$\begin{bmatrix} X_{xx} & X_{xy} & X_{xz} \\ X_{xy} & X_{yy} & X_{yz} \\ X_{xz} & X_{yz} & X_{zz} \end{bmatrix}$

4.2 Retrieval techniques from the literature

4.2.1 Homogeneous isotropic media [63, 153, 154, 155]

The majority of metamaterial characterization techniques developed to date are, as we stated previously, based on variations of the Nicholson-Ross-Weir [61, 62] method; developed initially for regular dielectrics. Inversion equations have been derived to retrieve an isotropic slab's refractive index n and impedance z:

$$z = \pm\sqrt{\frac{\left(1+S_{11}\right)^2 - S_{21}^2}{\left(1-S_{11}\right)^2 - S_{21}^2}}, \quad \mathrm{Re}(z) \geq 0 \tag{4.1}$$

$$\mathrm{Im}(n) = \pm\mathrm{Im}\left\{\frac{1}{k_0 d}\cos^{-1}\left(\frac{1}{2S_{21}}\left[1-(S_{11}^2 - S_{21}^2)\right]\right)\right\}, \quad \mathrm{Im}(n) \geq 0 \tag{4.2}$$

$$\mathrm{Re}(n) = \pm\mathrm{Re}\left\{\frac{1}{k_0 d}\cos^{-1}\left(\frac{1}{2S_{21}}\left[1-(S_{11}^2 - S_{21}^2)\right]\right)\right\} + \frac{2\pi m}{k_0 d}, \tag{4.3}$$

where $k_0 = \omega/c$ is the wavenumber of the incident field, and the S-parameters S_{11} and S_{21} are the reflection and transmission coefficients, respectively, for a slab of thickness d. The sign of the square root in (4.1) is determined such that $\mathrm{Re}(z) \geq 0$. Likewise, the sign in (4.2) is chosen such that $\mathrm{Im}(n) \geq 0$. The retrieval of the real part of n is, however, complicated by the branch cuts of the inverted function; we are left with an unknown branch index m that causes an ambiguity in the result. This is a problem that plagues all the extraction techniques that will be presented in this chapter. Many suggestions have been made on how to remove the uncertainty in the determination of the integer m, e.g., [155] however there is still much debate. A recently published technique that is showing promise, makes use of the Kramers-Kronig causality relationships [159], that mathematically relates the frequency

dispersive imaginary component of a complex function to its real part, and vice-versa. As we can unambiguously determine the $\mathrm{Im}(n)$, we can thus obtain an approximation for $\mathrm{Re}(n)$ over the relevant frequency band, which will give us a good idea of the correct value of m to select.

Assuming the branch index is known, a further limitation of this method is that it is restricted to the retrieval of the material parameters of an isotropic medium, and only at normal incidence.

4.2.2 Homogeneous bianisotropic media [157]

The anisotropic behavior of many metamaterials is evident due to their non-symmetrical structures, and this has long been recognized [60, 160]. A technique for extracting the material parameters of a bianisotropic metamaterial has been demonstrated [157], for structures with at least orthorhombic symmetry, where the tensor coefficients are zero off the main-diagonal. This system will have up to seven unknowns: ϵ_{xx}, ϵ_{yy}, ϵ_{zz}, μ_{xx}, μ_{yy}, and μ_{zz}, in addition to the bianisotropic term ξ_0. This technique also makes use of the reflection and transmission coefficients, however six different waves at normal incidence are used, as opposed to the single measurement of Smith's isotropic retrieval technique. Dispersive relations for each of these waves have been found, and they are solved for the seven unknown material parameters, in a manner similar to that of the isotropic case. These dispersive relations are summarized in Table 4.2.

Table 4.2: Dispersion relationship, impedance z, and refractive index n for each incident wave [157]

Case	Dispersion relationship	z	n
TE1	$k_z^2 = k_0^2 \epsilon_{yy} \mu_{xx}$	$\sqrt{\mu_{xx}/\epsilon_{yy}}$	$\sqrt{\epsilon_{yy}\mu_{xx}}$
TM1	$k_z^2 = k_0^2 \left(\epsilon_{xx}\mu_{yy} - \xi_0^2 \epsilon_{xx}/\epsilon_{zz}\right)$	$\frac{\epsilon_{xx}}{\sqrt{\epsilon_{xx}\mu_{yy} - \xi_0^2\epsilon_{xx}/\epsilon_{zz}}}$	$\sqrt{\epsilon_{xx}\mu_{yy} - \xi_0^2\epsilon_{xx}/\epsilon_{zz}}$
TE2	$k_x^2 = k_0^2 \left(\epsilon_{zz}\mu_{yy} - \xi_0^2\right)$	$\frac{\mu_{yy}}{\sqrt{\epsilon_{zz}\mu_{yy} - \xi_0^2 + j\xi_0^2}}$	$\sqrt{\epsilon_{zz}\mu_{yy} - \xi_0^2}$
TM2	$k_x^2 = k_0^2 \epsilon_{yy} \mu_{zz}$	$\sqrt{\epsilon_{yy}/\mu_{zz}}$	$\sqrt{\epsilon_{yy}\mu_{zz}}$
TE3	$k_y^2 = k_0^2 \epsilon_{xx} \mu_{zz}$	$\sqrt{\mu_{zz}/\epsilon_{xx}}$	$\sqrt{\epsilon_{xx}\mu_{zz}}$
TM3	$k_y^2 = k_0^2 \left(\epsilon_{zz}\mu_{xx} - \xi_0^2 \mu_{xx}/\mu_{yy}\right)$	$\frac{\epsilon_{zz}}{\sqrt{\epsilon_{zz}\mu_{xx} - \xi_0^2\mu_{xx}/\mu_{yy}}}$	$\sqrt{\epsilon_{zz}\mu_{xx} - \xi_0^2\mu_{xx}/\mu_{yy}}$

4.3 Homogeneous anisotropic media

4.3.1 Motivation for retrieval at oblique incidence angles

In practise, a wave may be incident on the metamaterial slab from an oblique angle. Furthermore, an incident wave may be non-planar (e.g., Gaussian [161]), in which case a spatial decomposition of the wave will reveal that it is a summation of a number of waves incident from different angles. Although in theory a homogeneous material will have angular independent material tensors, the homogeneity of the metamaterial structures that have been characterized has only been assumed. The material has been characterized only at normal incidence by a plane wave, and the assumption is made that the retrieved material parameters will be valid for any incident wave. For device design, however, it is extremely important to know whether these assumptions will in fact hold. There will be absolutely no benefit of modeling a metamaterial structure as an effective medium, if that effective medium model is only valid at normal incidence on a rectangular dielectric slab by a plane wave.

Furthermore, it would be of interest to be able to model complex metamaterial structures as effective materials with less than orthorhombic symmetry, i.e. there will be non-zero ten-

sor coefficients off the main axis. Referring back to Neumann's Principle, if the metamaterial structure has less than orthorhombic symmetry, then the material tensors may do as well. We will now describe a technique that can be used to extract the material parameters of a homogeneous anisotropic material with dielectric and magnetic components. The characterization can be performed at normal or oblique incidence, and requires the measurement of a TE and a TM wave. We will discuss the number of coefficients that can be extracted for different symmetries, as well as when we use an oblique, as opposed to a normal incident wave.

Additionally, it was mentioned that for very thin composite media, the extracted material parameters may not be equivalent to those of the bulk medium. In [63], an investigation is performed on a material with a unit cell composed of a single wire. The effective permittivity of the medium is extracted for thicknesses of one, three, and five unit cells. Traditionally, one would define the medium as *homogeneous* if the extracted parameters were equivalent for all three cases. However, in the investigation by Smith *et al.*, it is found that the effective permittivity of the single-layer medium deviates noticeably from the three- or five-layer bulk media, yet the bulk medium is still treated as homogeneous. This complication in the definition of a homogeneous medium arises due to the complex interactions between the different layers of a composite medium. For this case of a wire medium, a single wire layer will interact only with the incident wave, and we can call these interactions the *surface layer effects*. However, with multiple layers of wires, there will be mutual interactions between the different wire layers. With increasing numbers of wire layers, a saturation point will eventually be achieved, such that the interacting fields will average out to a bulk medium, with the surface layer effects having a minimal contribution. Once this saturation point has been reached, the material parameters will not subsequently vary with increasing slab thickness.

In Figure 4.2a, a medium is composed of wires with spacings large enough, such that there is minimal interaction between the wires. In this case, one would expect the extracted

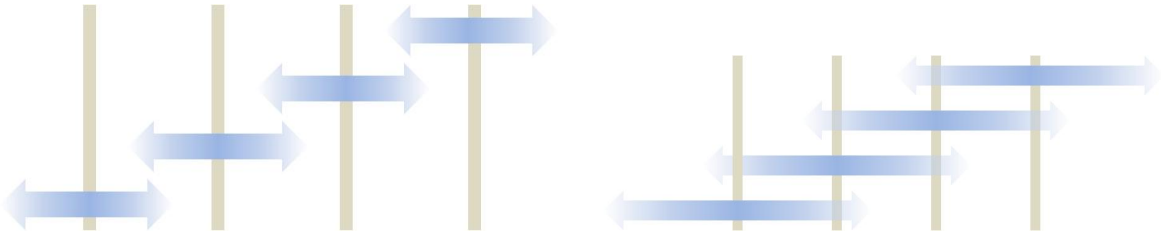

(a) Medium with minimal interaction between adjacent wires.

(b) Medium with significant interaction between adjacent wires.

Figure 4.2: Two different wire media, with arrows representing the strength of the field interactions with distance from a particular wire. The first medium has sufficient distance between wires such that there is minimal interaction. The second medium has closely spaced wires, and so there is significant interaction between adjacent wires. Note that the figures are not to scale; most important are the lengths of the arrows representing the field interactions.

parameters of just one or two layers of wires to represent that of the bulk material. In Figure 4.2b, the wires are closer to one another in this case, such that there is significant interaction between adjacent wires, as represented by the arrows. In this scenario, the fields between the middle two wire layers can be expected to be very similar to one another, and will form the bulk material. The outer two wire layers contribute the surface layer effects. Because of the strong interactions between the adjoining unit cells, one or two layers of wires will not sufficiently represent the material parameters of the bulk medium, and so at least three or four layers must be considered. As an analogy, consider a slab of material that we know to be homogeneous (e.g. the Alumina samples we characterized in chapter 2). Now assume that the surface of the slab is rough, and that the slab is very thin, such that the surface roughness is significant in comparison to the thickness of the slab. We can consider this surface roughness to be the surface layer effects, while the interior of the sample is the bulk material. If we were to characterize this material, then we would not have acceptable results, due to the strong surface layer effects. However, if we increased the thickness of the material, such that the surface roughness is negligible in comparison, then the surface layer effects will similarly be negligible in comparison to the bulk material, and our characterization will hence give acceptable results for the bulk material.

The techniques presented will first be verified by analytically calculating the reflection

and transmission coefficients of several known anisotropic materials, and then backing out the material parameters and comparing them to the correct (known) values. A similar task will be performed with the simulated reflection and transmission coefficients of the materials. Finally, the effective material parameters of conglomerates of spheres will be calculated. The spheres will be arranged with different lattice symmetries, so as to determine the lattice's effect on the tensor forms.

4.3.2 Scattering from an anisotropic slab.

The source-free, time-harmonic forms of Maxwell's equations relate the electric $\mathbf{E}$ and magnetic $\mathbf{H}$ fields to one another, at a frequency ω, in terms of the complex permittivity $\bar{\boldsymbol{\epsilon}}$ and permeability $\bar{\boldsymbol{\mu}}$ tensors:

$$-\nabla \times \mathbf{E} = j\omega\bar{\boldsymbol{\mu}} \cdot \mathbf{H} \tag{4.4a}$$

$$\nabla \times \mathbf{H} = j\omega\bar{\boldsymbol{\epsilon}} \cdot \mathbf{E}. \tag{4.4b}$$

Recall that the most general (and least symmetric) form of the second-rank material tensors are related to the triclinic point group, then using Table 4.1, we can define the permittivity and permeability tensors, in a rectangular coordinate system as,

$$\bar{\boldsymbol{\epsilon}} = \begin{bmatrix} \epsilon_{xx} & \epsilon_{xy} & \epsilon_{xz} \\ \epsilon_{xy} & \epsilon_{yy} & \epsilon_{yz} \\ \epsilon_{xz} & \epsilon_{yz} & \epsilon_{zz} \end{bmatrix} \quad and \quad \bar{\boldsymbol{\mu}} = \begin{bmatrix} \mu_{xx} & \mu_{xy} & \mu_{xz} \\ \mu_{xy} & \mu_{yy} & \mu_{yz} \\ \mu_{xz} & \mu_{yz} & \mu_{zz} \end{bmatrix}, \tag{4.5a}$$

respectively. Any of the coefficients can be complex, with an imaginary component representing either dielectric or magnetic losses, while a purely real tensor will represent a lossless system. Figure 4.3 shows the geometry under consideration.

A planar anisotropic slab of thickness d in the z-direction, and doubly-infinite in the

x- and y-directions, is incident upon by either a TE or a TM wave, at an angle θ_1 from the normal, and with a wavenumber k_0. In [162, 163], this geometry is analyzed in the traditional sense, in that the scattered and transmitted fields are calculated, knowing the material tensors. A *state-variable* approach is used, wherein a second-order wave equation is converted into two first-order ordinary differential equation, with a *state vector* describing the state of the system. Defining the state vector in terms of the transverse **E** and **H** field components:

$$\mathbf{\Psi} = \begin{bmatrix} E_x(z) \\ E_y(z) \\ H_x(z) \\ H_y(z) \end{bmatrix}, \tag{4.6}$$

it is possible to reduce the system from (4.4) and Figure 4.3, with both the TE and TM incident waves, into four coupled linear first-order differential equations [162]. In matrix notation, these are expressed as

$$\frac{d}{dz}\mathbf{\Psi}(z) = \bar{\mathbf{\Gamma}}(\boldsymbol{\epsilon}, \boldsymbol{\mu}, \theta_1, \omega) \cdot \mathbf{\Psi}(z), \tag{4.7}$$

where $\bar{\mathbf{\Gamma}}$ is a 4×4 complex matrix, that is a function of the material parameters, as well as θ_1 and ω. Additionally, as we are concerned only with linear media, we may define a 4×4 transition matrix $\bar{\mathbf{A}}$, that relates the state vectors at the two boundaries of the slab:

$$\mathbf{\Psi}(0) = \bar{\mathbf{A}} \cdot \mathbf{\Psi}(d). \tag{4.8}$$

The regular scattering problem is concerned with the determination of $\bar{\mathbf{A}}$, knowing $\bar{\mathbf{\Gamma}}$, and then solving for the complex scattering and transmission matrices, $\bar{\mathbf{S}}$ and $\bar{\mathbf{T}}$ respectively. It is shown in [162] that (4.7) may be expressed as the eigenvalue system

$$\left[\bar{\mathbf{\Gamma}} - \gamma_n \bar{\mathbf{I}}\right] \cdot \mathbf{V}_n = 0, \tag{4.9}$$

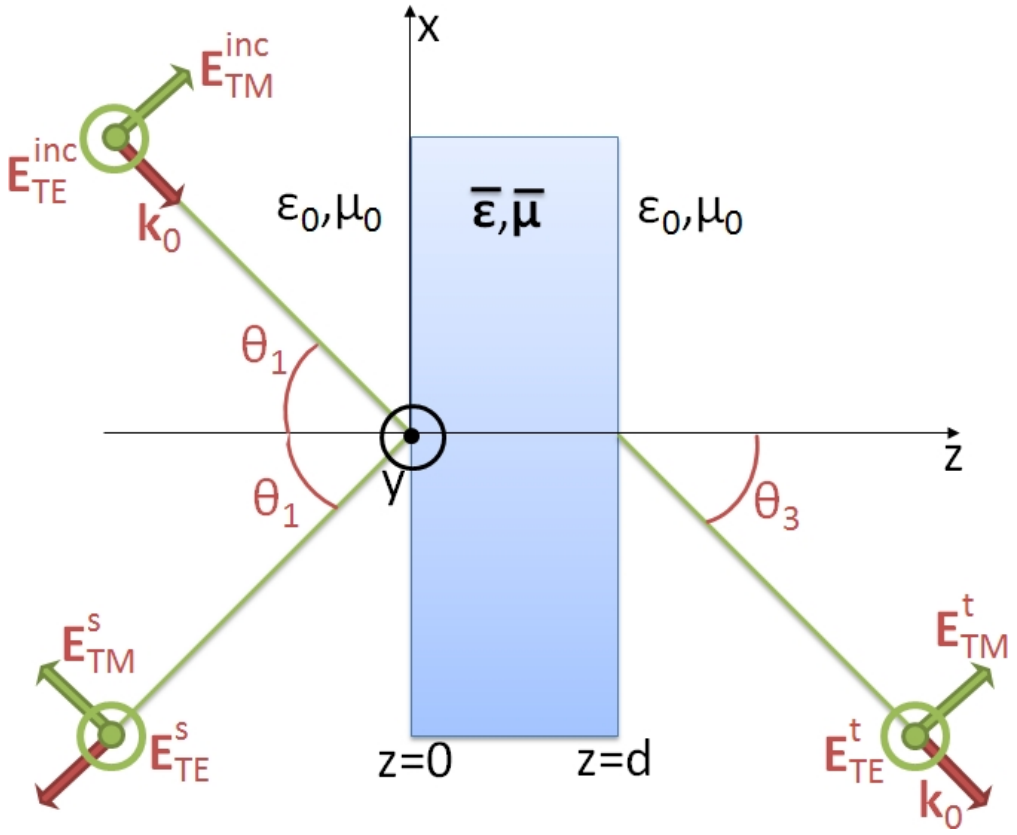

Figure 4.3: Scattering and transmission from an anisotropic doubly-infinite material.

where $\bar{\mathbf{I}}$ is the 4×4 identity matrix. The eigenvalue system will therefore give us four eigenvalues γ_n, and eigenvectors $\mathbf{V}_m$, such that $n = 1$ to 4. If we define a matrix $\bar{\mathbf{P}}$ whose diagonal elements are the eigenvalues γ,

$$\bar{\mathbf{P}} = \begin{bmatrix} \gamma_1 & & & \\ & \gamma_2 & & \\ & & \gamma_3 & \\ & & & \gamma_4 \end{bmatrix}, \tag{4.10}$$

and a matrix $\bar{\mathbf{V}} = [\mathbf{V}_1, \mathbf{V}_2, \mathbf{V}_3, \mathbf{V}_4]$, then we can solve for the eigendecomposition

$$\bar{\mathbf{A}} = \bar{\mathbf{V}} \cdot e^{-\bar{\mathbf{P}}d} \cdot \bar{\mathbf{V}}^{-1}, \tag{4.11}$$

where the exponentiation of a matrix is given as

$$e^{-\bar{\mathbf{P}}d} = \begin{bmatrix} e^{-\gamma_1 d} & & & \\ & e^{-\gamma_2 d} & & \\ & & e^{-\gamma_3 d} & \\ & & & e^{-\gamma_4 d} \end{bmatrix}. \tag{4.12}$$

This is the solution given in [162] for the transfer matrix. Our goal, however, is to begin with the S-parameters, and retrieve the material properties.

4.3.3 Material parameter retrieval

Extraction procedure

The procedure to extract the material parameters of an anisotropic slab, from the S-parameters, can be summarized as follows:

1. Obtain S-parameters for TE and TM incidence, and for two different slab thicknesses.
2. Solve for $\bar{\mathbf{A}}$.
3. Find eigenvectors and eigenvalues of $\bar{\mathbf{A}}$.
4. Solve for eigenvalues of $\bar{\mathbf{\Gamma}}$.
5. $\bar{\mathbf{\Gamma}} = \bar{\mathbf{V}} \cdot \bar{\mathbf{P}} \cdot \bar{\mathbf{V}}^{-1}$.
6. Retrieve $\bar{\boldsymbol{\epsilon}}$ and $\bar{\boldsymbol{\mu}}$.

Step 1 should be relatively straightforward, if the relevant experimental setup, or a numerical software tool is available. There are two important points to note: both TE and TM measurements are required, and the measurements must be performed on two slabs of the same composition, but with different thicknesses. For the first point, it is useful to note that of all the symmetries, only the triclinic point group will demonstrate cross-coupling

between the TE and the TM modes, i.e. the polarization of the incident wave can change. The reason for this is that, recalling Table 4.1, it is the only group that has non-zero off-axis parameters, outside the plane of propagation, i.e. non-zero tensor coefficients X_{xy} or X_{yz}. Monoclinic symmetry will show a non-zero X_{xz}, however this is in the plane of propagation of the incident wave, and thus will not affect its polarization. This is an interesting property, as it means that a change in polarization of the incident waves exists only if the structure symmetry is triclinic. One may ask, is the converse true? I.e., will triclinic symmetry always result in cross-polarization? The answer is no. It can be shown that all of the following three criteria must be satisfied such that no cross-polarization occurs:

$$\frac{\epsilon_{yz}}{\epsilon_{zz}} = \frac{\mu_{yz}}{\mu_{zz}}, \quad \epsilon_{xy} = \frac{\epsilon_{xz}\epsilon_{yz}}{\epsilon_{zz}}, \text{ and } \quad \mu_{xy} = \frac{\mu_{xz}\mu_{yz}}{\mu_{zz}}. \tag{4.13}$$

So while the most obvious solution to those cases is the trivial one, implying a non-triclinic structure, it is possible that a triclinic structure may not lead to cross-polarization of the incident waves. However, it should be noted that the conditions that will satisfy all three of those equations are extremely rare, and most likely do not exist in any material over a broad frequency range. So with a broadband measurement, we can say almost with certainty, that if no cross-polarization is exhibited, then the structure is not triclinic. As an example, if one's incident wave is TE, and a TM component is measured, then we can say that the structure definitely has triclinic symmetry, but if no TM component is measured, then we can safely ignore all X_{xy} or X_{yz} coefficients!

The reason for measuring two different slabs, is due to the number of equations required to solve for all the unknowns. Recall that $\bar{\mathbf{A}}$ is a 4×4 matrix, and so there are a total of 16 unknowns, for which we will need 16 linearly independent equations. On each slab, we will perform four sets of measurements (TE-TE, TM-TM, TE-TM and TM-TE), and each of these measurements will provide us with four S-parameters. However, due to the fact that we are measuring a linear, passive media, we will only actually have two unique

S-parameters, for a total of eight equations after all four measurements have been made. To obtain another eight, we must thus perform a second set of measurements on a different sample. We will however want to express the transition matrix for this second sample, in terms of the transition matrix $\bar{\mathbf{A}}$ of the first. Using (4.8) and (4.11), we can express the fields at the boundary $z = 0$ in terms of the fields at $z = pd$, where $p \geq 0$, such that

$$\mathbf{\Psi}(0) = \bar{\mathbf{V}} \cdot e^{-\bar{\mathbf{P}}pd} \cdot \bar{\mathbf{V}}^{-1} \cdot \mathbf{\Psi}(pd) = \bar{\mathbf{V}} \cdot \left[e^{-\bar{\mathbf{P}}d}\right]^{p} \cdot \bar{\mathbf{V}}^{-1} \cdot \mathbf{\Psi}(pd) = \bar{\mathbf{A}}^{p} \cdot \mathbf{\Psi}(pd). \tag{4.14}$$

So as long as the samples are homogeneous, we can express their transition matrices in terms of one another. To solve for $\bar{\mathbf{A}}$, we must first express it in terms of the S-parameters. Introducing the tangential field matrices,

$$\mathbf{E}_T(z) = \begin{bmatrix} E_x(z) \\ E_y(z) \end{bmatrix} \tag{4.15a}$$

$$\mathbf{H}_T(z) = \begin{bmatrix} H_x(z) \\ H_y(z) \end{bmatrix}, \tag{4.15b}$$

we can define the 2×2 complex scattering and transmission matrices, $\bar{\mathbf{S}}$ and $\bar{\mathbf{T}}$, as

$$\mathbf{E}_T^s(0) = \bar{\mathbf{S}} \cdot \mathbf{E}_T^{inc}(0) \tag{4.16a}$$

$$\mathbf{E}_T^t(d) = \bar{\mathbf{T}} \cdot \mathbf{E}_T^{inc}(0), \tag{4.16b}$$

where the superscripts inc, s, and t denote the incident, scattered, and total field, respectively. The $\bar{\mathbf{S}}$ matrix coefficients may be obtained from the relevant S_{11} measurements, while $\bar{\mathbf{T}}$ is composed of the corresponding S_{21} coefficients. For the purpose of clarifying the

definitions of the $\bar{\mathbf{S}}$ and $\bar{\mathbf{T}}$ matrices, we write them as

$$\bar{\mathbf{S}} = \begin{pmatrix} S_{xx} & S_{xy} \\ S_{yx} & S_{yy} \end{pmatrix} \quad \bar{\mathbf{T}} = \begin{pmatrix} T_{xx} & T_{xy} \\ T_{yx} & T_{yy} \end{pmatrix}, \tag{4.17}$$

so the S_{xy} component, for example, corresponds to the coefficient for the x component of the scattered field when a y-polarized electric field is incident, and so on.

Furthermore, for the case when the regions on both sides of the slab are the same, then $\theta_1 = \theta_3$, and

$$\mathbf{E}_T^{inc}(0) = \bar{\mathbf{Z}} \cdot \mathbf{H}_T^{inc}(0) \tag{4.18a}$$

$$\mathbf{E}_T^{s}(0) = -\bar{\mathbf{Z}} \cdot \mathbf{H}_T^{s}(0) \tag{4.18b}$$

$$\mathbf{E}_T^{t}(d) = \bar{\mathbf{Z}} \cdot \mathbf{H}_T^{t}(d), \tag{4.18c}$$

where we have introduced a wave impedance matrix to relate the electric and magnetic fields,

$$\bar{\mathbf{Z}} = \begin{bmatrix} 0 & \eta_m \cos\theta_m \\ -\eta_m \sec\theta_m & 0 \end{bmatrix}, \tag{4.19a}$$

for a characteristic impedance,

$$\eta_m = \sqrt{\frac{\mu_m}{\epsilon_m}}. \tag{4.19b}$$

The next step is to solve for the coefficients of the matrix $\bar{\mathbf{A}}$. If we partition $\bar{\mathbf{A}}$ into four 2×2 submatrices, such that

$$\bar{\mathbf{A}} = \begin{bmatrix} \bar{\mathbf{Q}}_{\mathbf{11}} & \bar{\mathbf{Q}}_{\mathbf{12}} \\ \bar{\mathbf{Q}}_{\mathbf{21}} & \bar{\mathbf{Q}}_{\mathbf{22}} \end{bmatrix}, \tag{4.20}$$

then along with (4.6), (4.16), and (4.18), we obtain the following matrix equation for a slab with thickness pd:

$$\begin{pmatrix} \bar{\mathbf{I}} \\ \bar{\mathbf{I}} \end{pmatrix} + \begin{pmatrix} \bar{\mathbf{S}}_{\mathbf{pd}} \\ -\bar{\mathbf{S}}_{\mathbf{pd}} \end{pmatrix} - \begin{pmatrix} \bar{\mathbf{I}} & 0 \\ 0 & \bar{\mathbf{Z}} \end{pmatrix} \cdot \begin{pmatrix} \bar{\mathbf{Q}}_{\mathbf{11}} & \bar{\mathbf{Q}}_{\mathbf{12}} \\ \bar{\mathbf{Q}}_{\mathbf{21}} & \bar{\mathbf{Q}}_{\mathbf{22}} \end{pmatrix}^{p} \cdot \begin{pmatrix} \bar{\mathbf{T}}_{\mathbf{pd}} \\ \bar{\mathbf{Z}}^{-1} \cdot \bar{\mathbf{T}}_{\mathbf{pd}} \end{pmatrix} = 0, \tag{4.21}$$

where the subscript pd refers to the measurements of the slabs with that thickness. The thinner of the two slabs may be set such that $p = 1$, and this allows us to rewrite the $\bar{\mathbf{A}}$ matrix in the preceding equations as:

$$\begin{pmatrix} \bar{\mathbf{Q}}_{\mathbf{11}} & \bar{\mathbf{Q}}_{\mathbf{12}} \\ \bar{\mathbf{Q}}_{\mathbf{21}} & \bar{\mathbf{Q}}_{\mathbf{22}} \end{pmatrix}^{p} = \left(\begin{array}{c|c} \bar{\mathbf{Q}}_{\mathbf{11}} & \left[\left(\bar{\mathbf{I}} + \bar{\mathbf{S}}_{\mathbf{d}}\right) \cdot \bar{\mathbf{T}}_{\mathbf{d}}^{-1} - \bar{\mathbf{Q}}_{\mathbf{11}}\right] \cdot \bar{\mathbf{Z}} \\ \bar{\mathbf{Q}}_{\mathbf{21}} & \left[\bar{\mathbf{Z}}^{-1}\left(\bar{\mathbf{I}} - \bar{\mathbf{S}}_{\mathbf{d}}\right) \cdot \bar{\mathbf{T}}_{\mathbf{d}}^{-1} - \bar{\mathbf{Q}}_{\mathbf{21}}\right] \cdot \bar{\mathbf{Z}} \end{array}\right)^{p}, \tag{4.22}$$

resulting in an easily solveable system, with an equivalent number of equations and unknowns. The difficulty, however, is that this is a nonlinear system, and for $p > 2$ there may be multiple solutions.

For the special case where $p = 2$ there will be a unique solution, and so the most appropriate setup is one in which the second slab is twice the thickness of the first. Making use of (4.21) and (4.22), we are able to solve for the $\bar{\mathbf{Q}}$ matrices, such that,

$$\bar{\mathbf{Q}}_{\mathbf{11}} = \frac{1}{2}\left[\left(\bar{\mathbf{I}} + \bar{\mathbf{S}}_{\mathbf{2d}}\right) \cdot \bar{\mathbf{T}}_{\mathbf{2d}}^{-1} \cdot \bar{\mathbf{T}}_{\mathbf{d}} - \left(\bar{\mathbf{I}} + \bar{\mathbf{S}}_{\mathbf{d}}\right) \cdot \bar{\mathbf{T}}_{\mathbf{d}}^{-1} \cdot \left(\bar{\mathbf{I}} - \bar{\mathbf{S}}_{\mathbf{d}}\right)\right] \cdot \bar{\mathbf{S}}_{\mathbf{d}}^{-1} \tag{4.23a}$$

$$\bar{\mathbf{Q}}_{\mathbf{12}} = \left[\left(\bar{\mathbf{I}} + \bar{\mathbf{S}}_{\mathbf{d}}\right) \cdot \bar{\mathbf{T}}_{\mathbf{d}}^{-1} - \bar{\mathbf{Q}}_{\mathbf{11}}\right] \cdot \bar{\mathbf{Z}} \tag{4.23b}$$

$$\bar{\mathbf{Q}}_{\mathbf{21}} = \frac{1}{2}\bar{\mathbf{Z}}^{-1} \cdot \left\{\left(\bar{\mathbf{I}} - \bar{\mathbf{S}}_{\mathbf{2d}}\right) \cdot \bar{\mathbf{T}}_{\mathbf{2d}}^{-1} - \left[\left(\bar{\mathbf{I}} - \bar{\mathbf{S}}_{\mathbf{d}}\right) \cdot \bar{\mathbf{T}}_{\mathbf{d}}^{-1}\right]^{2}\right\} \cdot \bar{\mathbf{T}}_{\mathbf{d}} \cdot \bar{\mathbf{S}}_{\mathbf{d}}^{-1} \tag{4.23c}$$

$$\bar{\mathbf{Q}}_{\mathbf{22}} = \left[\bar{\mathbf{Z}}^{-1}\left(\bar{\mathbf{I}} - \bar{\mathbf{S}}_{\mathbf{d}}\right) \cdot \bar{\mathbf{T}}_{\mathbf{d}}^{-1} - \bar{\mathbf{Q}}_{\mathbf{21}}\right] \cdot \bar{\mathbf{Z}}. \tag{4.23d}$$

Once $\bar{\mathbf{A}}$ has been determined, it is a simple matter to find its eigenvalues λ_m and eigenvectors, with a number of numerical routines available [147]. An eigendecomposition can the

be performed on $\bar{\mathbf{A}}$, and equating this to (4.11), we can solve for the four eigenvalues of $\bar{\mathbf{\Gamma}}$,

$$\gamma_n = \frac{1}{d} \ln \left[\lambda_n - 2j\pi m \right], \tag{4.24}$$

where m is the branch index that was discussed earlier. Recalling that $\bar{\mathbf{A}}$ and $\bar{\mathbf{\Gamma}}$ have the same set of eigenvectors $\mathbf{V}$, and using the definition of $\bar{\mathbf{P}}$ from (4.10), we can solve for

$$\bar{\mathbf{\Gamma}} = \bar{\mathbf{V}} \cdot \bar{\mathbf{P}} \cdot \bar{\mathbf{V}}^{-1}. \tag{4.25}$$

Now that we have obtained the $\bar{\mathbf{\Gamma}}$ matrix, the final step is to extract the material parameters. The material tensor coefficients can be found by solving the following equations:

$$\epsilon_{xx} = -\epsilon_{zz} \frac{\Gamma_{11}^2}{k_x^2} + j \frac{\Gamma_{41}}{\omega} \tag{4.26a}$$

$$\mu_{xx} = -\mu_{zz} \frac{\Gamma_{22}^2}{k_x^2} - j \frac{\Gamma_{23}}{\omega} \tag{4.26b}$$

$$\epsilon_{xz} = -j\epsilon_{zz} \frac{\Gamma_{11}}{k_x} \tag{4.26c}$$

$$\mu_{xz} = -j\mu_{zz} \frac{\Gamma_{22}}{k_x} \tag{4.26d}$$

$$\epsilon_{xy} = -j \left(\epsilon_{yz} \frac{\Gamma_{11}}{k_x} + \frac{\Gamma_{31}}{\omega} \right) \tag{4.26e}$$

$$\mu_{xy} = -j \left(\mu_{yz} \frac{\Gamma_{22}}{k_x} + \frac{\Gamma_{24}}{\omega} \right) \tag{4.26f}$$

$$\epsilon_{yy} = \frac{\epsilon_{yz}^2}{\epsilon_{zz}} + \frac{1}{\omega} \left(\frac{k_x^2}{\omega} \frac{1}{\mu_{zz}} - j\Gamma_{32} \right) \tag{4.26g}$$

$$\mu_{yy} = \frac{\mu_{yz}^2}{\mu_{zz}} + \frac{1}{\omega} \left(\frac{k_x^2}{\omega} \frac{1}{\epsilon_{zz}} + j\Gamma_{14} \right) \tag{4.26h}$$

$$\frac{\mu_{yz}}{\mu_{zz}} = \frac{\epsilon_{yz}}{\epsilon_{zz}} + j \frac{\Gamma_{12}}{k_x}. \tag{4.26i}$$

However, examination of the coefficients will lead to the conclusion that there will not always be sufficient equations to solve for all the unknowns. Hence, for certain symmetries, some of the parameters should be known *a priori*, or another set of measurements will be required. For non-magnetic materials, however, the relevant number of coefficients will be known and the full permittivity tensor can be determined with a single measurement. Table 4.3 lists the number of parameters needed for the full solution of both material parameters, under the different symmetry conditions. So a cubic (isotropic), or a uniaxial material may be fully determined just from measurements, but for triclinic symmetry, at least three parameters must be known beforehand. Also listed, are the determined parameters, that may be retrieved from $\bar{\mathbf{\Gamma}}$ without any knowledge of other material parameters. The final column shows the different groups of parameters that may be used to solve for the coefficients, in the case that parameters are known *a priori*. Only one coefficient may be selected from each group, so for example, with triclinic symmetry, μ_{yz}, μ_{yy}, and μ_{zz} may be used to fully determine the tensors, however μ_{yz}, μ_{xx}, and μ_{zz} may not be, as μ_{xx} and μ_{zz} are in the same group.

Another set of measurements will negate the need for *a priori* knowledge of any of the coefficients, as a second set of equations will allow the full solution of the coefficients. There are three modifications to the system that we can make to achieve a second measurement: we can change the angle of incidence; rotate the sample; or change the plane of the incident wave. The last two cases are identical mathematically, however sample rotation is easier experimentally, and so we will discuss this case along with the incident angle variation. The suitability of each of these two techniques will be determined for application to different symmetries.

Table 4.3: Parameters required for determination of second-rank material tensor with different lattice symmetries

System	Number of Parameters needed *a priori*	Determined parameters	Parameter groups (Select at most one from each group)
Cubic	0	ϵ, μ	-
Uniaxial	0	$\epsilon_{xx}, \epsilon_{zz}, \mu_{xx}, \mu_{zz}$	-
Orthorhombic	2	ϵ_{xx}, μ_{xx}	$(\epsilon_{yy}, \mu_{zz}), (\epsilon_{zz}, \mu_{yy})$
Monoclinic	2	-	$(\epsilon_{xx}, \epsilon_{xz}, \epsilon_{zz}, \mu_{yy})$, $(\mu_{xx}, \mu_{xz}, \mu_{zz}, \epsilon_{yy})$
Triclinic	3	-	$(\epsilon_{xx}, \epsilon_{xz}, \epsilon_{zz}), (\mu_{xx}, \mu_{xz}, \mu_{zz})$, $(\epsilon_{xy}, \epsilon_{yz}), (\mu_{xy}, \mu_{yz}), (\epsilon_{yy}), (\mu_{yy})$

Angle of incidence variation

Subsequent to the measurement of the sample at an angle θ_1, a second measurement is performed at an angle θ_2. For the isotropic or uniaxial cases, this second angular measurement is, of course, unnecessary. It can, however, be beneficial in other cases. For the biaxial cases, (4.26h) and (4.26g) can be rearranged to obtain expressions for ϵ_{zz} and μ_{zz}:

$$\epsilon_{zz} = \frac{j}{\omega} \frac{k_{x(1)}^2 - k_{x(2)}^2}{\Gamma_{14}^{(1)} - \Gamma_{14}^{(2)}} \tag{4.27a}$$

$$\mu_{zz} = \frac{j}{\omega} \frac{k_{x(1)}^2 - k_{x(2)}^2}{\Gamma_{32}^{(2)} - \Gamma_{32}^{(1)}}, \tag{4.27b}$$

where the bracketed number refers to one of the two angular measurements. However, Γ_{11} is a linear function of k_x, and so (4.26e) and (4.26f) cannot be used to determine the xy and yz components of ϵ and μ. So with these two equations, we will have the two required parameters needed to solve for all the orthorhombic and monoclinic coefficients in Table 4.3. However, this method cannot be used for magnetic materials with triclinic symmetry.

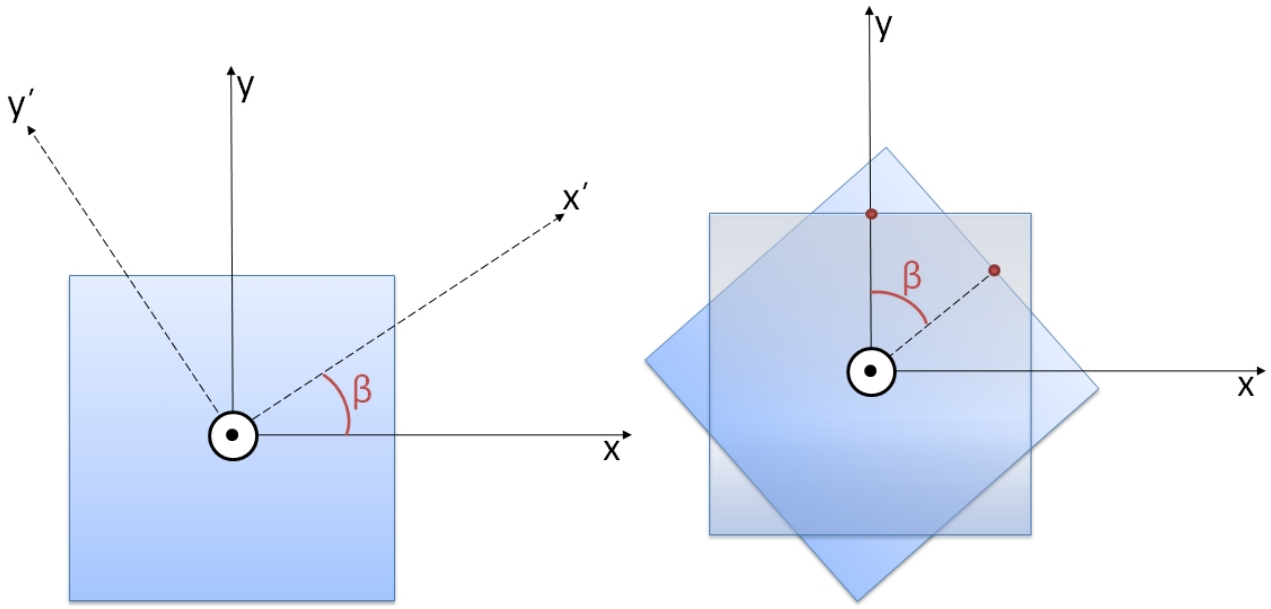

(a) Coordinate system rotation (b) Sample rotation

Figure 4.4: Rotation by an angle β.

Sample rotation

A rotation of the sample is equivalent to a rotation of the coordinate system, and a rotation in the coordinate system will lead to changes in the properties of the material tensors. In Figure 4.4a, the coordinate system axes are rotated around the z-axis, by an angle β. An identical rotation is shown in Figure 4.4b. It should be noted though, that the direction of the rotation will affect the material tensors, and so a clockwise rotation of the sample should be seen as a counterclockwise rotation of the coordinate axes.

A rotation matrix may be defined [158, 163] as,

$$\bar{\mathbf{T}} = \begin{pmatrix} \cos\theta & \sin\theta & 0 \\ -\sin\theta & \cos\theta & 0 \\ 0 & 0 & 1 \end{pmatrix}. \tag{4.28a}$$

A second-order tensor, $\bar{\mathbf{X}}$, can then be described, after rotation of the coordinate system, as

$\bar{\mathbf{X}}'$, where,

$$\bar{\mathbf{X}}' = \bar{\mathbf{T}} \cdot \bar{\mathbf{X}} \cdot \bar{\mathbf{T}}^T. \tag{4.28b}$$

Of most use to us is the case where $\beta = 90\,\text{deg}$, i.e., the sample is rotated by 90 deg *clockwise*. In this case, the rotated material tensors will be,

$$\bar{\boldsymbol{\epsilon}}' = \begin{bmatrix} \epsilon_{yy} & -\epsilon_{yx} & \epsilon_{yz} \\ -\epsilon_{xy} & \epsilon_{xx} & -\epsilon_{xz} \\ \epsilon_{zy} & -\epsilon_{zx} & \epsilon_{zz} \end{bmatrix} \quad \text{and} \quad \bar{\boldsymbol{\mu}}' = \begin{bmatrix} \mu_{yy} & -\mu_{yx} & \mu_{yz} \\ -\mu_{xy} & \mu_{xx} & -\mu_{xz} \\ \mu_{zy} & -\mu_{zx} & \mu_{zz} \end{bmatrix}. \tag{4.29}$$

Substituting these coefficients, in place of the unrotated coefficients, into (4.26) will provide enough equations to solve for all material parameters, and for all symmetry classes, including triclinic. The following three equations are most convenient:

$$\mu_{zz} = -j\frac{k_x^2}{\omega} \cdot \frac{1}{\Gamma_{41} + \Gamma'_{32}} \tag{4.30a}$$

$$\epsilon_{zz} = j\frac{k_x^2}{\omega} \cdot \frac{1}{\Gamma_{23} + \Gamma'_{14}} \tag{4.30b}$$

$$\epsilon_{yz} = -j\epsilon_{zz}\frac{\Gamma'_{11}}{k_x}. \tag{4.30c}$$

4.4 Results

4.4.1 Verification of parameter retrieval technique

The technique will first be verified on a number of slabs with known material parameters. The S-parameters will be calculated analytically, as well as simulated for the uniaxial and orthorhombic cases. Frequency domain simulations are performed using CST Microwave Studio [164], using the *Unit Cell* boundary conditions. The simulations, however, do not allow off-axis material parameters, and so triclinic materials will not be simulated. Once S-parameters are obtained, they will then be used to retrieve the material's permittivity and

permeability.

Uniaxial case

This is a relatively simple structure, yet it is very common in nature. From Table 4.3, it is evident that a single set of measurements, at one incident angle, will provide all material parameters. A lossless uniaxial material with,

$$\bar{\boldsymbol{\epsilon}} = \epsilon_0 \begin{bmatrix} 5-0.5j & 0 & 0 \\ 0 & 5-0.5j & 0 \\ 0 & 0 & 1-0.1j \end{bmatrix} \quad \text{and} \quad \bar{\boldsymbol{\mu}} = \mu_0 \begin{bmatrix} 2-0.2j & 0 & 0 \\ 0 & 2-0.2j & 0 \\ 0 & 0 & 1-0.1j \end{bmatrix}$$

at 10 GHz has been simulated and calculated, for sample thicknesses of $1mm$ and $2mm$. The non-zero parameters of the $\bar{\mathbf{S}}$ and $\bar{\mathbf{T}}$ matrices, as defined in (4.16), are plotted in Figure 4.5. Recall that for the uniaxial case, there is no cross-polarization of the incident waves, and so the xy and yx components are zero. The simulations matched our expectations, and so those components have not been plotted.

Following the procedure in subsection 4.3.3, the $\bar{\mathbf{\Gamma}}$ matrices are found at each frequency point. For the purpose of demonstrating this procedure, we will present the numerical results for the first frequency point (8 GHz) in Figure 4.5. Recalling that our two samples have thickness of $1mm$ and $2mm$ respectively, the simulated $\bar{\mathbf{S}}$ and $\bar{\mathbf{T}}$ matrices at this frequency are found to be

$$\bar{\mathbf{S}}_{(1mm)} = \begin{pmatrix} -0.053-0.102j & 0 \\ 0 & -0.24-0.269j \end{pmatrix}$$

$$\bar{\mathbf{T}}_{(1mm)} = \begin{pmatrix} 0.832-0.428j & 0 \\ 0 & 0.709-0.496j \end{pmatrix}$$

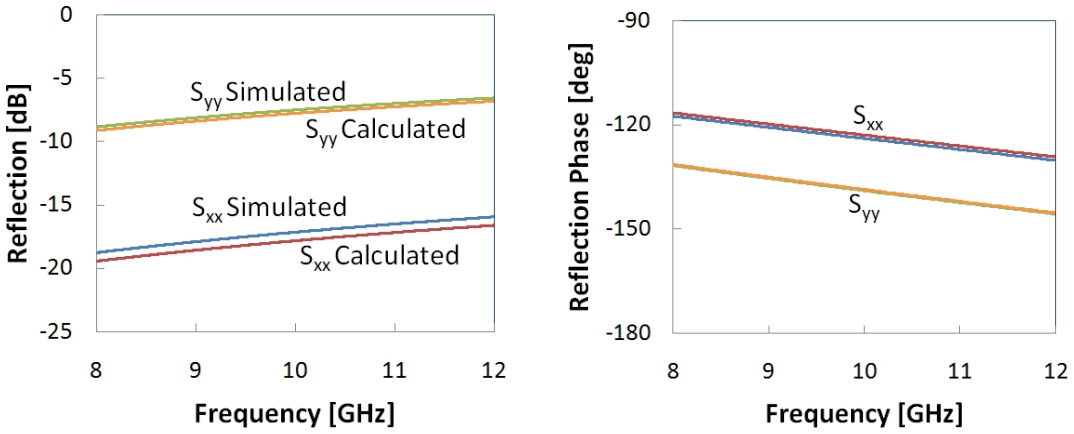

(a) Reflection magnitude.

(b) Reflection phase.

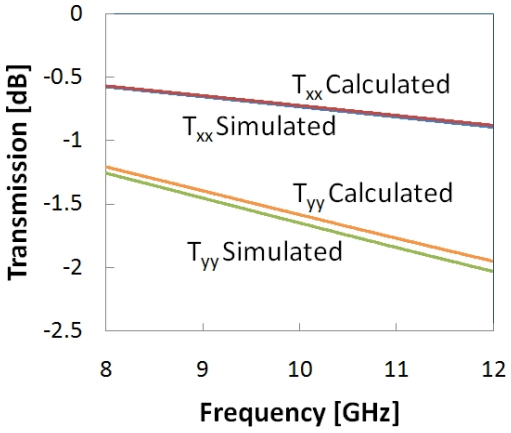

(c) Transmission magnitude.

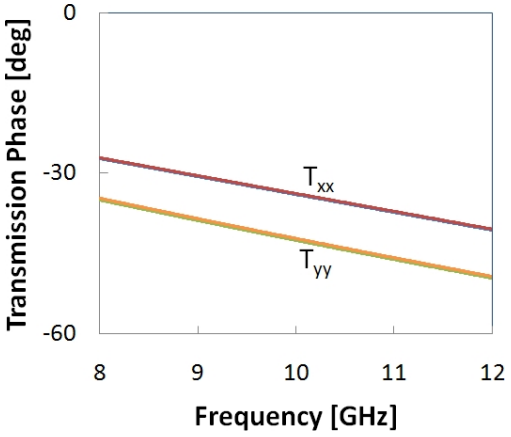

(d) Transmission phase.

Figure 4.5: Calculated and simulated S and T parameters for a uniaxial material. Cross-coupling terms, i.e., S_{xy}, S_{yx}, T_{xy} and T_{yx} are zero, and are not shown.

$$\bar{\mathbf{S}}_{(2mm)} = \begin{pmatrix} -0.154 - 0.118j & 0 \\ 0 & -0.498 - 0.203j \end{pmatrix}$$
$$\bar{\mathbf{T}}_{(2mm)} = \begin{pmatrix} 0.511 - 0.703j & 0 \\ 0 & 0.334 - 0.65j \end{pmatrix}. \tag{4.31}$$

To find the $\bar{\mathbf{Q}}$ matrices at this frequency, we solve the equations given in (4.23) to get,

$$\bar{\mathbf{Q}}_{\mathbf{11}} = \begin{pmatrix} 0.899 + 0.023j & 0 \\ 0 & 0.878 + 0.025j \end{pmatrix}$$
$$\bar{\mathbf{Q}}_{\mathbf{12}} = \begin{pmatrix} 0 & 13.523 + 91.426j \\ -10.414 - 118.847j & 0 \end{pmatrix}$$
$$\bar{\mathbf{Q}}_{\mathbf{21}} = \begin{pmatrix} 0 & -2.098 \times 10^{-4} - 1.967j \times 10^{-3} \\ 1.587 \times 10^{-4} + 2.181j \times 10^{-3} & 0 \end{pmatrix}$$
$$\bar{\mathbf{Q}}_{\mathbf{22}} = \begin{pmatrix} 0.884 + 0.029j & 0 \\ 0 & 0.908 + 0.031j \end{pmatrix}. \tag{4.32}$$

Recall that, by definition, the $\bar{\mathbf{A}}$ matrix is composed of all the $\bar{\mathbf{Q}}$ matrices, as shown in (4.20). We have thus completed step 2 in the extraction procedure. Step 3 is to determine the eigenvalues and eigenvectors of the $\bar{\mathbf{A}}$ matrix. Following the formulation in subsection 4.3.2, the matrices of eigenvalues and eigenvectors are

$$e^{-\bar{\mathbf{P}}d} = \text{diag} \begin{pmatrix} 0.854 - 0.42j \\ 0.953 + 0.474j \\ 0.834 - 0.456j \\ 0.928 + 0.511j \end{pmatrix} \quad \text{and} \quad \bar{\mathbf{V}} = \begin{pmatrix} 1 & 1 & 0 & 0 \\ 0 & 0 & 1 & 1 \\ 0 & 0 & V_{33} & V_{34} \\ V_{41} & V_{42} & 0 & 0 \end{pmatrix}, \tag{4.33}$$

where $V_{33} = 4.055 \times 10^{-3} - 1.668j \times 10^{-5}$, $V_{34} = -4.089 \times 10^{-3} + 6.03j \times 10^{-5}$, $V_{41} = -4.807 \times 10^{-3} - 2.247j \times 10^{-4}$, and $V_{42} = 4.915 \times 10^{-3} + 1.352j \times 10^{-4}$. The next step is to

determine the eigenvalues of $\bar{\mathbf{\Gamma}}$. They are found, using (4.24), to be

$$\bar{\mathbf{P}} = \text{diag} \begin{pmatrix} 49.486 + 456.732j \\ -62.149 - 461.655j \\ 50.638 + 500.705j \\ -57.506 - 503.209j \end{pmatrix} \frac{1}{m}. \tag{4.34}$$

The branch index was selected as $m = 0$. An advantage of a thin material, is that a change in the branch index will have a significant effect on the retrieved material parameters. An intuition of the expected parameters will thus give a very good idea of what the branch index should be. The eigenvectors will, of course, be the same as the eigenvectors of $\bar{\mathbf{A}}$. Thus, we can solve for $\bar{\mathbf{\Gamma}}$ as

$$\bar{\mathbf{\Gamma}} = \begin{pmatrix} \Gamma_{11} & 0 & 0 & \Gamma_{14} \\ 0 & \Gamma_{22} & \Gamma_{23} & 0 \\ 0 & \Gamma_{32} & \Gamma_{33} & 0 \\ \Gamma_{41} & 0 & 0 & \Gamma_{44} \end{pmatrix}, \tag{4.35}$$

where $\Gamma_{11} = -1.32 + 1.937j$, $\Gamma_{14} = -1.496 \times 10^4 - 9.391j \times 10^4$, $\Gamma_{22} = -0.537 + 0.585j$, $\Gamma_{23} = 1.211 \times 10^4 + 1.234j \times 10^5$, $\Gamma_{32} = 0.239 + 2.042j$, $\Gamma_{33} = -6.331 - 3.089j$, $\Gamma_{41} = -0.188 - 2.242j$, and $\Gamma_{44} = -11.343 - 6.86j$. In actual fact, there should only be non-zero terms along the minor diagonal, however errors in the simulations have resulted in some small non-zero terms on the main diagonal. It is evident that these are non-physical, as for a symmetric tensor with $\epsilon_{xz} = \epsilon_{zx}$ and $\mu_{xz} = \mu_{zx}$, then we should have $\Gamma_{11} = \Gamma_{44}$ and $\Gamma_{22} = \Gamma_{33}$.

Nevertheless, we are now able to calculate the material parameters using (4.26a), (4.26b), (4.26g), and (4.26h). The extracted material parameters over the whole frequency range are plotted in Figure 4.6. The plot includes materials extracted from simulation, and also from analytically calculated S parameters. They show good agreement. Errors from the parameters extracted from simulation are due to the errors in the S parameters, as seen in

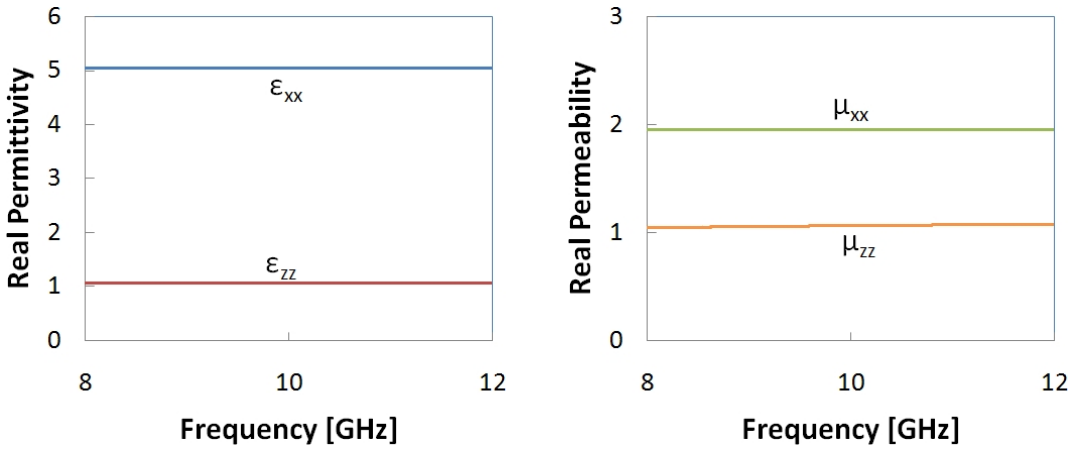

(a) Re(ϵ).

(b) Re(μ).

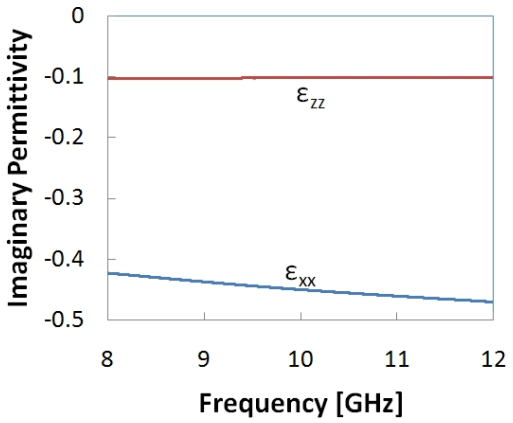

(c) Im(ϵ).

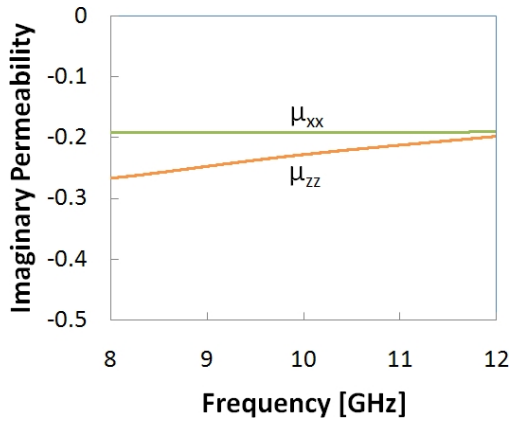

(d) Im(μ).

Figure 4.6: Extracted material parameters for a material with uniaxial symmetry. Parameters are extracted from simulations, and also from calculated S parameters.

Figure 4.5. There is also a possibility that the dispersion model in the simulation, due to the losses included, result in material parameters that may diverge slightly from what we expect.

Orthorhombic case

A more complicated material is used for verification in this case. The magnetic material demonstrates orthorhombic symmetry, and to complicate matters, it is lossy, and the

anisotropic permittivity functions are dispersive. The material tensors are given as

$$\bar{\boldsymbol{\epsilon}}(\omega) = \begin{bmatrix} \epsilon_{xx}(\omega) & 0 & 0 \\ 0 & \epsilon_{yy}(\omega) & 0 \\ 0 & 0 & \epsilon_{zz}(\omega) \end{bmatrix} \quad \text{and} \quad \bar{\boldsymbol{\mu}} = \mu_0 \begin{bmatrix} 4 - 0.4j & 0 & 0 \\ 0 & 2 - 0.2j & 0 \\ 0 & 0 & 1 - 0.1j \end{bmatrix}$$

Each of the permittivity functions follows a Lorentz dispersion model, defined as:

$$\epsilon(\omega) = \epsilon_0 \left(\epsilon_\infty + \frac{(\epsilon_s - \epsilon_\infty)\omega_0^2}{\omega_0^2 + j\omega\delta - \omega^2} \right), \tag{4.36}$$

where ϵ_s is the static permittivity, ϵ_∞ is the permittivity at infinity, ω_0 is the resonant frequency, and δ is the damping factor. The coefficients for each parameter are,

$$\begin{aligned} \epsilon_{xx}(\omega) &: \epsilon_s = 5; \quad \epsilon_\infty = 2; \quad \omega_0 = 70 \times 10^9 \text{rad/s}; \quad \delta = 25\text{rad/s} \\ \epsilon_{yy}(\omega) &: \epsilon_s = 1000; \quad \epsilon_\infty = 1; \quad \omega_0 = 200\pi \times 10^6 \text{rad/s}; \quad \delta = 1\text{rad/s} \\ \epsilon_{zz}(\omega) &: \epsilon_s = 5; \quad \epsilon_\infty = 4; \quad \omega_0 = 20\pi \times 10^9 \text{rad/s}; \quad \delta = 10\text{rad/s}. \end{aligned} \tag{4.37}$$

Referring to Table 4.3, it is evident that a second measurement is required in order to extract all parameters. Although sample rotation may be used, the method of incident angle variation shall be used for demonstration purposes. Two different angular measurements are made, at 45 deg and 60 deg off-normal. The procedure is almost exactly the same as for the uniaxial case, however as we have measured the two incident angles, we may first extract ϵ_{zz} and μ_{zz} using (4.27). The relevant equations from (4.26) may then be used to solve for the rest of the parameters.

The extracted parameters are shown in Figure 4.7. Again, the retrieved parameters show good agreement with what we would expect. In general, the errors in the imaginary parts of the coefficients are larger than those of the real, in common with the techniques presented in chapter 2. Although there are visible errors in some of the extracted results, as compared

to the calculated parameters, the technique still shows a good deal of accuracy, and it is envisioned that with more accurate simulations, an even closer match can be attained.

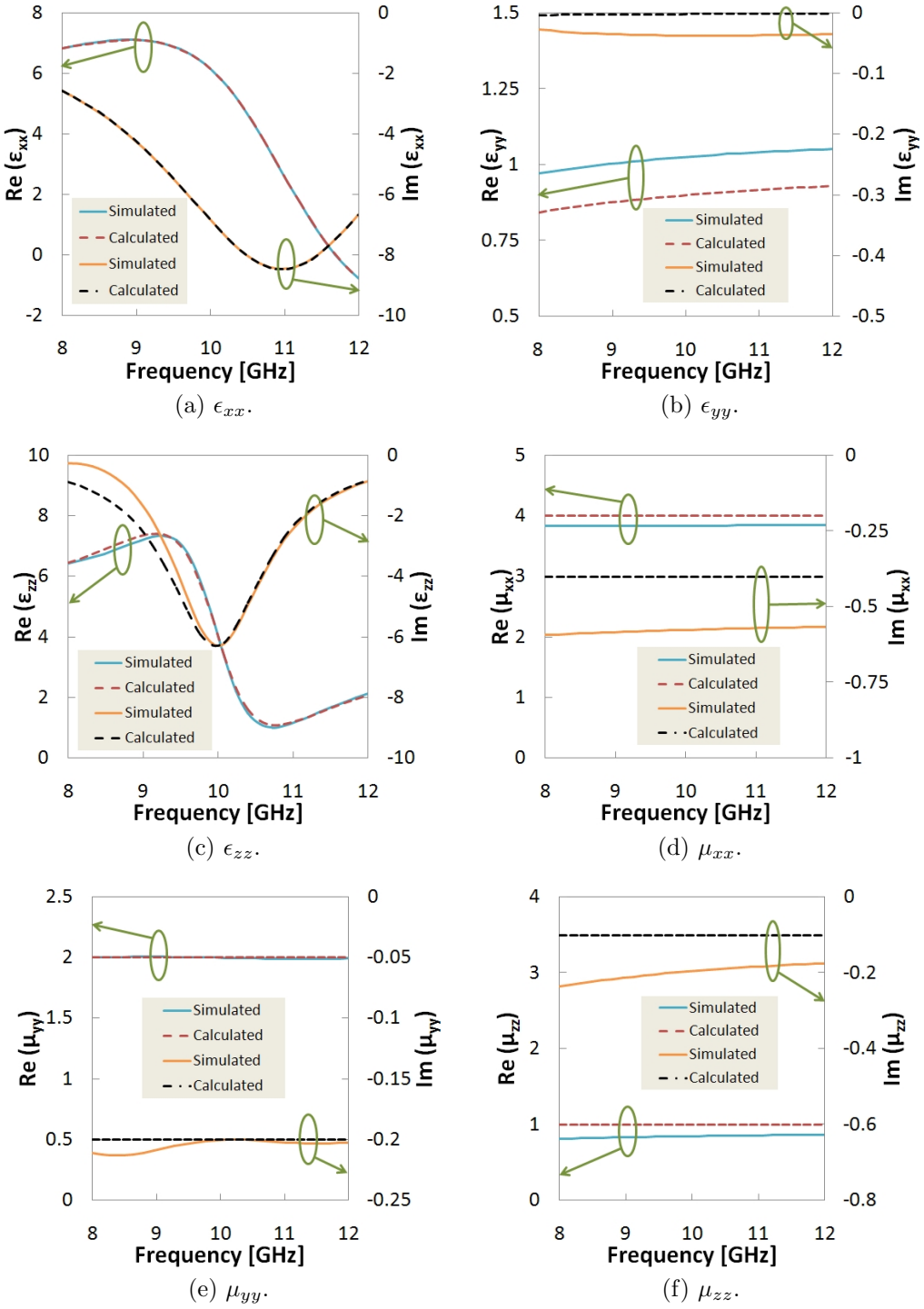

(a) ϵ_{xx}. (b) ϵ_{yy}.

(c) ϵ_{zz}. (d) μ_{xx}.

(e) μ_{yy}. (f) μ_{zz}.

Figure 4.7: Extracted material parameters for a material with orthorhombic symmetry. Parameters are extracted from simulations, and also from calculated S parameters.

Triclinic case

In this, the most general case, all material parameters are unknown. The sample rotation technique is required to solve the entire system, as the incident angle variation technique, demonstrated for the orthorhombic case, will not provide sufficient equations to solve for all unknowns. For this most general of cases, simulation tools available are not capable of modeling the complicated material parameters that we wish to retrieve. Nevertheless, verification can be performed by first calculating the required S parameters, and then using only those S parameters, assuming no *a priori* knowledge of the material, to retrieve the material's properties.

The S parameters are calculated for a slab with the following material parameters:

$$\bar{\boldsymbol{\epsilon}}(\omega) = \epsilon_0 \begin{bmatrix} 5 & -0.5 & 1 \\ -0.5 & 4 & 0.5 \\ 1 & 0.5 & 3 \end{bmatrix} \quad \text{and} \quad \bar{\boldsymbol{\mu}} = \mu_0 \begin{bmatrix} 5 & 0.5 & 0.5 \\ 0.5 & 3 & 2 \\ 0.5 & 2 & 2 \end{bmatrix}.$$

The material tensor of the rotated sample must also be found. Upon rotation by 90 deg clockwise, the slab will exhibit the following material parameters:

$$\bar{\boldsymbol{\epsilon}}(\omega) = \epsilon_0 \begin{bmatrix} 4 & 0.5 & 0.5 \\ 0.5 & 5 & 1 \\ 0.5 & 1 & 3 \end{bmatrix} \quad \text{and} \quad \bar{\boldsymbol{\mu}} = \mu_0 \begin{bmatrix} 3 & -0.5 & 2 \\ -0.5 & 5 & -0.5 \\ 2 & -0.5 & 2 \end{bmatrix},$$

The analytically calculated $\bar{\mathbf{S}}$ and $\bar{\mathbf{T}}$ matrices are plotted in Figure 4.8. It should be noted that in this case, the xy and yx coefficients are non-zero. This is as we expected, with the incident wave exhibiting cross-polarization. This cross-polarization is evident only with a triclinic material tensor. We can thus conclude that a structure that exhibits cross-polarization of an incident wave must be represented by a triclinic material tensor.

We will now attempt to retrieve the material tensors, using only the S parameters that we

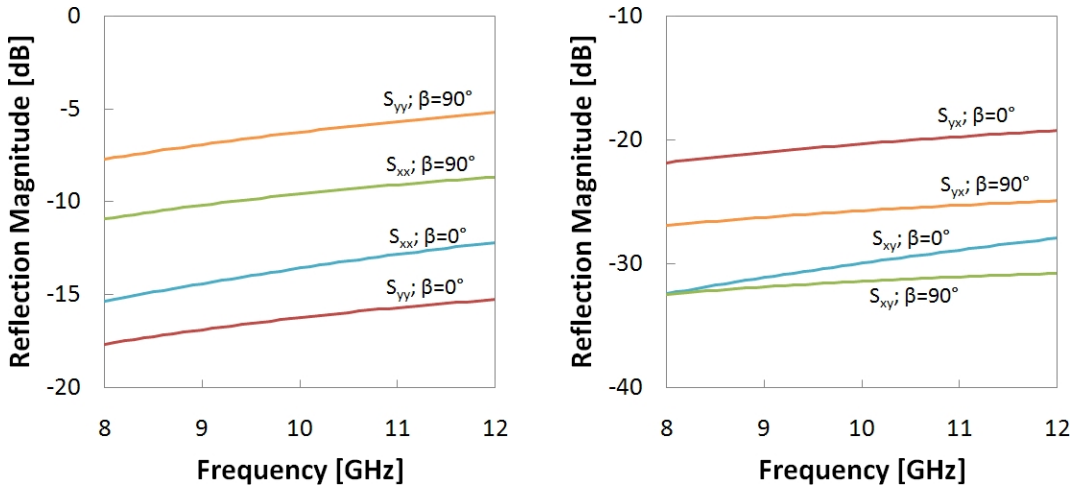

(a) S_{xx} and S_{yy}.

(b) S_{xy} and S_{yx}.

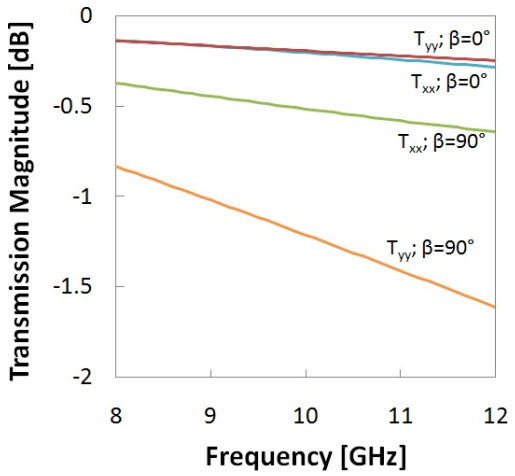

(c) T_{xx} and T_{yy}.

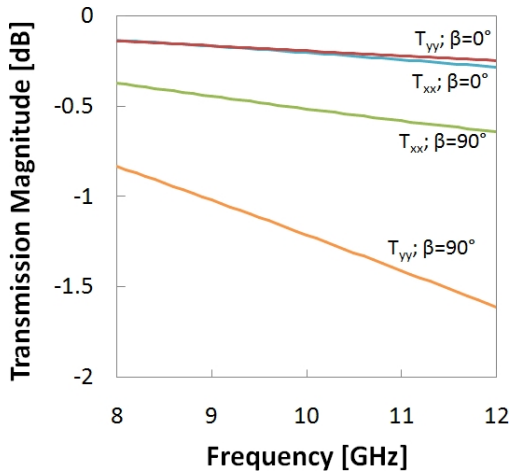

(d) T_{xy} and T_{xy}.

Figure 4.8: Analytically calculated S and T parameters for material with triclinic symmetry. The sample is measured at two different orientations.

now know. This is achieved following a similar procedure to the uniaxial and orthorhombic case, apart from the fact that we now have two measurements of a sample that has been rotated. Once the $\bar{\mathbf{\Gamma}}$ matrix has been obtained, (4.30) is used to extract ϵ_{zz}, μ_{zz}, and ϵ_{yz}. Subsequently, all other parameters may be retrieved using (4.26). The results are shown in Figure 4.9, with the extracted parameters matching exactly with the original material tensors, and thus verifying the sample rotation technique.

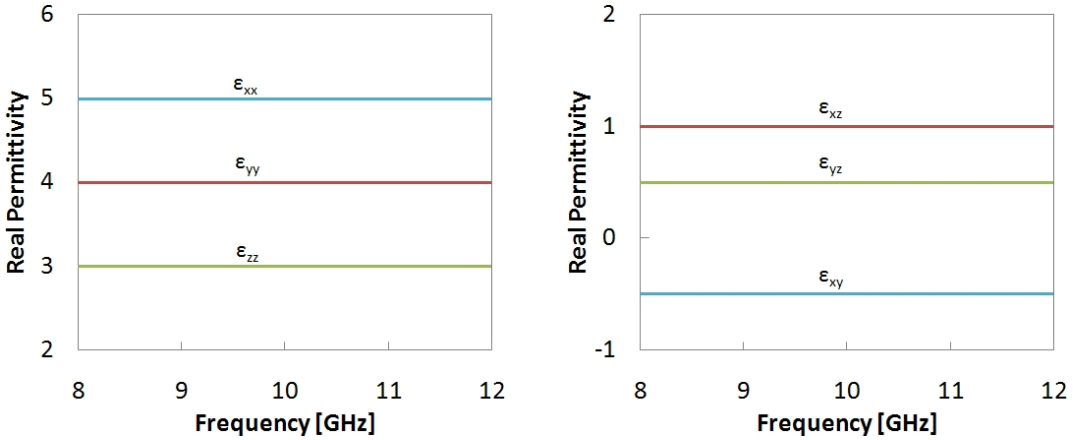

(a) ϵ_{xx}, ϵ_{yy}, and ϵ_{zz}.

(b) ϵ_{xy}, ϵ_{xz}, and ϵ_{yz}.

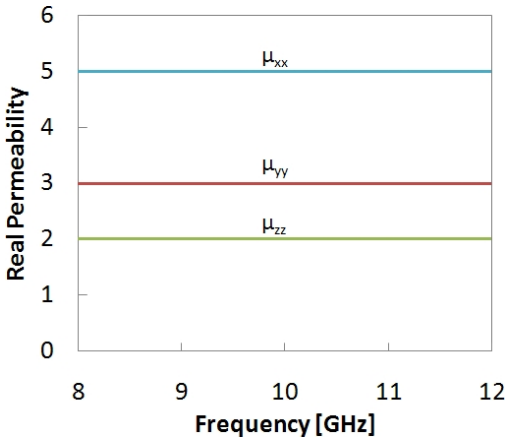

(c) μ_{xx}, μ_{yy}, and μ_{zz}.

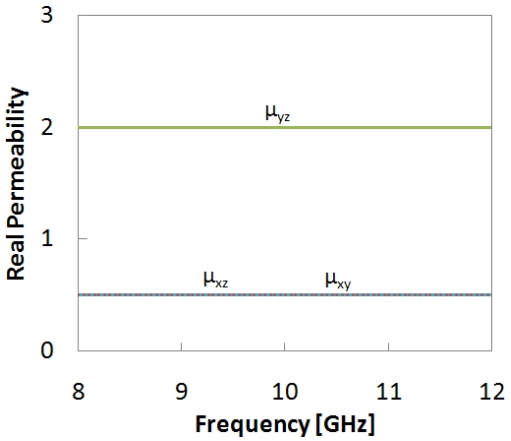

(d) μ_{xy}, μ_{xz}, and μ_{yz}.

Figure 4.9: Retrieved material parameters of a lossless triclinic material.

4.4.2 Spheres arranged within a planar slab

Dielectric spheres will now be arranged into a planar slab. We will attempt to retrieve the material parameters, while at the same time gaining an understanding of the number of layers of spheres required, such that we may obtain the characteristics of the *bulk* material, as discussed in section 4.3. The slab will be composed of a cubic arrangement of touching spheres, and will be infinitely periodic in the x- and y-directions. In the direction of propagation – the z-direction – there will be a finite number of layers of spheres, with the number varying from two to 16. The spheres have a size factor of $ka = 0.1$, and permittivity of $\epsilon = 10$. Figure 4.10 shows this arrangement of spheres into a slab, 16 sphere layers thick.

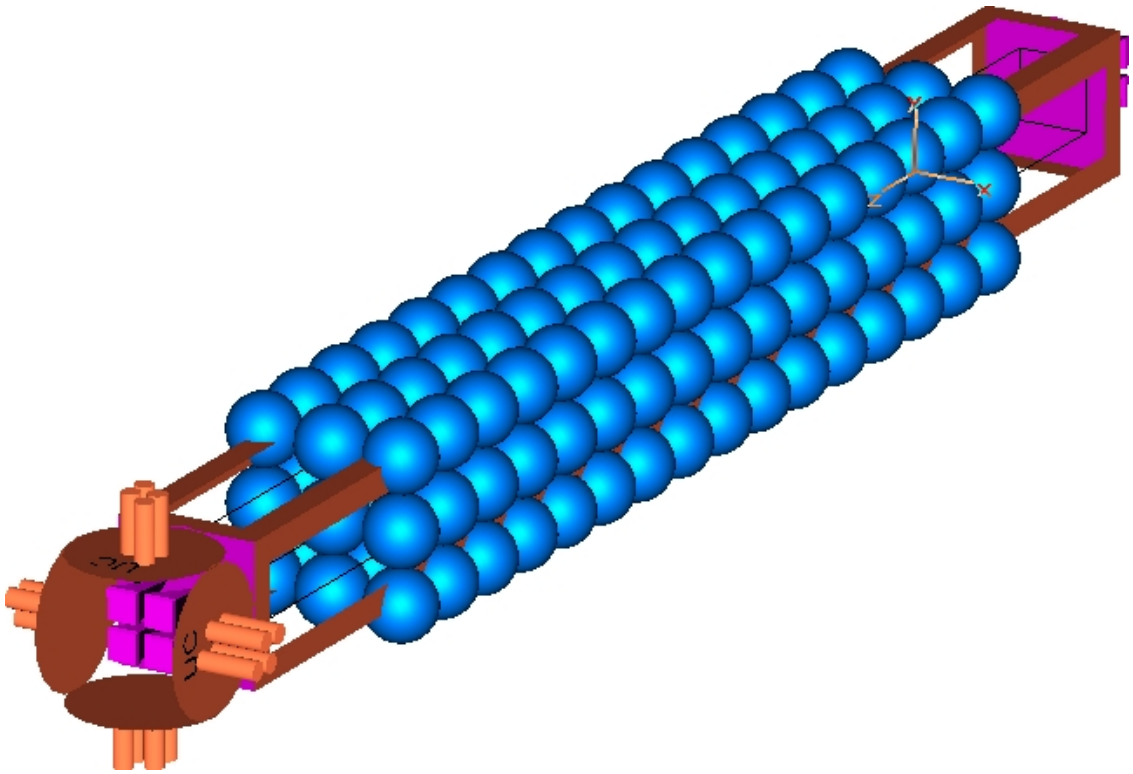

Figure 4.10: A doubly-infinite periodic arrangement of spheres into a slab, 16 sphere-layers thick.

This should enable us to obtain an understanding of the number of spheres that are required in order for the composite medium to behave as a homogeneous bulk material. This will be important for the design of devices formed with such a composite structure.

Once the S parameters have been obtained, and the transfer matrix calculated, our initial goal will be to determine the minimum number of sphere layers required, such that the slab may be treated as a homogeneous bulk material. Recall that the calculation of a transfer matrix requires the use of two different slab thicknesses. So, for example, a slab two sphere layers thick, and a slab four sphere layers thick, together will give one transfer matrix. The eigenvectors of this matrix should then be constant, assuming the material is homogeneous, if we compare them to those of matrices formed, for example, using slabs of thickness three and six spheres, or four and eight spheres (note that it is not required that slabs double in thickness, however it simplifies calculations and guarantees stability of solutions). In Figure 4.11 we compare the eigenvectors calculated using different slabs. Five different T-

matrices are calculated, each using a combination of two difference sample thicknesses. Each T-matrix is labeled based on the two samples used to form it, so for example, $T_{2|4}$ refers to the eigenvectors of the matrix created using slabs two and four sphere layers thick. Recall that for the extracted parameters to represent those of the bulk material, the eigenvectors should stay relatively constant as the slab thickness is changed. For this purpose, the relative difference is calculated between the eigenvectors of the different T-matrices, using $T_{4|8}$ as a reference. So in other words, the relative difference is found as:

$$\text{Relative Difference} = \left| \frac{T_{x|2x} - T_{4|8}}{T_{4|8}} \right|. \tag{4.38}$$

One would expect the relative difference between the eigenvectors to be close to zero once the retrieved properties match those of the bulk properties. In Figure 4.11 it is evident that for the thinnest slabs, $T_{2|4}$, there are large differences in the eigenvectors compared to $T_{4|8}$. We can thus conclude that the two sphere-layer thick slab cannot be treated as a homogeneous material; even though it is formed of spheres as with the other two, being only two spheres thick implies that the surface layer effects dominate over the bulk effects. However, on comparing both $T_{3|6}$ and $T_{6|12}$ to $T_{4|8}$, the relative differences between the eigenvectors are minimal. So with a thickness of three sphere-layers should be sufficient to retrieve the bulk parameters. Another point to note is that the relative differences of $T_{8|16}$ witness the effects of a longitudinal resonance at around 10 GHz, which results in errors in the extracted eigenvectors, and thus the material parameters, at those frequencies.

In Figures 4.12 and 4.13, the material parameters of the spheres are plotted. The composite structures show close to isotropic, and nonmagnetic behavior, as one would expect. ϵ_{yy} is not plotted as it is identical to ϵ_{xx}. The retrieved parameters are plotted only for the bulk cases, i.e., for $T_{3|6}$, $T_{4|8}$, and $T_{6|12}$. As expected, the very closely correlate to one another, with slight errors due to simulation inaccuracies. For $T_{2|4}$, the surface layer effects dominate, and so the retrieved parameters would not match with the expected bulk parameters. For

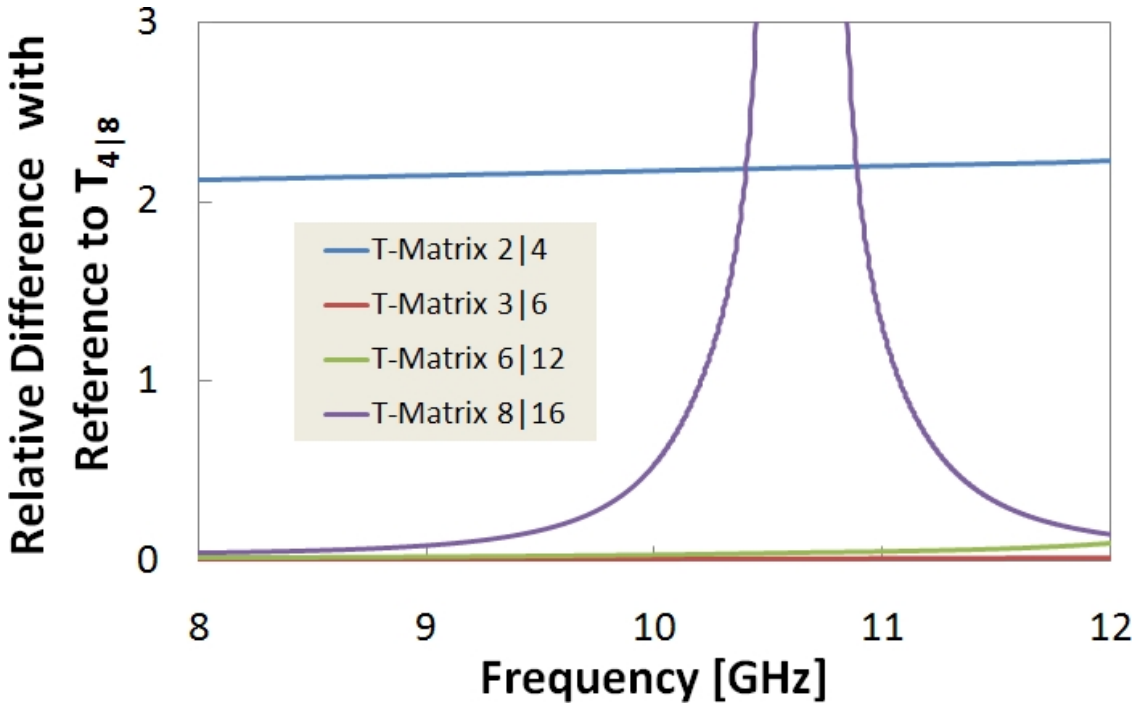

Figure 4.11: Relative differences between the eigenvectors of the T-matrices.

$T_{8|16}$, the retrieved parameters would be similar to those of the bulk parameters, although at the frequency of the longitudinal resonance, there would be large errors. Nevertheless, this confirms the procedure, with the homogeneity between the different slab thicknesses resulting in very well-matching extracted parameters, in fact so well that they cannot be easily distinguished on the plots.

4.5 Summary

A technique for retrieving the permittivity and permeability tensors of an anisotropic slab has been presented. Unlike previous techniques, this method allows characterization at oblique angles of incidence, and it is capable of characterizing even the most general, and non-symmetric of anisotropic materials. Furthermore, the eigenvalues may be compared in order to verify that the slab is thick enough, such that the extracted material properties are those of the bulk material. This is necessary for the use of the material in device design, allowing us to ascertain the minimum thickness of a homogeneous material that may be

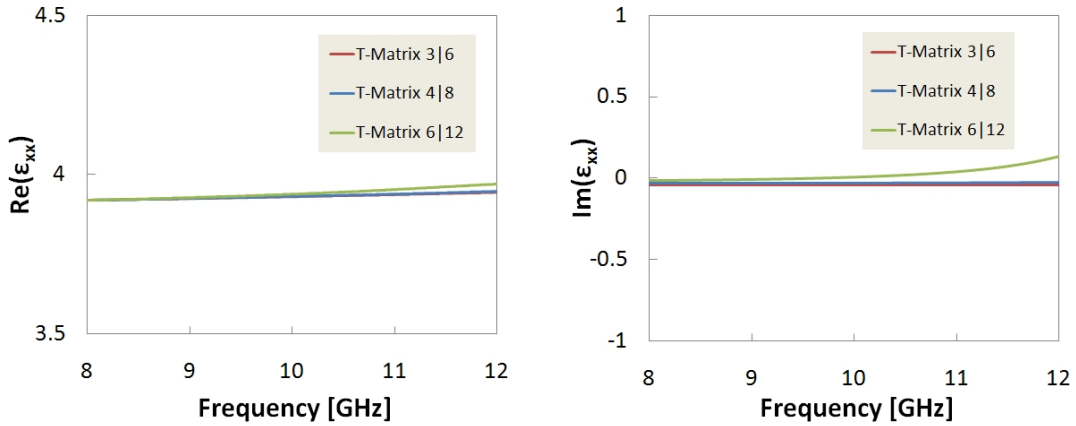

(a) $\mathrm{Re}(\epsilon_{xx})$.

(b) $\mathrm{Im}(\epsilon_{xx})$.

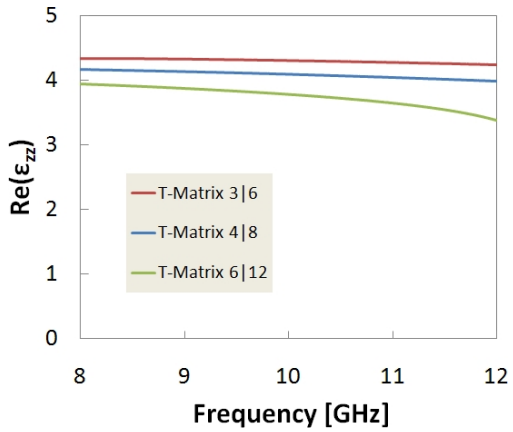

(c) $\mathrm{Re}(\epsilon_{zz})$.

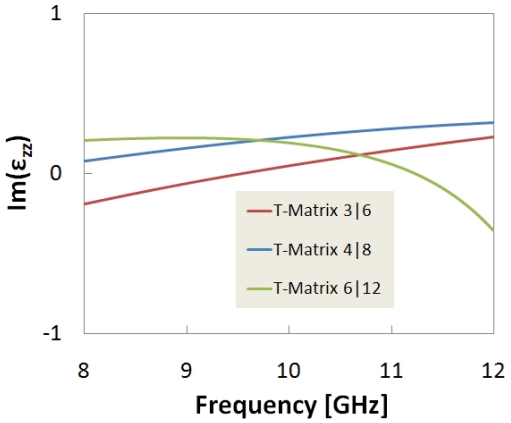

(d) $\mathrm{Im}(\epsilon_{zz})$.

Figure 4.12: Retrieved effective permittivities of cubic lattices of spheres, calculated using T-matrices formed with different slab thicknesses.

used.

The technique is based on the state variable approach, in which a transfer matrix is used to represent the fields on one side of the slab in terms of the fields on the other. S parameters must be measured for two different slab thicknesses, and for two different polarizations (TE and TM). An eigendecomposition of the transfer matrix will then provide information on the homogeneity of the slab, as well as allowing the retrieval of the material parameters.

The technique was verified, first with a uniaxial material, retrieving the parameters from simulation results. Next, a lossy, dispersive, orthorhombic material was simulated, and the parameters retrieved. In this case, the xx-, yy-, and zz-components of the tensors are

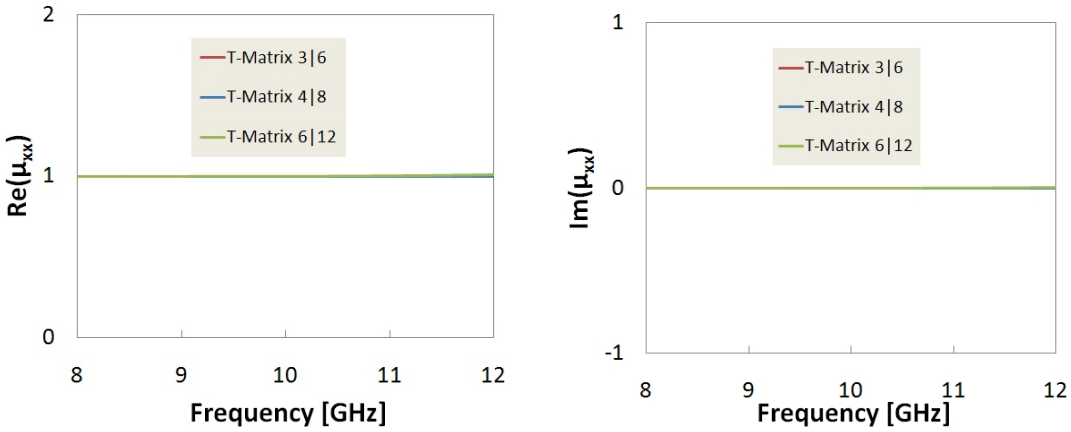

(a) Re(μ_{xx}).

(b) Im(μ_{xx}).

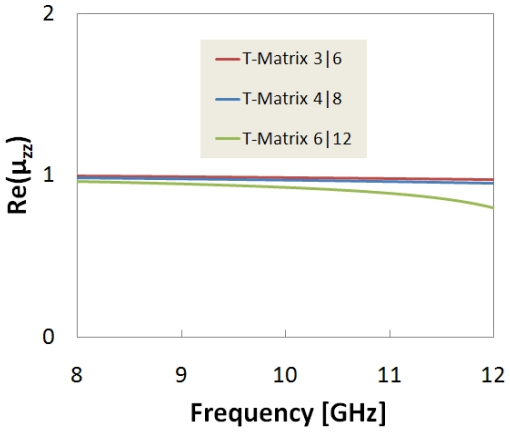

(c) Re(μ_{zz}).

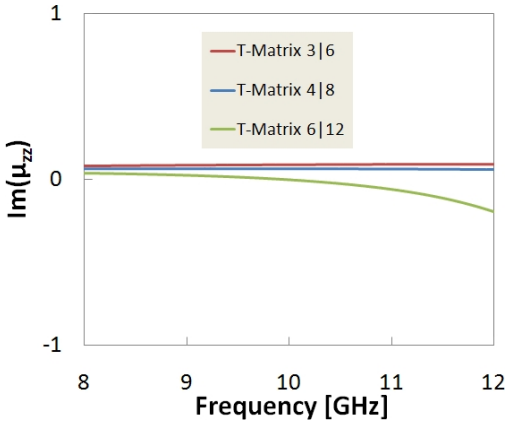

(d) Im(μ_{zz}).

Figure 4.13: Retrieved effective permeabilities of cubic lattices of spheres, calculated using T-matrices formed with different slab thicknesses.

all different, and so two different incident angle measurements were used to obtain the requisite number of equations. Finally, the technique was verified on the most general case of a triclinic material, in which there were twelve independent material parameters. As simulations were not capable of modeling this material, the parameters were retrieved from analytical calculations of the S parameters. Additionally, it was shown that only in the triclinic symmetry case, will a structure produce cross-polarization of an incident wave. Thus, it can be concluded that previous effective material models and extraction techniques, are insufficient if a change in the polarization of the incident wave is observed, as they are not capable of reproducing this behavior.

Additionally, the material parameters of a cubic lattice of spheres were extracted. It was concluded that for too thin a slab, homogeneity may not be assumed, as the extracted parameters will not match those of the bulk material. Instead, surface layer effects will dominate. Additionally, when there is a longitudinal resonance for a thick slab, the extraction procedure is inaccurate, as with other transmission methods. However, with an appropriate sample thickness, the extracted results match up extremely well.

Chapter 5

Conclusion

5.1 Summary

The goal of this work was to provide a method for designing and characterizing metamaterial structures within a group theoretical framework, relating the symmetry of the composite structures to their anisotropic material properties. In particular, dielectric spheres were characterized at terahertz frequencies, both through measurement and numerically. The measurements were performed using terahertz time-domain spectroscopy, which was also used for the characterization of ceramics. The sphere aggregates were numerically analyzed with the use of a novel, highly efficient technique based on the characteristic basis function method. Their effective material properties were subsequently investigated with various lattice symmetry arrangements. The anisotropic material parameters were extracted from the reflection and transmission coefficients at different angles of incidence, so that the entire $\bar{\boldsymbol{\epsilon}}$ and $\bar{\boldsymbol{\mu}}$ tensors could be retrieved. It was found that an isotropic material model is insufficient for representation of most metamaterials, and in many cases, a triclinic model is necessary. Furthermore, at resonance, the loss of homogeneity of dielectric metamaterials is demonstrated, and it is shown that traditional effective medium models are incapable of representing the structure accurately. Thus, we can conclude that for real-world device design incorporating metamaterials, it is imperative that:

- The effective medium representation of a metamaterial has been verified, and homo-

geneity confirmed, or,

- Ideally, full wave simulations or analytical techniques are used to fully describe the composite.

For application at microwave frequencies, the relative permittivity of a material is generally assumed to be relatively constant. However, as applications move to higher frequencies, particularly the terahertz frequencies, the material behavior will begin to change. Material characterization is thus very important, not only for device design, but also for metamaterial design, in which the properties of the constituent materials can vastly affect the properties of the metamaterial as a whole. A terahertz time-domain spectroscopy system was used for the dielectric characterization of ceramics, and for the measurement of transmission through lattices of dielectric spheres of resonant size. The characterization technique allowed the broadband extraction of the relative permittivities of lossy, non-magnetic dielectric materials. The extracted permittivities of different ceramics were then compared with good agreement to those obtained using microwave techniques at lower frequencies, and Fourier-transform infrared spectroscopy at frequencies above those allowed by THz TDS. Additionally, an error analysis was performed on the technique, to investigate the effects of measurement inaccuracies on the extracted results. It was found that losses in particular are sensitive to measurement errors which, as with other transmission methods, limits accuracy in determination of $\tan\delta$ for low loss samples. Transmission through arrays of Silicon Nitride spheres in various lattice arrangements were then measured.

A technique for calculating the scattered fields from an aggregate of spheres was developed. It was shown that the technique, based on the characteristic basis function method, is more efficient than the T-matrix formulation of multiple scattering, especially as sphere separations are increased. Furthermore, calculation speeds are increased significantly with the use of the Strassen matrix multiplication and inversion algorithms, in which large matrices are broken up into smaller block matrices, resulting in fewer operations. Additionally, it was shown that this technique can be applied to the solution of large matrix problems, by storing

the matrix on a physical drive, and only calling up to memory the smaller block matrices as they are needed. The developed techniques were applied to calculate the scattering from a large number of resonant spheres - a problem that would previously have been impossible on a single processor with limited memory.

A method for extracting the complex material tensors of an anisotropic homogeneous medium was established. The technique, effectively a generalization of the method we used for isotropic ceramic characterization at terahertz frequencies, allows the retrieval of the material characteristics of a slab from the reflection and transmission measurements. Excitation is at oblique incidence by TE and TM plane waves, with the measurement of two slabs of identical material but different thickness. Depending on the symmetry of the structure, either one of two different incident angles were needed for extraction: one for cubic (isotropic) and uniaxial symmetries, and two for orthorhombic, monoclinic and triclinic symmetries. It was also shown that only triclinic symmetries, with all off-axis tensor terms being non-zero, will change the polarization of an incident wave. Thus, previous material models for metamaterials could not sufficiently describe the structures, as they experience polarization changes, and so triclinic tensor forms were used. The technique was first verified analytically and with simulations, and then applied to extract the material parameters of the well known split-ring resonator structure. Finally, it was applied to investigate the effects of symmetry on effective media composed of lattices of spheres.

5.2 Future work

Research into metamaterials, and effective media, are continually ongoing. The extraction technique presented here, which allows the characterization of anisotropic materials at oblique incidence, holds many possibilities for further work. A more comprehensive study can be performed on the effective anisotropic material parameters of various symmetries of structures. All classes of effective media would be well served by an analysis into their isotropy, and this technique is easily applied, both numerically, and also experimentally.

and in fact, an experimental verification of the technique could be a top priority for any future work. At microwave frequencies, a free space measurement system would be ideal for characterization. At terahertz frequencies, terahertz time-domain spectroscopy should work well, although with the added difficulty that angle variations are difficult to achieve.

Appendix A

Special Functions

A number of special functions are useful for solving various scattering problems. This appendix will cover the special functions that are relevant to the scattering problems encountered in this thesis. For calculation purposes, the recurrence relations are of particular interest. Equations are referenced from [147, 165].

A.1 Cylindrical Bessel functions

A.1.1 Definition

The cylindrical Bessel functions are the solutions to the Bessel differential equation, given by

$$z^2\frac{d^2f}{dz^2} + z\frac{df}{dz} + \left[z^2 - n^2\right] z = 0, \quad n \in \mathbb{C} \tag{A.1}$$

where n is an arbitrary real or complex number.

A.1.2 Solutions

Two linearly independent solutions to (A.1) are $J_n(z)$ and $Y_n(z)$, the cylindrical Bessel functions of the first and second kind, respectively. We can define a linear combination of

the two functions, called the Hankel functions, as

$$H_n^{(1)}(z) = J_n(z) + jY_n(z) \tag{A.2a}$$

$$H_n^{(2)}(z) = J_n(z) - jY_n(z). \tag{A.2b}$$

A.1.3 Recurrence relations

It would be relatively computationally intensive to calculate every required special function value individually, especially in cases where hundreds, or thousands of different solutions are required. A much more efficient technique would be to recursively calculate all required values, from just a few known initial values. Defining F_n as a linear combination of any of the Bessel (or Hankel) functions, the following recurrence relations are useful for calculating the n-th order Bessel functions, or their derivatives, for a particular z:

$$\frac{2n}{z}F_n(z) = F_{n-1}(z) + F_{n+1}(z) \tag{A.3a}$$

$$2\frac{d}{dz}F_n(z) = F_{n-1}(z) - F_{n+1}(z) \tag{A.3b}$$

$$z\frac{d}{dz}F_n(z) = nF_n(z) - zF_{n+1}(z) = -nF_n(z) + zF_{n-1}(z) \tag{A.3c}$$

$$\int \left[F_n(z)\right]^2 z dz = \frac{z^2}{2}\left[F_n^2(z) - F_{n-1}(z)F_{n+1}(z)\right]. \tag{A.3d}$$

It is important to note that the recurrence relations could diverge if we use upward recurrence (i.e. begin with values at $n = 0$ and $n = 1$ to solve for higher values of n), and so downward recurrence is preferable [147, p.278].

A.2 Spherical Bessel functions

A.2.1 Definition

Of particular use in solving scattering problems with a spherical geometry, are the spherical Bessel functions; they form the radial portion of the solution to the wave equation in spherical coordinates. The Helmholtz equation in spherical coordinates is the spherical Bessel differential equation

$$r^2\frac{d^2R}{dr^2} + 2r\frac{dR}{dr} + \left[k^2r^2 - n(n+1)\right]R = 0, \quad k \in \mathbb{C}. \tag{A.4}$$

A.2.2 Solutions

The solution to the differential equation is, in fact, related to the cylindrical Bessel functions of half integral order,

$$j_n(kr) = \sqrt{\frac{\pi}{2kr}}J_{n+1/2}(kr) \quad n \in \mathbb{Z} \tag{A.5a}$$

$$y_n(kr) = \sqrt{\frac{\pi}{2kr}}Y_{n+1/2}(kr) = (-1)^{n+1}\sqrt{\frac{\pi}{2kr}}J_{-n-1/2}(kr). \tag{A.5b}$$

We can also define the spherical Hankel functions,

$$h_n^{(1)}(kr) = j_n(kr) + jy_n(kr) \tag{A.5c}$$

$$h_n^{(2)}(kr) = j_n(kr) - jy_n(kr). \tag{A.5d}$$

A.2.3 Recurrence relations

Again, recurrence relations are useful in solving various scattering problems, and will make numerical techniques more efficient. Useful recurrence relations are given as:

$$f_{n-1}(z) + f_{n+1}(z) = (2n+1)\frac{f_n(z)}{z} \tag{A.6a}$$

$$nf_{n-1}(z) - (n+1)f_{n+1}(z) = (2n+1)\frac{d}{dz}f_n(z) \tag{A.6b}$$

$$\frac{n+1}{z}f_n(z) + \frac{d}{dz}f_n(z) = f_{n-1}(z) \tag{A.6c}$$

$$\frac{n}{z}f_n(z) - \frac{d}{dz}f_n(z) = f_{n+1}(z), \tag{A.6d}$$

where f_n is a linear combination of the spherical Bessel (or Hankel) functions. In a similar manner to the cylindrical Bessel functions, it is preferrable to use downward recursion [147, p.284].

A.3 Riccati-Bessel functions

A.3.1 Definition

The Riccati-Bessel functions are special functions that occur in the solution for scattering from a sphere. The Riccati differential equation is,

$$z^2\frac{d^2R}{dz^2} + \left[z^2 - n(n+1)\right]R = 0, \quad k \in \mathbb{C}. \tag{A.7}$$

A.3.2 Solutions

The solution is very closely related to the spherical Bessel functions:

$$\psi_n(z) = zj_n(z) \quad n \in \mathbb{Z} \tag{A.8a}$$

$$\eta_n(z) = -zy_n(z) \tag{A.8b}$$

$$\xi_n(z) = zh_n^{(1)}(z) \tag{A.8c}$$

$$\zeta_n(z) = zh_n^{(2)}(z). \tag{A.8d}$$

A.3.3 Recurrence relations

Defining g_n as a linear combination of any of the Riccati-Bessel functions, we have the following recurrence relations,

$$(2n+1)\frac{d}{dz}g_n(z) = (n+1)g_{n-1} - ng_{n+1} \tag{A.9a}$$

$$\frac{d}{dz}g_n(z) = g_{n-1}(z) - nf_n(z) = (n+1)f_n(z) - g_{n+1}(z) \tag{A.9b}$$

A.4 Associated Legendre functions

A.4.1 Definition

Another important class of special functions, for the solution of scattering problems with spherical geometries, are the associated Legendre functions. These functions form part of the angular (zenith, or elevation) portion of the solution to the wave equation in spherical coordinates. The associated Legendre differential equations is

$$(1-x^2)\frac{d^2y}{dx^2} - 2x\frac{dy}{dx} + \left(n[n+1] - \frac{m^2}{1-x^2}\right)y = 0, \quad x \in [-1,1]. \tag{A.10}$$

A.4.2 Solutions

The solutions to the differential equation are the associated Legendre functions,

$$P_n^m(x) = \frac{(1-x^2)^{m/2}}{2^n n!}\frac{d^{m+n}}{dx^{m+n}}(x^2-1)^n, \quad n \in \mathbb{N}, -n \leq m \leq n. \tag{A.11a}$$

The functions are of most important to us when $x \equiv \cos\theta$:

$$P_n^m(\cos\theta) = \frac{(-1)^n}{2^n n!}(\sin\theta)^m \frac{d^{m+n}}{d(\cos\theta)^{m+n}}(\sin\theta)^n. \tag{A.11b}$$

The following functions are also useful in sphere scattering problems:

$$\tau_n^m(\theta) = \frac{mP_n^m(\cos\theta)}{\sin\theta} \tag{A.12a}$$

$$\pi_n^m(\theta) = \frac{d}{d\theta}P_n^m(\cos\theta) \tag{A.12b}$$

A.4.3 Recurrence relations

The first few associated Legendre functions are given as,

$$P_0^0(\cos\theta) = 1, \quad P_1^0(\cos\theta) = \cos\theta, \quad P_1^1(\cos\theta) = \sin\theta, \quad P_2^1(\cos\theta) = \tfrac{3}{2}\sin 2\theta. \tag{A.13a}$$

These can be used to recursively determine subsequent functions, using the following relationships:

$$P_{n+1}^n = (2n+1)\sin\theta\, P_n^{n-1} \tag{A.13b}$$

$$P_{n+1}^{n+1} = (2n+1)\sin\theta\, P_n^n \tag{A.13c}$$

$$P_{n+1}^m = \frac{(2n+1)\cos\theta\, P_n^m - (n+m)P_{n-1}^m}{n-m+1} \tag{A.13d}$$

$$P_n^{-m} = (-1)^m \frac{(n-m)!}{(n+m)!}P_n^m. \tag{A.13e}$$

τ_n^m may similarly be found using:

$$\tau_0^0(\cos\theta) = \tau_1^0(\cos\theta) = 0, \quad \tau_1^1(\cos\theta) = 1 \quad \tau_2^1(\cos\theta) = 3\cos\theta, \tag{A.14a}$$

and

$$\tau_{n+1}^{n} = \frac{n(2n+1)}{n-1}\sin\theta\,\tau_n^{n-1} \tag{A.14b}$$

$$\tau_{n+1}^{n+1} = \frac{(n+1)(2n+1)}{n}\sin\theta\,\tau_n^{n} \tag{A.14c}$$

$$\tau_{n+1}^{m} = \frac{(2n+1)\cos\theta\,\tau_n^m - (n+m)\tau_{n-1}^m}{n-m+1} \tag{A.14d}$$

$$\tau_n^{-m} = (-1)^{m+1}\frac{(n-m)!}{(n+m)!}\tau_n^m. \tag{A.14e}$$

For $\cos\theta = \pm 1$, π_n^m will take the special values,

$$\pi_n^m(\pm 1) = \frac{1}{2}(\pm 1)^n n(n+1)\delta_{m1} \tag{A.15a}$$

Otherwise, it can be found using the initial values,

$$\pi_0^0(\cos\theta) = \pi_0^1(\cos\theta) = 0, \quad \pi_1^0(\cos\theta) = -\sin\theta \quad \pi_1^1(\cos\theta) = \cos\theta \tag{A.15b}$$

as well as the previously calculated τ_n^m coefficients, and the following relationships,

$$\pi_n^0 = \frac{2n-1}{n-1}\cos\theta\,\pi_{n-1}^0 - \frac{n}{n-1}\pi_{n-2}^0 \tag{A.15c}$$

$$\pi_n^m = \frac{n-m+1}{m}\pi_{n+1}^m - \frac{(n+1)}{m}\cos\theta\,\pi_n^m \tag{A.15d}$$

$$\pi_n^{-m} = (-1)^m\frac{(n-m)!}{(n+m)!}\pi_n^m. \tag{A.15e}$$

A.4.4 Orthogonality

The following orthogonality relationships are useful in solving sphere scattering problems:

$$\int_{-1}^{+1}\frac{P_n^m(z)P_n^l(z)}{1-z^2}dz = \frac{1}{m}\frac{(n+m)!}{(n-m)!}\delta_{ml} \tag{A.16a}$$

$$\int_{-1}^{+1} P_n^m(z) P_l^m(z) dz = \frac{2}{2n+1} \frac{(n+m)!}{(n-m)!} \delta_{nl}, \quad n \geq m \tag{A.16b}$$

$$\int_0^{\pi} \left(\frac{dP_n^m}{d\theta} \frac{dP_l^m}{d\theta} + \frac{m^2}{\sin^2 \theta} P_n^m P_l^m \right) \sin\theta d\theta = \frac{2n(n+1)}{2n+1} \frac{(n+m)!}{(n-m)!} \delta_{nl}. \tag{A.16c}$$

A.5 Spherical harmonic functions

A.5.1 Definition

These are the angular portion of the solution to Laplace's equation,

$$\nabla^2 f(r, \theta, \phi) = 0 \tag{A.17}$$

A.5.2 Solutions

The spherical harmonics are functions of the associated Legendre functions, and an exponential phase term, along with a normalizing constant. In this thesis it is defined as follows,

$$Y_n^m(\theta, \phi) = (-1)^m \sqrt{\frac{2n+1}{4\pi} \frac{(n-m)!}{(n+m)!}} P_n^m(\cos\theta) e^{jm\phi}. \tag{A.18}$$

Appendix B

Transformation properties of spherical waves

B.1 Scalar translation theorem

B.1.1 The scalar wave equation

The scalar Helmholtz equation, the time-invariant form of the wave equation, is defined as,

$$\nabla^2\psi + k^2\psi = 0. \tag{B.1}$$

In a spherical coordinate system, a solution can be found, using the separation of variables,

$$\psi_{mn}^{(J)}(r,\theta,\phi) = z_n^{(J)}(kr)Y_n^m(\theta,\phi), \quad n,m \in \mathbb{N}, n \geq 0, -n \leq m \leq n \tag{B.2a}$$

where $Y_n^m(\theta,\phi)$ is the spherical harmonic function, and $z_n^{(J)}(kr)$ represents a spherical Bessel function of the J-th kind, i.e., j_n, y_n, $h_n^{(1)}$, and $h_n^{(2)}$ for $J = 1$ to 4, respectively. Both of these functions have been defined in Appendix A. It will also be beneficial to represent the scalar wave function ψ in matrix form,

$$\boldsymbol{\psi}^{(J)}(r,\theta,\phi) = \left\{\cdots \psi_{mn}^{(J)}(r,\theta,\phi)\cdots\right\}^T. \tag{B.2b}$$

B.1.2 Definition

Addition theorem in three dimensions

Critical to the solution of a multiple scattering problem in any coordinate system, is the transformation of a wave function between different coordinate system origins. For an observation point x, the scalar wave equation in a coordinate system j can be represented in terms of a summation of scalar wave equations at i (see Figure 3.2), as well as the translation coefficients β, such that,

$$\psi_{mn}^{(J)}(\mathbf{r}_{jx}) = \sum_{\nu=0}^{\infty} \sum_{\mu=-\nu}^{\nu} \psi_{\mu\nu}^{(J)}(\mathbf{r}_{ix}) \beta_{\mu\nu}^{mn}(j,i) \tag{B.3a}$$

$$\beta_{\mu\nu}^{mn}(j,i) = \sum_{p} 4\pi j^{(\nu+p-n)} \psi_{(m-\mu)p}^{(J)}(\mathbf{r}_{ji}) A(m,n,-\mu,\nu,p) \tag{B.3b}$$

$$A(m,n,-\mu,\nu,p) = (-1)^m \sqrt{\frac{(2n+1)(2\nu+1)(2p+1)}{4\pi}} \cdot \begin{pmatrix} n & \nu & p \\ 0 & 0 & 0 \end{pmatrix} \begin{pmatrix} n & \nu & p \\ -m & \mu & m-\mu \end{pmatrix}, \tag{B.3c}$$

where $\begin{pmatrix} n & \nu & p \\ m & \mu & q \end{pmatrix}$ is the Wigner $3j$ symbol [166]. In matrix formulation, this is,

$$\boldsymbol{\psi}(\mathbf{r}_{jx}) = \boldsymbol{\psi}(\mathbf{r}_{ix}) \cdot \bar{\boldsymbol{\beta}}_{ji}, \tag{B.4a}$$

where,

$$\bar{\boldsymbol{\beta}} = \overset{mn}{\downarrow} \left(\beta_{\mu\nu}^{mn} \right) \overset{\mu\nu\longrightarrow}{}. \tag{B.4b}$$

These theorems will translate from a coordinate system j to a coordinate system i.

B.1.3 Recurrence relations

A number of different recurrence relations have been derived for the translation theorems, e.g. [124, 140, 167]. The formulas of Chew [140] are presented here, where $\alpha_{\mu\nu}^{mn}$ represents the outgoing case ($J = 3$), and $\beta_{\mu\nu}^{mn}$ represents the regular case ($J = 1$):

$$\alpha_{\mu\nu}^{00} = (-1)^{\mu+\nu}\sqrt{4\pi}Y_{\nu}^{-\mu}(\theta_{ji}, \phi_{ji})h_{\nu}^{(1)}(kr_{ji}) \tag{B.5a}$$

$$\beta_{\mu\nu}^{00} = (-1)^{\mu+\nu}\sqrt{4\pi}Y_{\nu}^{-\mu}(\theta_{ji}, \phi_{ji})j_{\nu}(kr_{ji}) \tag{B.5b}$$

$$a_{mn}^{+}\beta_{\mu\nu}^{m(n+1)} = -a_{mn}^{-}\beta_{\mu\nu}^{m(n-1)} + a_{\mu(\nu-1)}^{+}\beta_{\mu(\nu-1)}^{mn} + a_{\mu(\nu+1)}^{-}\beta_{\mu(\nu+1)}^{mn} \tag{B.5c}$$

$$b_{nn}^{+}\beta_{\mu\nu}^{(n+1)(n+1)} = b_{(\mu-1)(\nu-1)}^{+}\beta_{(\mu-1)(\nu-1)}^{nn} + b_{(\mu-1)(\nu+1)}^{-}\beta_{(\mu-1)(\nu+1)}^{nn}, \tag{B.5d}$$

where,

$$a_{mn}^{+} = -\sqrt{\frac{(n+m+1)(n-m+1)}{(2n+1)(2n+3)}} \tag{B.6a}$$

$$a_{mn}^{-} = \sqrt{\frac{(n+m)(n-m)}{(2n+1)(2n-1)}} \tag{B.6b}$$

$$b_{mn}^{+} = \sqrt{\frac{(n+m+2)(n+m+1)}{(2n+1)(2n+3)}} \tag{B.6c}$$

$$b_{mn}^{-} = \sqrt{\frac{(n-m)(n-m-1)}{(2n+1)(2n-1)}}. \tag{B.6d}$$

B.2 Vector translation theorem

B.2.1 The vector wave equation

Electromagnetic scattering problems are inherently vectorial in nature, and so we must solve the vector form of the wave equation,

$$\nabla \times \nabla \times \mathbf{\Psi} - k^2\mathbf{\Psi} = 0. \tag{B.7}$$

Here, Ψ is a vector function. Stratton gives the solutions to this equation in terms of the three vector functions, $\mathbf{L}$, $\mathbf{M}$, and $\mathbf{N}$:

$$\mathbf{L} = \nabla\boldsymbol{\Psi} \tag{B.8a}$$

$$\mathbf{M} = \nabla \times \mathbf{R}\boldsymbol{\Psi} = \mathbf{L} \times \mathbf{R} = \frac{1}{k}\nabla \times \mathbf{N} \tag{B.8b}$$

$$\mathbf{N} = \frac{1}{k}\nabla \times \mathbf{M}, \tag{B.8c}$$

where the position vector $\mathbf{R}$ is defined in the (r, θ, ϕ) system as

$$\mathbf{R} = (\hat{\mathbf{r}}, \hat{\boldsymbol{\theta}}, \hat{\boldsymbol{\phi}}). \tag{B.9}$$

For a divergenceless incident field $\mathbf{L} = 0$. We can thus define,

$$\boldsymbol{\Psi} = \{\cdots \mathbf{N}_{mn} \cdots \qquad \cdots \mathbf{M}_{mn} \cdots\}^T. \tag{B.10}$$

B.2.2 Definition

In matrix form, the vector translation theorems are,

$$Ou\boldsymbol{\Psi}(k\mathbf{r}_{jx}) = \bar{\boldsymbol{\alpha}}_{ij} \cdot Rg\boldsymbol{\Psi}(k\mathbf{r}_{ix}) \qquad \text{if } \left|\mathbf{r}_{ix}\right| < \left|\mathbf{r}_{ij}\right| \tag{B.11a}$$

$$Ou\boldsymbol{\Psi}(k\mathbf{r}_{jx}) = \bar{\boldsymbol{\beta}}_{ij} \cdot Ou\boldsymbol{\Psi}(k\mathbf{r}_{ix}) \qquad \text{if } \left|\mathbf{r}_{ix}\right| > \left|\mathbf{r}_{ij}\right| \tag{B.11b}$$

$$Rg\boldsymbol{\Psi}(k\mathbf{r}_{jx}) = \bar{\boldsymbol{\beta}}_{ij} \cdot Rg\boldsymbol{\Psi}(k\mathbf{r}_{ix}) \qquad \text{if } \forall\left|\mathbf{r}_{ix}\right|, \tag{B.11c}$$

where $Rg\boldsymbol{\Psi}$ refers to the regular vector wave function, while $Ou\boldsymbol{\Psi}$ is the outgoing function. The translation matrices are defined as,

$$\bar{\boldsymbol{\alpha}}_{ij} = \left(\begin{array}{c|c} \bar{\mathbf{A}}_{ij} & \bar{\mathbf{B}}_{ij} \\ \hline \bar{\mathbf{B}}_{ij} & \bar{\mathbf{A}}_{ij} \end{array}\right) \tag{B.12a}$$

$$\bar{\boldsymbol{\beta}}_{ij} = \left(\begin{array}{c|c} \bar{\mathbf{C}}_{ij} & \bar{\mathbf{D}}_{ij} \\ \hline \bar{\mathbf{D}}_{ij} & \bar{\mathbf{C}}_{ij} \end{array}\right). \tag{B.12b}$$

The $\bar{\mathbf{A}}$, $\bar{\mathbf{B}}$, $\bar{\mathbf{C}}$, and $\bar{\mathbf{D}}$ matrices are formed in the same manner as $\bar{\boldsymbol{\beta}}$ in (B.4b).

B.2.3 Recurrence relations

Various different recurrence relations have been derived for the vector translation theorems [121, 122, 124, 141, 168], however we will present those of [141].

$$\begin{aligned} A_{\mu\nu}^{mn} = \alpha_{\mu\nu}^{mn} &+ r_{ji}\sin\theta_{ji}\frac{e^{-j\phi_{ji}}}{2(\nu+1)}\sqrt{\frac{(\nu-\mu+2)(\nu-\mu+1)}{(2\nu+1)(2\nu+3)}}\alpha_{(\mu-1)(\nu+1)}^{mn} \\ &- r_{ji}\sin\theta_{ji}\frac{e^{-j\phi_{ji}}}{2\nu}\sqrt{\frac{(\nu+\mu-1)(\nu+\mu)}{(2\nu-1)(2\nu+1)}}\alpha_{(\mu-1)(\nu-1)}^{mn} \\ &- r_{ji}\sin\theta_{ji}\frac{e^{j\phi_{ji}}}{2(\nu+1)}\sqrt{\frac{(\nu+\mu+2)(\nu+\mu+1)}{(2\nu+1)(2\nu+3)}}\alpha_{(\mu+1)(\nu+1)}^{mn} \\ &+ r_{ji}\sin\theta_{ji}\frac{e^{j\phi_{ji}}}{2\nu}\sqrt{\frac{(\nu-\mu)(\nu-\mu-1)}{(2\nu-1)(2\nu+1)}}\alpha_{(\mu+1)(\nu-1)}^{mn} \\ &+ r_{ji}\cos\theta_{ji}\frac{1}{\nu+1}\sqrt{\frac{(\nu+\mu+1)(\nu-\mu+1)}{(2\nu+1)(2\nu+3)}}\alpha_{\mu(\nu+1)}^{mn} \\ &+ r_{ji}\cos\theta_{ji}\frac{1}{\nu}\sqrt{\frac{(\nu+\mu)(\nu-\mu)}{(2\nu-1)(2\nu+1)}}\alpha_{\mu(\nu-1)}^{mn} \end{aligned} \tag{B.13a}$$

$$\begin{aligned} B_{\mu\nu}^{mn} = r_{ji}\cos\theta_{ji}\frac{j\mu}{\nu(\nu+1)}\alpha_{\mu\nu}^{mn} + r_{ji}\sin\theta_{ji}\frac{j}{2\nu(\nu+1)}\cdot\big[\ &\sqrt{(\nu-\mu)(\nu+\mu+1)}\cdot e^{j\phi_{ji}}\cdot\alpha_{(\mu+1)\nu}^{mn} \\ &+\sqrt{(\nu+\mu)(\nu-\mu+1)}\cdot e^{-j\phi_{ji}}\cdot\alpha_{(\mu-1)\nu}^{mn}\big], \end{aligned} \tag{B.13b}$$

where α is calculated recursively using the formulas from (B.5). For the calculation of the coefficients of $\bar{\mathbf{C}}$ and $\bar{\mathbf{D}}$, replace α in (B.13) with β.

Bibliography

[1] H. A. Gebbie, N. W. B. Stone, and F. D. Findlay. A stimulated emission source at 0.34 millimetre wave-length. *Nature*, 202(4933):685, May 1964.

[2] H. A. Gebbie, N. W. B. Stone, F. D. Findlay, and E. C. Pyatt. Absorption and refractive index measurements at a wave-length of 0.34 mm. *Nature*, 205(4969):377–378, January 1965.

[3] J. E. Chamberlain, F. D. Findlay, and H. A. Gebbie. Refractive index of air at 0.337-mm wave-length. *Nature*, 206(4987):886–887, May 1965.

[4] J. Faist, F. Capasso, D. L. Sivco, C. Sirtori, A. L. Hutchinson, and A. Y. Cho. Quantum cascade laser. *Science*, 264(4):553–556, 1994.

[5] R. Koehler, A. Tredicucci, F. Beltram, H. E. Beere, E. H. Linfield, A. G. Davies, D. A. Ritchie, R. C. Iotti, and F Rossi. Terahertz semiconductor-heterostructure laser. *Nature*, 417:156–159, May 2002.

[6] M. Rochat, L. Ajili, H. Willenberg, J. Faist, H. Beere, G. Davies, E. Linfield, and D. Ritchie. Low-threshold terahertz quantum-cascade lasers. *Applied Physics Letters*, 81(8):1381–1383, August 2002.

[7] D. H. Auston, K. P. Cheung, J. A. Valdmanis, and D. A. Kleinman. Cherenkov radiation from femtosecond optical pulses in electro-optic media. *Physical Review Letters*, 53(16):1555–1558, October 1984.

[8] Ch. Fattinger and D. Grischkowsky. Point source terahertz optics. *Applied Physics Letters*, 53(16):1480–1482, October 1988.

[9] Q. Wu and X.-C. Zhang. Free-space electro-optic sampling of terahertz beams. *Applied Physics Letters*, 67(24):3523–3525, December 1995.

[10] T. G. Phillips and J. Keene. Submillimeter astronomy [heterodyne spectroscopy]. *Proceedings of the IEEE*, 80(11):1662–1678, November 1992.

[11] B. Ferguson and X. C. Zhang. Materials for terahertz science and technology. *Nature Materials*, 1(1):26–33, September 2002.

[12] B. Ferguson, S. Wang, D. Gray, D. Abbott, and X. C. Zhang. Towards functional 3 D T-ray imaging. *Physics in Medicine and Biology*, 47(21):3735–3742, November 2002.

[13] W. L. Chan, J. Deibel, and D. M. Mittleman. Imaging with terahertz radiation. *Reports on Progress in Physics*, 70(8):1325–1379, August 2007.

[14] P. H. Siegel. Terahertz technology in biology and medicine. *IEEE Transactions of Microwave Theory and Techniques*, 52(10):2438–2447, October 2004.

[15] P. H. Siegel. Thz instruments for space. *Antennas and Propagation, IEEE Transactions on*, 55(11):2957–2965, November 2007.

[16] H.-B. Liu, H. Zhong, N. Karpowicz, Y. Chen, and X.-C. Zhang. Terahertz spectroscopy and imaging for defense and security applications. *Proceedings of the IEEE*, 95(8):1514–1527, August 2007.

[17] R. Appleby and H. B. Wallace. Standoff detection of weapons and contraband in the 100 GHz to 1 THz region. *IEEE Transactions on Antennas and Propagation*, 55(11):2944–2956, November 2007.

[18] PH Siegel. Terahertz technology. *Microwave Theory and Techniques, IEEE Transactions on*, 50(3):910–928, 2002.

[19] C. A. Schmuttenmaer. Exploring dynamics in the far-infrared with terahertz spectroscopy. *Chemical Reviews*, 104(4):1759–1779, April 2004.

[20] M. Tonouchi. Cutting-edge terahertz technology. *Nature Photonics*, 1(2):97–105, February 2007.

[21] D. Mittleman. *Sensing with terahertz radiation*. Springer series in optical sciences. Springer, Berlin, 1^{st} edition, June 2004.

[22] K. Sakai. *Terahertz Optoelectronics*. Topics in Applied Physics. Springer, Berlin, 1^{st} edition, July 2005.

[23] R. M. Walser. Electromagnetic metamaterials. *Proceedings of SPIE*, 4467:1, 2001.

[24] Werner S. Weiglhofer and Akhlesh Lakhtakia, editors. *Introduction to Complex Mediums for Optics and Electromagnetics*. SPIE Publications, Bellingham, WA, USA, 2003.

[25] R. Rashed. A pioneer in anaclastics: Ibn Sahl on burning mirrors and lenses. *Isis*, 81(3):464–491, 1990.

[26] A. Kwan, J. Dudley, and E. Lantz. Who really discovered Snell's law? *Physics World*, 15(4):64, April 2002.

[27] Abu Ali al-Hasan ibn al-Hasan ibn al Haytham. *Book of Optics*. Baghdad, 1021.

[28] R. Rashed. *Géométrie et dioptrique au Xe siècle Ibn Sahl, Al-Qūhi et Ibn al-Haytham*. Collection Sciences et philosophie arabes. Textes et études. Les Belles Lettres, Paris, France, 1993.

[29] V. G Veselago. The electrodynamics of substances with simultaneously negative values of ϵ and μ. *Soviet Physics Uspekhi*, 10(4):509–514, 1968.

[30] Horace Lamb. On group-velocity. *Proceedings of the London Mathematical Society*, 2(1):473, 1904.

[31] H. C. Pocklington. Growth of a wave-group when the group-velocity is negative. *Nature*, 71:607–608, 1905.

[32] A. Schuster. *An introduction to the theory of optics*. Edward Arnold, London, UK, 1904.

[33] H. R. Johnson. Backward-wave oscillators. *Proceedings of the IRE*, 43(6):684–697, June 1955.

[34] J. B. Pendry, A. J. Holden, W. J. Stewart, and I. Youngs. Extremely low frequency plasmons in metallic mesostructures. *Physical Review Letters*, 76(25):4773–4776, Jun 1996.

[35] J. B. Pendry. Negative refraction makes a perfect lens. *Phys. Rev. Lett.*, 85(18):3966–3969, Oct 2000.

[36] D. R. Smith, Willie J. Padilla, D. C. Vier, S. C. Nemat-Nasser, and S. Schultz. Composite medium with simultaneously negative permeability and permittivity. *Physical Review Letters*, 84(18):4184–4187, May 2000.

[37] A. K. Iyer and G. V. Eleftheriades. Negative refractive index metamaterials supporting 2-D waves. In *Microwave Symposium Digest*, volume 2, pages 1067–1070, Seattle, WA, USA, 2-7 June 2002.

[38] C. Caloz, H. Okabe, T. Iwai, and T. Itoh. Transmission line approach of left-handed (LH) materials. In *Proc. USNC/URSI National Radio Science Meeting*, San Antonio, TX, USA, 18^{th} June 2002.

[39] L. Liu, C. Caloz, C.-C. Chang, and T. Itoh. Forward coupling phenomena between artificial left-handed transmission lines. *Journal of Applied Physics*, 92(9):5560–5565, November 2002.

[40] G. V. Eleftheriades, A. K. Iyer, and P. C. Kremer. Planar negative refractive index media using periodically l-c loaded transmission lines. *IEEE Transactions of Microwave Theory and Techniques*, 50(12):2702–2712, December 2002.

[41] K. Z. Rajab, R. Mittra, and M. Lanagan. Phase verification of compact multilayered low temperature co-fired ceramic composite right-/left-handed transmission line. *Microwave and Optical Technology Letters*, 48(9):1792–1795, 2006.

[42] E. Yablonovitch. Inhibited spontaneous emission in solid-state physics and electronics. *Physical Review Letters*, 58(20):2059–2062, May 1987.

[43] E. Yablonovitch and T. J. Gmitter. Photonic band structure: The face-centered-cubic case. *Physical Review Letters*, 63(18):1950–1953, Oct 1989.

[44] E. Yablonovitch, T. J. Gmitter, and K. M. Leung. Photonic band structure: The face-centered-cubic case employing nonspherical atoms. *Physical Review Letters*, 67(17):2295–2298, Oct 1991.

[45] E. Yablonovitch. Photonic band-gap structures. *Journal of the Optical Society of America B*, 10(2):283, 1993.

[46] J. D. Joannopoulos, Pierre R. Villeneuve, and S. Fan. Photonic crystals: putting a new twist on light. *Nature*, 386(6621):143–149, March 1997.

[47] W. E. Kock. Metal-lens antennas. *Proceedings of the IRE*, 34(11):828–836, November 1946.

[48] W. E. Kock. Metallic delay lens. *Bell System Technical Journal of Applied Physics*, 27(1):58–82, 1948.

[49] R. W. Corkum. Isotropic artificial dielectric. *Proceedings of the IRE*, 40(5):574–587, May 1952.

[50] O. F. Mossotti. Discussione analitica sull'influenza che l'azione di un mezzo dielettrico ha sulla distibuzione dell'elettricita alla superficie di piu corpi elettrici disseminati in esso. *Memorie di Matematica e di Fisica della Societa Italiana delle Scienze*, 24(2):49–74, 1850.

[51] R. J. E. Clausius. *Die mechanische behandlung der electrcität*, volume 2. Druck und Verlag von Friedrich Vieweg und Sohn, Braunschweig, Germany, 1879.

[52] Lord Rayleigh (J. W. Strutt). On the influence of obstacles arranged in rectangular order upon the properties of a medium. *Philosophical Magazine*, 34(1892):481–502, 1892.

[53] Lord Rayleigh (J. W. Strutt). On the incidence of aerial and electric waves upon small obstacles in the form of ellipsoids or elliptic cylinders, and on the passage of electric waves through a circular aperture in a conducting screen. *Philosophical Magazine*, 44:28–52, 1897.

[54] J. C. Maxwell Garnett. Colours in metal glasses and in metallic films. *Philosophical Transactions of the Royal Society of London. Series A*, 203:385–420, 1904.

[55] D. A. G. Bruggeman. Berechnung verschiedener physikalischer Konstanten von heterogenen Substanzen. I. Dielektrizittskonstanten und Leitfhigkeiten der Mischkrper aus isotropen Substanzen. *Annalen der Physik*, 416(7):636–664, 1935.

[56] J. B. Keller. Conductivity of a medium containing a dense array of perfectly conducting spheres or cylinders or nonconducting cylinders. *Journal of Applied Physics*, 34(4):991–993, 1963.

[57] J. B. Keller. A theorem on the conductivity of a composite medium. *Journal of Mathematical Physics*, 5(4):548–549, 1964.

[58] A. Lakhtakia, editor. *Selected Papers on Linear Optical Composite Materials*, volume MS120 of *SPIE Milestone Series*. SPIE Optical Engineering Press, Bellingham, WA, USA, 1996.

[59] Ari Sihvola. *Electromagnetic Mixing Formulas and Applications*. IEE electromagnetic waves series 47. The Institute of Electrical Engineers, London, UK, 1999.

[60] J. B. Pendry, A. J. Holden, D. J. Robbins, and W. J. Stewart. Magnetism from conductors and enhanced nonlinear phenomena. *IEEE Transactions of Microwave Theory and Techniques*, 47(11):2075–2084, November 1999.

[61] A. M. Nicolson and G. F. Ross. Measurement of the intrinsic properties of materials by time-domain techniques. *IEEE Transactions on Instrumentation and Measurement*, 19(4):377–382, November 1970.

[62] W. B. Weir. Automatic measurement of complex dielectric constant and permeability at microwave frequencies. *Proceedings of the IEEE*, 62(1):33–36, January 1974.

[63] D. R. Smith, S. Schultz, P. Markoš, and C. M. Soukoulis. Determination of effective permittivity and permeability of metamaterials from reflection and transmission coefficients. *Physical Review B*, 65(19):195104, Apr 2002.

[64] N. Fang, H. Lee, C. Sun, and X. Zhang. Sub-diffraction-limited optical imaging with a silver superlens. *Science*, 308(5721):534–537, April 2005.

[65] C. Caloz, A. Sanada, and T. Itoh. A novel composite right-/left-handed coupled-line directional coupler with arbitrary coupling level and broad bandwidth. *IEEE Transactions of Microwave Theory and Techniques*, 52(3):980–992, 2004.

[66] L. Liu, C. Caloz, and T. Itoh. Dominant mode leaky-wave antenna with backfire-to-endfire scanning capability. *Electronics Letters*, 38(23):1414–1416, 2002.

[67] K. Z. Rajab, R. Mittra, and M. T. Lanagan. Size reduction of microstrip antennas using metamaterials. In *IEEE Antennas and Propagation Society International Symposium*, volume 2B, pages 296–299, 3-8 July 2005.

[68] Khalid Z. Rajab, Raj Mittra, and Michael T. Lanagan. Size reduction of microstrip patch antennas with left-handed transmission line loading. *Microwaves, Antennas & Propagation, IET*, 1(1):39–44, February 2007.

[69] I. C. Khoo, D. H. Werner, X. Liang, A. Diaz, and B. Weiner. Nanosphere dispersed liquid crystals for tunable negative-zero-positive index of refraction in the optical and terahertz regimes. *Optics Letters*, 31(17):2592–2594, 2006.

[70] J. Baker-Jarvis, R. G. Geyer, Jr. Grosvenor, J. H., M. D. Janezic, C. A. Jones, B. Riddle, C. M. Weil, and J. Krupka. Dielectric characterization of low-loss materials a comparison of techniques. *IEEE Transactions on Dielectrics and Electrical Insulation*, 5(4):571–577, August 1998.

[71] J. Baker-Jarvis, M. D. Janezic, B. Riddle, C. L. Holloway, N. G. Paulter, and J. E. Blendell. Dielectric and conductor-loss characterization and measurements of electronic packaging materials. Technical Note 1520, National Insitute of Standards and Technology, Boulder, CO USA, July 2001.

[72] J. Baker-Jarvis, M. D. Janezic, B. F. Riddle, R. T. Johnk, P. Kabos, C. L. Holloway, R. G. Geyer, and C. A. Grosvenor. Measuring the permittivity and permeability of lossy materials: solids, liquids, metals, building materials and negative-index materials. Technical Note 1536, Electromagnetics Division, National Insitute of Standards and Technology, Boulder, CO USA, February 2005.

[73] M. N. Afsar, J. R. Birch, R. N. Clarke, and G. W. Chantry. The measurement of the properties of materials. *Proceedings of the IEEE*, 74(1):183–199, January 1986.

[74] K. G. Ong, J. Wang, R. S. Singh, L. G. Bachas, and C. A. Grimes. Monitoring of bacteria growth using a wireless, remote query resonant-circuit sensor: application to environmental sensing. *Biosensors and Bioelectronics*, 16(4-5):305–312, 2001.

[75] B. W. Hakki and P. D. Coleman. A dielectric resonator method of measuring inductive capacities in the millimeter range. *IEEE Transactions of Microwave Theory and Techniques*, 8(4):402–410, July 1960.

[76] W. E. Courtney. Analysis and evaluation of a method of measuring the complex permittivity and permeability microwave insulators. *IEEE Transactions on Microwave Theory and Techniques*, 18(8):476–485, August 1970.

[77] K. Z. Rajab, K.-F. Fuh, R. Mittra, and M. Lanagan. Dielectric property measurement using a resonant nonradiative dielectric waveguide structure. *IEEE Microwave and Wireless Components Letters*, 15(2):104–106, February 2005.

[78] R. N. Clarke and C. B. Rosenberg. Fabry-Perot and open resonators at microwave and millimetre wave frequencies, 2-300 GHz. *Journal of Physics E: Scientific Instruments*, 15(1):9–24, 1982.

[79] M. N. Afsar. Dielectric measurements of millimeter-wave materials. *IEEE Transactions of Microwave Theory and Techniques*, 32(12):1598–1609, December 1984.

[80] G. Kent. Nondestructive permittivity measurement of substrates. *IEEE Transactions on Instrumentation and Measurement*, 45(1):102–106, February 1996.

[81] M. D. Janezic and J. Baker-Jarvis. Full-wave analysis of a split-cylinder resonator for nondestructive permittivity measurements. *IEEE Transactions of Microwave Theory and Techniques*, 47(10):2014–2020, October 1999.

[82] A. Parkash, J. K. Vaid, and A. Mansingh. Measurement of dielectric parameters at microwave frequencies by cavity-perturbation technique. *IEEE Transactions of Microwave Theory and Techniques*, 27(9):791–795, September 1979.

[83] Kai Chang. *Microwave ring circuits and antennas*. Wiley Series in Microwave and Optical Engineering. John Wiley & Sons, Inc., New York, USA, 1996.

[84] I. Wolff and N. Knoppik. Microstrip ring resonator and dispersion measurement on microstrip lines. *Electronics Letters*, 7(26):779–781, December 1971.

[85] L. L. Li, N. H. Ismail, L. S. Taylor, and C. C. Davis. Flanged coaxial microwave probes for measuring thin moisture layers. *IEEE Transactions on Biomedical Engineering*, 39(1):49–57, January 1992.

[86] J. Baker-Jarvis, M. D. Janezic, P. D. Domich, and R. G. Geyer. Analysis of an open-ended coaxial probe with lift-off for nondestructive testing. *IEEE Transactions on Instrumentation and Measurement*, 43(5):711–718, October 1994.

[87] S. Roberts and A. Von Hippel. A new method for measuring dielectric constant and loss in the range of centimeter waves. *Journal of Applied Physics*, 17(7):610–616, July 1946.

[88] M. Olyphant and J. H. Ball. Strip-line methods for dielectric measurements at microwave frequencies. *IEEE Transactions on Electrical Insulation*, EI-5(1):26–32, March 1970.

[89] D. K. Ghodgaonkar, V. V. Varadan, and V. K. Varadan. Free-space measurement of complex permittivity and complex permeability of magnetic materials at microwave frequencies. *IEEE Transactions on Instrumentation and Measurement*, 39(2):387–394, April 1990.

[90] L. Duvillaret, F. Garet, and J.-L. Coutaz. A reliable method for extraction of material parameters in terahertz time-domain spectroscopy. *IEEE Journal of Selected Topics in Quantum Electronics*, 2(3):739–746, September 1996.

[91] L. Duvillaret, F. Garet, and J.-L. Coutaz. Influence of noise on the characterization of materials by terahertz time-domain spectroscopy. *Journal of the Optical Society of America B*, 17(3):452–461, March 2000.

[92] Z. Jiang, M. Li, and X.-C. Zhang. Dielectric constant measurement of thin films by differential time-domain spectroscopy. *Applied Physics Letters*, 76(22):3221–3223, May 2000.

[93] Peter R. Griffiths and James A. De Haseth. *Fourier Transform Infrared Spectrometry*. Wiley-Interscience, 2^{nd} edition, 2007.

[94] J. Baker-Jarvis, E. J. Vanzura, and W. A. Kissick. Improved technique for determining complex permittivity with the transmission/reflection method. *IEEE Transactions of Microwave Theory and Techniques*, 38(8):1096–1103, August 1990.

[95] G. Andermann, A. Caron, and D. A. Dows. Kramers-Kronig dispersion analysis of infrared reflectance bands. *Journal of the Optical Society of America*, 55(10):1210, October 1965.

[96] G. Mourou, C. V. Stancampiano, A. Antonetti, and A. Orszag. Picosecond microwave pulses generated with a subpicosecond laser-driven semiconductor switch. *Applied Physics Letters*, 39(4):295–296, August 1981.

[97] Y. C. Shen, P. C. Upadhya, H. E. Beere, E. H. Linfield, A. G. Davies, I. S. Gregory, C. Baker, W. R. Tribe, and M. J. Evans. Generation and detection of ultrabroadband terahertz radiation using photoconductive emitters and receivers. *Applied Physics Letters*, 85(2):164–166, July 2004.

[98] M. Bass, P. A. Franken, J. F. Ward, and G. Weinreich. Optical rectification. *Physical Review Letters*, 9(11):446–448, 1962.

[99] Y. Cai, I. Brener, J. Lopata, J. Wynn, L. Pfeiffer, J. B. Stark, Q. Wu, X. C. Zhang, and J. F. Federici. Coherent terahertz radiation detection: Direct comparison between free-space electro-optic sampling and antenna detection. *Applied Physics Letters*, 73(4):444–446, July 1998.

[100] L. Duvillaret, F. Garet, and J.-L. Coutaz. Highly precise determination of optical constants and sample thickness in terahertz time-domain spectroscopy. *Applied Optics*, 38(2):409–415, 1999.

[101] M. Schramm. Steps towards the idea of function: A comparison between Eastern and Western science of the Middle Ages. *History of Science*, 4:70, 1965.

[102] F. T. Ulaby, R. K. Moore, and A. K. Fung. *Microwave Remote Sensing: Active and Passive*, volume 1. Artech House, Norwood, MA, 1982.

[103] C. L. Holloway, E. F. Kuester, J. Baker-Jarvis, and P. Kabos. A double negative (DNG) composite medium composed of magnetodielectric spherical particles embedded in a matrix. *IEEE Transactions on Antennas and Propagation*, 51(10):2596–2603, October 2003.

[104] O. G. Vendik and M. S. Gashinova. Artificial double negative (DNG) media composed by two different dielectric sphere lattices embedded in a dielectric matrix. In *34th European Microwave Conference*, volume 3, pages 1209–1212, 11-15 October 2004.

[105] E. A. Semouchkina, G. B. Semouchkin, M. Lanagan, and C. A. Randall. FDTD study of resonance processes in metamaterials. *IEEE Transactions of Microwave Theory and Techniques*, 53(4):1477–1487, April 2005.

[106] Lord Rayleigh (J. W. Strutt). On the scattering of light by small particles. *Philosophical Magazine*, 41:447–451, 1871.

[107] Lord Rayleigh (J. W. Strutt). On the transmission of light through an atmosphere containing small particles in suspension, and on the origin of the blue of the sky. *Philosophical Magazine*, 47:375–384, 1899.

[108] A. Clebsch. Über die Reflexion an einer Kugelfläche. *Journal für Mathematik*, 61(3):195–262, 1863.

[109] G. Mie. Beiträge zur Optik trüber Medien, speziell kolloidaler Metallösungen. *Annalen der Physik*, 25(3):377–445, 1908.

[110] G. Mie. Contributions to the optics of turbid media, particularly of colloidal metal solutions. *Royal Aricraft Establishment, Farnborough (England)*, February 1976. Translation into English.

[111] L. V. Lorenz. Upon the light reflected and refracted by a transparent sphere. *Vidensk. Selsk. Shrifter*, 6:1–62, 1890.

[112] P. Debye. Der Lichtdruck auf Kugeln von beliebigem Material. *Annalen der Physik*, 335:57–136, 1909.

[113] P. C. Waterman. Matrix formulation of electromagnetic scattering. *Proceedings of the IEEE*, 53(8):805–812, August 1965.

[114] P. C. Waterman. Symmetry, unitarity, and geometry in electromagnetic scattering. *Physical Review D*, 3(4):825–839, February 1971.

[115] W. Trinks. Zur vielfachstreuung an kleinen kugeln. *Annalen der Physik*, 414(6):561–590, 1935.

[116] L. L. Foldy. The multiple scattering of waves. i. general theory of isotropic scattering by randomly distributed scatterers. *Physical Review*, 67(3-4):107–119, Feb 1945.

[117] P. C. Waterman. Multiple scattering of waves. *Journal of Mathematical Physics*, 2(4):512–537, July-August 1961.

[118] V. Twersky. Multiple scattering of radiation by an arbitrary configuration of parallel cylinders. *The Journal of the Acoustical Society of America*, 24:42, 1952.

[119] V. Twersky. Multiple scattering by arbitrary configurations in three dimensions. *Journal of Mathematical Physics*, 3(1):83–91, 1962.

[120] V. Twersky. Multiple scattering of electromagnetic waves by arbitrary configurations. *Journal of Mathematical Physics*, 8(3):589–610, 1967.

[121] S. Stein. Addition theorems for spherical wave functions. *Quarterly of Applied Mathematics*, 19(1):15–24, 1961.

[122] O. R. Cruzan. Translational addition theorems for spherical vector wave. *Quarterly of Applied Mathematics*, 20:33–40, 1962.

[123] C. Liang and Y. Lo. Scattering by two spheres. In *Antennas and Propagation Society International Symposium*, volume 4, pages 469–472, December 1966.

[124] J. H. Bruning and Y. T. Lo. Multiple scattering by spheres. Technical Report 69-5, Antenna Lab., University of Illinois, Urbana, IL, USA, May 1969.

[125] J. H. Bruning and Y. T. Lo. Multiple scattering of EM waves by spheres part I–Multipole expansion and ray-optical solutions. *IEEE Transactions on Antennas and Propagation*, 19(3):378–390, May 1971.

[126] J. H. Bruning and Y. T. Lo. Multiple scattering of EM waves by spheres part II–Numerical and experimental results. *IEEE Transactions on Antennas and Propagation*, 19(3):391–400, May 1971.

[127] B. Peterson and S. Ström. Matrix formulation of acoustic scattering from an arbitrary number of scatterers. *Journal of the Acoustical Society of America*, 56(3):771–780, September 1974.

[128] B. Peterson and S. Ström. T matrix for electromagnetic scattering from an arbitrary number of scatterers and representations of E(3). *Physical Review D*, 8(10):3661–3678, November 1973.

[129] A. Lakhtakia and M. F. Iskander. Scattering and absorption characteristics of lossy dielectric objects exposed to the near fields of aperture sources. *IEEE Transactions on Antennas and Propagation*, 31(1):111–120, January 1983.

[130] W. C. Chew, J. A. Friedrich, and R. Geiger. A multiple scattering solution for the effective permittivity of a sphere mixture. *IEEE Transactions on Geoscience and Remote Sensing*, 28(2):207–214, March 1990.

[131] Y. M. Wang and W. C. Chew. A recursive T-matrix approach for the solution of electromagnetic scattering by many spheres. *IEEE Transactions on Antennas and Propagation*, 41(12):1633–1639, December 1993.

[132] W.C. Chew and C.C. Lu. The recursive aggregate interaction matrix algorithm for multiple scatterers. *Antennas and Propagation, IEEE Transactions on*, 43(12):1483–1486, December 1995.

[133] M. I. Mishchenko, G. Videen, V. A. Babenko, N. G. Khlebtsov, and T. Wriedt. T-matrix theory of electromagnetic scattering by particles and its applications: a comprehensive reference database. *Journal of Quantitative Spectroscopy and Radiative Transfer*, 88:357–406, 2004.

[134] W. C. Chew, Y. M. Wang, and L. Gürel. Recursive algorithm for wave-scattering solutions using windowed addition theorem. *Journal of electromagnetic waves and applications*, 6(11):1537–1560, 1992.

[135] P. R. Siqueira and K. Sarabandi. T-matrix determination of effective permittivity for three-dimensional dense random media. *IEEE Transactions on Antennas and Propagation*, 48(2):317–327, February 2000.

[136] C. Meiners, J. Psilopoulos, and A. F. Jacob. Determining the scattered field of dense particles using recursive algorithms. *Microwave and Optical Technology Letters*, 40(6):523–529, 2004.

[137] V. V. S. Prakash and R. Mittra. Characteristic basis function method: A new technique for efficient solution of method of moments matrix equations. *Microwave and Optical Technology Letters*, 36(2):95–100, January 2003.

[138] S. J. Kwon, K. Du, and R. Mittra. Characteristic basis function method: A numerically efficient technique for analyzing microwave and RF circuits. *Microwave and Optical Technology Letters*, 38(6):444–448, September 2003.

[139] J. Yep, V. V. S. Prakash, and R. Mittra. Efficient analysis of a class of microstrip antennas using the characteristic basis function method (CBFM). *Microwave and Optical Technology Letters*, 39(6):456–464, December 2003.

[140] W. C. Chew. Recurrence relations for three-dimensional scalar addition theorem. *Journal of Electromagnetic Waves and Applications*, 6(2):133–142, 1992.

[141] W. C. Chew and Y. M. Wang. Efficient ways to compute the vector addition theorm. *Journal of Electromagnetic Waves and Applications*, 7(5):207–214, 651-665 1993.

[142] Akira Ishimaru. *Electromagnetic wave propagation, radiation, and scattering.* Prentice Hall, Englewood Cliffs, NJ, USA, 1991.

[143] J. A. Stratton. *Electromagnetic Theory.* McGraw-Hill, New York, NY, USA, 1941.

[144] W. J. Wiscombe. Improved Mie scattering algorithms. *Applied Optics*, 19(9):1505–1509, May 1980.

[145] C. A. Balanis. *Advanced engineering electromagnetics*. Wiley New York, New York, NY, USA, 1989.

[146] D. Sarkar and N. J. Halas. General vector basis function solution of Maxwell's equations. *Physical Review E*, 56(1):1102–1112, Jul 1997.

[147] W. H. Press, S. A. Teukolsky, W. T. Vetterling, and B. P. Flannery. *Numerical Recipes: The Art of Scientific Computing*. Cambridge University Press, New York, 3^{rd} edition, 2007.

[148] L. W. Davis. Theory of electromagnetic beams. *Physical Review A*, 19(3):1177–1179, March 1979.

[149] G. Gouesbet, B. Maheu, and G. Grehan. Light scattering from a sphere arbitrarily located in a Gaussian beam, using a Bromwich formulation. *Journal of the Optical Society of America A*, 5(9):1427, September 1988.

[150] P. Y. Han and X. C. Zhang. Free-space coherent broadband terahertz time-domain spectroscopy. *Measurement Science and Technology*, 12(11):1747–1756, 2001.

[151] V. Strassen. Gaussian elimination is not optimal. *Numerische Mathematik*, 13(4):354–356, 1969.

[152] R. A. Shelby, D. R. Smith, and S. Schultz. Experimental verification of a negative index of refraction. *Science*, 292(5514):77–79, April 2001.

[153] R. W. Ziolkowski. Design, fabrication, and testing of double negative metamaterials. *IEEE Transactions on Antennas and Propagation*, 51(7):1516–1529, July 2003.

[154] P. Markoš and C. Soukoulis. Transmission properties and effective electromagnetic parameters of double negative metamaterials. *Optics Express*, 11(7):649–661, 2003.

[155] X. Chen, T. M. Grzegorczyk, B.-I. Wu, J. Pacheco, and J. A. Kong. Robust method to retrieve the constitutive effective parameters of metamaterials. *Physical Review E*, 70(1):016608, Jul 2004.

[156] T. Driscoll, D. N. Basov, W. J. Padilla, J. J. Mock, and D. R. Smith. Electromagnetic characterization of planar metamaterials by oblique angle spectroscopic measurements. *Physical Review B*, 75(11):115114, 2007.

[157] X. Chen, B.-I. Wu, J. A. Kong, and T. M. Grzegorczyk. Retrieval of the effective constitutive parameters of bianisotropic metamaterials. *Physical Review E*, 71(4):046610, April 2005.

[158] J. F. Nye. *Physical Properties of Crystals: Their Representation by Tensors and Matrices*. Oxford University Press, New York, USA, 1985.

[159] V. V. Varadan and R. Ro. Unique retrieval of complex permittivity and permeability of dispersive materials from reflection and transmitted fields by enforcing causality. *IEEE Transactions of Microwave Theory and Techniques*, 55(10):2224–2230, October 2007.

[160] R. Marqués, F. Medina, and Rachid R.-E.-I. Role of bianisotropy in negative permeability and left-handed metamaterials. *Physical Review B*, 65(14):144440, Apr 2002.

[161] R. Ziolkowski. Pulsed and CW Gaussian beam interactions with double negative metamaterial slabs. *Optics Express*, 11(7):662–681, April 2003.

[162] M. Morgan, D. Fisher, and E. Milne. Electromagnetic scattering by stratified inhomogeneous anisotropic media. *IEEE Transactions on Antennas and Propagation*, 35(2):191–197, February 1987.

[163] W. C. Chew. *Waves and Fields in Inhomogeneous Media*. IEEE Press, New York, NY USA, 1990.

[164] *CST Microwave Studio, User Guide*. CST GmbH, Buedinger Str. 2a, D-64289 Darmstadt, Germany, 2007.

[165] M. Abramowitz and I. A. Stegun. *Handbook of Mathematical Functions with Formulas, Graphs and Mathematical Tables*. Dover, New York, NY USA, 10^{th} edition, December 1972.

[166] A. R. Edmonds. *Angular Momentum in Quantum Mechanics*. Princeton University Press, Princeton, NJ, USA, 2^{nd} edition, 1960.

[167] Y.-L. Xu. Fast evaluation of Gaunt coefficients: recursive approach. *Journal of Computational and Applied Mathematics*, 85(1):53–65, 1997.

[168] Y.-L. Xu. Efficient evaluation of vector translation coefficients in multiparticle light-scattering theories. *Journal of Computational Physics*, 139(1):137–165, 1998.

Vita

Khalid Rajab was born in Kuwait City, Kuwait, in 1982. He received the B. S. degree in Electrical Engineering from the Pennsylvania State University in 2003, and is currently pursuing his M. A. in Mathematics and Ph.D. in Electrical Engineering at the same university. Currently, he is a Research Assistant at the Materials Research Laboratory at the Pennsylvania State University. His present research interests include materials characterization at microwave and terahertz frequencies, novel electromagnetic materials, PBG and EBG structures, antenna theory, and computational electromagnetics.